Lidar-based Reconstruction of Wind Fields and Application for Wind Turbine Control

Von der Fakultät für Mathematik und Naturwissenschaften

der Carl von Ossietzky Universität Oldenburg

zur Erlangung des Grades und Titels eines

Doktors der Ingenieurwissenschaften (Dr.-Ing.)

angenommene Dissertation

von Herrn Stefan Kapp

geboren am 27.08.1984 in Ludwigsburg

Contents

Abstract

The focus on lidar anemometry is currently enlarged from market-ready stand-alone wind measurement devices towards wind turbine integrated systems enhancing monitoring and control applications. Turbine operation is expected to benefit from this trend by improved control algorithms aiming at reduced structural loads, optimized power quality and maximized energy output.

Horizontally aligned, upwind oriented turbine mounted lidar systems of the focused continuous-wave type which scan the inflow are regarded in this thesis in theory, simulation and experiments. General systems constraints regarding predictability of the evolving wind in front of a turbine as well as inherent sensor constraints are composed.

The theory of wind field reconstruction is extended from three parameter wind field models to a five parameter model comprising wind speed, two shear and two direction characteristics. The extended model is able to describe the inflow in non-uniform conditions like e.g. in wind farms more accurately. Simulations especially show that wind direction signals can be expected more precisely. Sensor requirements are derived, comprising the need for at least three measurements in two distances in front of the rotor.

A new approach to spherically scan a two-dimensional inflow area is studied in detail. From experiments it can be concluded that these comprehensive measurements can provide valuable insight into temporal and spatial inhomogeneities such as the wakes of other wind turbines. Furthermore, it was confirmed that wind field parameter reconstruction can be inaccurate in wind farm environments due to the single measurement distance. Significant inaccuracies in the instantaneous and averaged wind direction signal were found for all sampling and scanning approaches and were quantified.

The possible use of turbine mounted lidar measurements – in one or two distances – is then simulated in feedforward blade pitch control applications. All relevant steps of lidar measurement, reconstruction, wind evolution and control action are modelled in a full lidar simulation chain. Collective feedforward pitch control is well suited to supplement collective and individual feedback pitch control. The damage equivalent loads, pitch activity and power output fluctuations are reduced significantly. A positive effect of additional individual feedforward control is vanishing if well designed individual feedback control based on blade load measurements is applied. Consequently, the use of the five parameter wind field model is not stringently required for pitch control, whereas other parameters like prediction time offset and measurement distance of the focussing lidar show high sensitivity on the overall control performance and should be adjusted carefully.

Zusammenfassung

Lidar-Anemometrie erfährt derzeit eine Weiterentwicklung von marktreifen freistehenden Geräten zur Windmessung hin zu Systemen, die in Windenergieanlagen integrierbar sind und für Monitoring- und Regelungsaufgaben herangezogen werden können. Es wird erwartet, dass der Betrieb von Windenergieanlagen von dieser Entwicklung profitiert, indem neue Lidar-basierte Regelungsalgorithmen zum Einsatz kommen. Diese zielen auf eine Reduktion von Strukturbelastungen, auf die Optimierung der Qualität der abgegebenen Leistung und auf die Maximierung des Energieertrages ab.

In dieser Arbeit werden horizontal ausgerichtete, die Anströmung scannende Lidarsysteme mit fokussiertem Dauerstrichlaser für Windenergieanlagen aus den Blickwinkeln Theorie, Simulation und Experiment betrachtet. Allgemeine Einschränkungen hinsichtlich der Vorhersagbarkeit der dynamischen Anströmung einer Windenergieanlage sowie Sensor-inhärente Randbedingungen werden erarbeitet.

Die Theorie der Windfeldrekonstruktion wird erweitert von Modellen mit drei Parametern auf ein Fünf-Parameter-Modell, das die Windgeschwindigkeit, zwei Scherungen und zwei Windrichtungsparameter enthält. Das erweiterte Modell kann die Anströmung bei inhomogenen Bedingungen wie beispielsweise in Windparks genauer beschreiben. Simulationen zeigen deutlich präzisere zu erwartende Windrichtungssignale. Es werden Sensoranforderungen abgeleitet, darunter die Notwendigkeit von mindestens drei Messungen in zwei Entfernungen vor dem Rotor.

Ein neuer Ansatz basierend auf einem sphärischen Abscannen eines zweidimensionalen Einströmungsbereichs wird näher untersucht. Die Messergebnisse zeigen, dass wertvolle Einblicke in die zeitlichen und räumlichen Inhomogenitäten der Anströmung gewonnen werden können. Allerdings wird auch die mögliche Ungenauigkeit in Windparkumgebungen bestätigt, wie sie bei allen einstrahligen Messungen in nur einer Entfernung zu erwarten ist. Signifikante Ungenauigkeiten im momentanen und gemittelten Windrichtungssignal werden für verschiedene Abtast- und Scanvarianten ermittelt und quantifiziert.

Die mögliche Verwendung von gondelbasierten Lidar-Messungen – in ein oder zwei Entfernungen – wird anhand einer Blattwinkelregelung mit Vorsteuerung als Anwendung simuliert. Alle relevanten Schritte von der Lidar-Messung, der Windfeld-Rekonstruktion und der Windfeld-Evolution bis zum Stelleingriff werden in einer ganzheitlichen Lidar-Simulationskette modelliert. Als Alternative oder vorzugsweise in Ergänzung zur Einzelblattwinkelregelung ist die Lidar-basierte kollektive Blattwinkelvorsteuerung in der Lage, Ermüdungs- und Extremlasten, Abgabeleistungsschwankungen sowie die Blattwinkel-Verstellaktivität deutlich zu reduzieren.

Zusätzliche individuelle Vorsteuer-Blattwinkel bringen keine nennenswerten Vorteile, wenn bereits eine Einzelblattregelung basierend auf Blattbiegesensoren implementiert ist. Dadurch ist die Verwendung des Fünf-Parameter-Modells zur Pitchregelung nicht zwingend erforderlich, wohingegen andere Parameter einer Lidar-basierten Vorsteuerung wie beispielsweise ein ungenaues Timing oder die Messentfernung eines fokussierenden Lidars großen Einfluss auf die Leistungsfähigkeit der Vorsteuerung besitzen.

List of Figures

List of Tables

List of Abbreviations

1P	periodical at rotor speed
2P	periodical at twice the rotor speed
3P	periodical at three times the rotor speed
3pe	three parameter estimation
5pe	five parameter estimation
AEP	annual energy production
CAE	computer-aided engineering
CFF	collective feedforward
CPC	collective (feedback) pitch control
CPPP	counter pulse per pattern
CPPR1	counter pulse per rotation 1 (bottom prism)
CPPR2	counter pulse per rotation 2 (top prism)
cw	continuous-wave
DEL	damage equivalent load
DFT	discrete Fourier transform
DLL	Dynamic-link library
FB	feedback
FF	feedforward
FIR	finite impulse response
FFT	fast Fourier transform
FWFM	full width at fraction maximum
FWHM	full width at half maximum
GW	gigawatt
IIR	infinite impulse response
IEC	International Electrotechnical Commission
IFF	individual feedforward
IPC	individual (feedback) pitch control
laser	light amplification by stimulated emission of radiation
LDV	laser Doppler velocimetry
lidar	light detection and ranging
lin.	linear

LOS	line-of-sight
max $\{\cdot\}$	maximum (operator)
min $\{\cdot\}$	minimum (operator)
MPC	model predictive control
MW	megawatt
nonlin.	nonlinear
NTM	normal turbulence model
PI	proportional integral
pp	percentage points
RIN	relative intensity noise
SCADA	supervisory control and data acquisition
SNR	signal-to-noise ratio
sodar	sound detection and ranging
sync.	synchronized
TwD	tower damping
w.r.t.	with respect to

List of Notations

d	m	distance
d_t	m	lidar aperture diameter
d_{12}	m	distance between turbine (1) and (2)
D	m	rotor diameter
f	–	function (operator)
f_B	Hz	backscatter frequency
f_-	Hz	lower backscatter spectrum peak frequency
f_+	Hz	upper backscatter spectrum peak frequency
f_c	Hz	filter corner frequency
$\Phi\{\cdot\}$		Fourier transform
G_0	–	direct current amplification
$H(s)$		filter transfer function
I	–	backscatter spectrum intensity
$\bar{I}_B$	–	averaged backscatter intensity
k	m^{-1}	wavenumber
l_0	m	beam length to $\tilde{y}$-$\tilde{z}$-plane
l_{focus}	m	focus length
M	–	matrix mapping Cartesian onto polar coordinates
$M_{i,j}$	–	element of matrix M
M_{xs}	Nm	shaft torque
M_{ybi}	Nm	blade root bending moment about the y-axis of blade i
M_{yt}	Nm	tower base bending moment about the y-axis
n	–	filter order
n_{84}	–	number of azimuthally distributed scan points at $r/R = 84\%$
$p(t_i)$		arbitrary wind field parameter value at time step t_i
P_{Gen}	kW	generator power
Q_{cw}	–	spatial weighting function of a continuous-wave lidar
r_0	m	radius of beam intersection with $\tilde{y}$-$\tilde{z}$-plane
Δr	m	correction of r_0 to take into account focus position on sphere instead on circle
r	m	radial position from hub
r^2	–	coefficient of determination
R	m	rotor radius
R_{ab}		cross-correlation
R_{yz}	m	outer scan radius measured in the y-z-plane

s	–	complex variable $s = \sigma + j\omega$
s_h	(m/s) / m	horizontal shear
s_v	(m/s) / m	vertical shear
t_i	s	time step
T_I	–	turbulence intensity
$T_{I,c}$	–	conical turbulence intensity
$\overline{U}$	m/s	mean wind speed
u_0	m/s	mean streamwise wind speed
U_c	m/s	vector of wind speed components in Cartesian coordinates
U_p	m/s	vector of wind speed components in polar coordinates
v_-	m/s	horizontal wind speed at lower probe volume limit
v_+	m/s	horizontal wind speed at upper probe volume limit
v_L	m/s	wind speed in lidar beam direction
$w(\xi)$	–	spatial lidar measurement weighting function
w_{norm}	–	$w(\xi)$ normalized by $w(0)$
$W(\xi)$	–	integral of $w(\xi)$
W_{used}	–	fraction of $W(\xi)$ used in the simulation
x_{focus}	m	focus distance in x-direction
z_R	m	Rayleigh length, Rayleigh range
α	degrees	angle between lidar beam and mean wind direction
β	degrees	pitch angle
$\beta_{A,sh}$	degrees·s	individual pitch angle contribution per horizontal shear
$\beta_{A,sv}$	degrees·s	individual pitch angle contribution per vertical shear
$\beta_{A,\delta h}$	–	individual pitch angle contribution per horizontal direction
$\beta_{A,\delta v}$	–	individual pitch angle contribution per vertical direction
β_{FFC}	degrees	collective feedforward pitch angle
β_{FFI}	degrees	individual feedforward pitch angle, including β_{FFC}
β_i	degrees	pitch angle of blade i
γ	–	coherence
δ_{h}	degrees	horizontal wind direction parameter
$\delta_{\mathrm{h,fixed}}$	degrees	fixed horizontal wind direction
δ_{h}^*	degrees	relative horizontal wind direction limit of wake interaction

δ_{v}	degrees	vertical wind direction parameter
$\delta_{\text{v,fixed}}$	degrees	fixed vertical wind direction
θ	degrees	half cone opening angle of the optical scanner head
ϑ	degrees	angular rotor position, angular coordinate
ϑ_{error}	degrees	angular rotor position error
ξ	–	distance in beam direction without units
ϱ	m	radial coordinate
$\sigma\{\cdot\}$		standard deviation
τ_{error}	s	remote sensing preview time error
τ_g	s	filter group delay
τ_{pre}	s	remote sensing preview time
τ	degrees	rotor tilt angle
ϕ_{sh}	degrees	constant pitch phase offset for horizontal shear
ϕ_{sv}	degrees	constant pitch phase offset for vertical shear
$\phi_{\delta h}$	degrees	constant pitch phase offset for horizontal wind direction
$\phi_{\delta v}$	degrees	constant pitch phase offset for vertical wind direction
ϕ_1	degrees	bottom prism angle of rotation
ϕ_2	degrees	top prism angle of rotation
φ	rad	phase of complex number
ω	rad/s	angular frequency
ω_c	rad/s	angular filter corner frequency
Ω_{R}	rad/s	angular speed of the rotor

1   Introduction

"Even now it is not utterly chimerical to think of wind superseding coal in some places for a very important part of its present duty – that of giving light."

Sir William Thomson, "Lord Kelvin", 1881 [1].

1.1   Motivation and Scope

Wind energy as one of the renewable energy sources is considered to contribute significantly to a sustainable power supply system in the long term, since its natural resource, the kinetic energy of moving air driven by pressure differences, cannot be exhausted. Even now wind energy has gained considerable contribution to the electricity generation in many economies. The European Wind Energy Association EWEA estimated the share of generated electricity in the European Union to 8% in 2013 [2]. With 105 GW net installed capacity between 2000 and 2013, wind energy dominates over all other renewable and conventional installations. The development is supported by decreased production costs of 4.5 to 10.7 Ct/kWh in 2013 [3] and political efforts. To preserve and increase competitiveness and profitability of wind energy, advancement in wind turbine technology research and development is often seen as one requirement.

The basic principle of power extraction from the wind is the interaction of air over the whole wind field with the aerodynamic blades of the rotor. Although this interaction is the basis for all mechanical and electrical behaviour of the system, up to now, the behaviour of the wind itself in front of the rotor is not measured systematically during operation with a sensor on the nacelle. Several current wind turbine control and monitoring applications could potentially benefit from these measurements: Pitch and generator control could proactively act in advance of changing conditions, yaw control could benefit from wind direction signals obtained by distributed measurements and performance monitoring could be enabled without the use of sensors on an external measurement tower. However, potentials of the desired benefits and in particular the influence of the design of such a remote wind speed sensor system on the benefits have not been researched in all details.

One sensor system candidate for these tasks has arisen from the development of laser technologies and the advancements in communication technology: A lidar – light detection and ranging – is able to measure the wind speed remotely and, by use of scanners or beam splitters, at different locations within a wind field. Although a lot of experiences have been made with lidar systems for ground based wind speed measurements, a lot less is known about its possible use to measure inflowing winds from a horizontal nacelle based position. Besides mechanical questions, it is

particularly unclear how the scanning, signal processing and data aggregation should be designed so that useful information for the abovementioned applications is generated.

It is therefore the aim of this thesis to contribute to the deepening study of the use of horizontally oriented turbine mounted lidars for wind turbine control applications.

Two indications additionally plead for the future use of lidars on wind turbines: Decreasing costs for lasers and for lidar systems and increasing unit costs of an average wind turbines (see Figure 1-1) result in decreasing costs to equip wind turbines with turbine mounted lidars, making lidar based applications economically more attractive. Secondly, the increased interest in lidar technology is reflected by the increasing number of yearly publications which are exceeding the number of publications related to competing wind speed sensing technologies like cup, ultrasonic or sodar anemometry (see Figure 1-2).
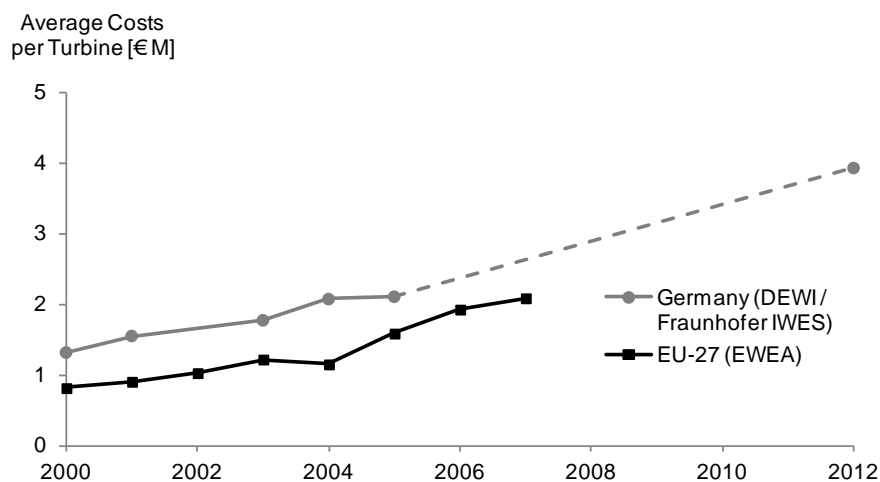
Figure 1-1: Average costs per installed onshore wind turbine in Germany (grey) and in the European Union (black) derived of statistical data of DEWI [4], Fraunhofer IWES [5] and EWEA [6].
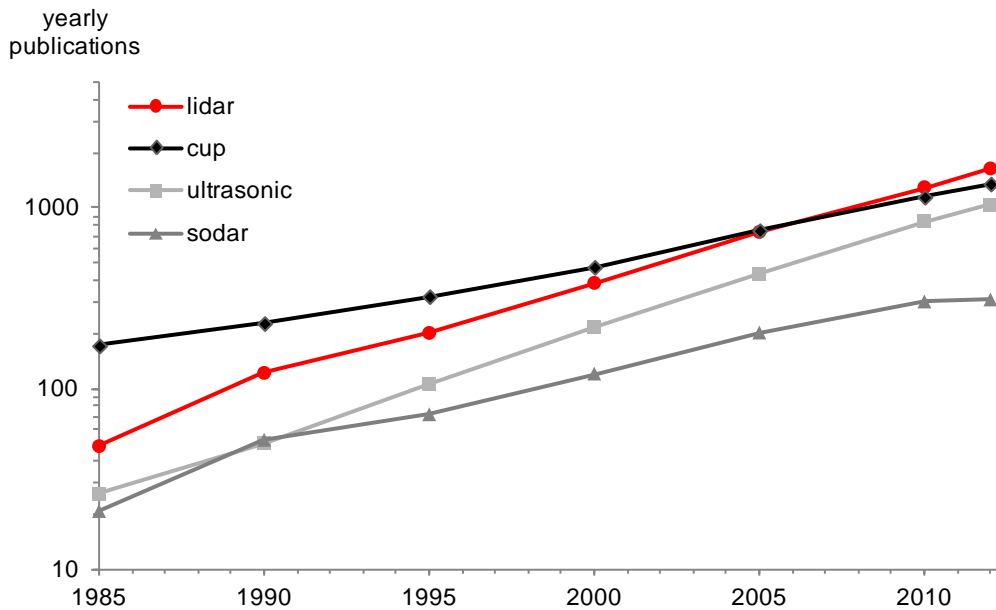
Figure 1-2: Number of new yearly publications listed on Google Scholar [7] using search expressions "wind speed" AND "lidar", "cup", "ultrasonic" or "sodar" respectively. Citations and patents have been excluded. Since 2005 publications including "lidar" dominate over the other measuring systems.

In the next section the current state of lidar anemometry in wind industry and research is described and important developments in lidar based wind turbine control are given. Three explicit issues to be focused in the thesis are derived.

The introduction concludes with an overview about the thesis outline showing that the issues will be studied in the categories theory, simulation and experiment.

1.2   Current State and Research Issues

Actually, the idea to measure upwind wind speeds using a laser Doppler anemometer is more than 25 years old. In 1989, Vaughan and Forrester stated [8]: "In the long term, the potential for routine wind monitoring and gust warning from LDV [author's note: laser Doppler velocimetry] equipments mounted on the nacelles of large wind generators would seem very considerable." The authors also explicitly anticipated the turbine mounted lidar's potential for enhanced blade pitch control and gust warnings. But the early lidars commonly have not been mounted on wind turbines.

Lidar anemometry has found entrance into the wind energy market during the preceding decade mainly as a consequence of cost decreases of lasers and optical parts of the telecommunication technology. The first commercialized lidars were ground based, vertical oriented and scanning or beam switching. They aim at measuring the wind speed and direction at one or several heights for site assessment, i.e. for qualifying the availability of wind resources at a specific geographic location. Portable lidars for site assessment are favorable if a fast

overview of the wind potential is to be acquired or the required increasing hub heights of modern wind turbines cannot be reached economically using very large met masts. However, as of today lidars are not heading to completely replace traditional measurements in bankable wind resource assessments because the assumption of homogenous wind within the scanned measurement area is invalid in complex terrain and leads to erroneous wind estimates [9].

The complexity and weight of lidars decreased: A carbon dioxide lidar system in 1996 referred to as "compact" in [10] was specified 250 kilograms, while today's lidar systems can weigh below 30 kilograms. Also, fibre laser sources have been replaced by laser diodes recently in some commercial lidars and new suppliers of dedicated turbine mounted lidar systems have entered the market with lower prices by a factor of five compared to established suppliers [11].

Consequently, experimental mounting of lidars on wind turbine nacelles was started and scientifically accompanied:

- In [12] the first experimental installation of a turbine mounted lidar is proclaimed. In 2003 a Nordex N-90 wind turbine was equipped with a one beam staring continuous-wave lidar focused at 200 meters distance, demonstrating the possibility of upwind measurements.

- In 2009 a pulsed lidar system comprising a mirror based deflection unit started recording wind speeds by different scan patterns upwind of an Areva M5000 [13].

- In 2010 the first inflow scanning lidar was mounted in the rotating spinner of a NEG Micon NM80 wind turbine, demonstrating the ability to scan and acquire inflow wind field measurements [14].

- In 2013 the results of a field test of collective pitch control based on the measurements of a commercial turbine mounted three beam lidar were published [15]. For the first time it could be demonstrated that lidar anemometry can be used in real time for load reducing feedforward pitch control.

In the existing studies, often a rotor averaged wind speed signal is calculated and compared to estimations based on other sensor signals. The signal is then used for control simulations, for performance monitoring or for real time collective pitch control. Less often, more detailed inflow characteristics like wind shear and wind direction are determined and evaluated regarding their use for turbine controls. Therefore, more complex wind inflow models than the existing models with one or three parameters are necessary, and suitable algorithms to reconstruct these parameters from the lidar measurements have to be developed and tested.

In this thesis, the focus on inflow wind shear and direction detection is covered. Therefore, the existing wind inflow models are enlarged to more parameters to be determined, and strategies to reconstruct these parameters from lidar measurements are developed.

Connected to these new lidar measurement opportunities, the study of new applications making use of the distributed preview information is ongoing. One possible application is the expansion of blade pitch control strategies by using preview wind information.

Wind turbine blade pitch control primary aims at limiting the amount of extracted energy to avoid overload on the generator or inverter. Moreover, modern pitch control aims at reducing power fluctuations as unwanted effects on the power grid, at reducing loads on the blades and subsequent components of the turbine and at increasing the energy extraction at partial load conditions. The actuators are pitch drives changing the blades' angles about their longitudinal axis and hence influence the aerodynamic forces on the blades. The control loops are closed by measurements of rotor speed, blade loads or of other structural loads or movements and a controller calculating pitch signal updates. For instance, an increased rotor speed produces a positive pitch increment update, resulting in reduced torque on the rotor and decreasing rotor speed.

Often, basic proportional-integral-derivative control is applied due to its simplicity [16]. More advanced methods are based on the weighting of rotor speed and tower acceleration sensors [17], the use of an observer for signals assumed unknown as the wind speed [18] or individual blade pitch control to mitigate asymmetric loads on the rotor [19], [20], [21]. A new holistic control approach is presented in [22] to meet the different control objectives simultaneously.

One of the latest developments is to include measurements of inflow wind speeds explicitly in the control structure so that controls not only rely on the measured turbine response, but also on the approaching wind conditions. The main advantage of feeding inflow wind speed signals forward to the manipulated variable, referred to as feedforward control, turns out to provide preview time, i.e. the difference between remote measurement and wind arrival at the rotor plane. The preview time can be used for controller computations, filter algorithms or the compensation of actuation dynamics.

Several feedforward based control strategies have already been proposed in literature. In 2006 Harris et. al. simulated a wind turbine with a turbine mounted lidar enhancing the individual blade pitch control [12]. Damage equivalent loads (DELs) of the blade flap were found to decrease by around 10%, compared to control without lidar information. Although the study was limited to a 600 kW two bladed turbine, the

results were promising and initiated further research. In 2008 Schlipf and Kühn presented the theory of predictive disturbance reduction, stability and robustness analyses for a basic proportional-integral (PI) collective pitch controller enhanced with wind speed information [23]. In 2011 model predictive control (MPC) strategies based on lidar measurements had been studied by Laks et.al. [24], Jespersen et.al. [25] and Körber et. al. [26]. It was pointed out that the use of MPC without lidar wind speed information leads to a trade-off between the reduction of load fluctuations and the reduction of power output fluctuations, while the supplement of lidar wind speed information to MPC can result in both reduced loads and reduced power fluctuations. In [27] FIR and PI based control strategies have been compared. Although the approaches are different, similar load reduction can be achieved. In 2016 Schlipf published comprehensively the challenges and approaches of lidar assisted wind turbine control [28]. He introduced an analytical model of the correlation between measurements of a pulsed lidar and the turbine response as a basis for control concepts, and developed a lidar-assisted flatness based collective pitch control for further damping of the tower in simulations.

It can be concluded that simulative studies with different lidar sensor and scanner models and with different feedforward pitch control strategies result in similar load reduction potentials for components of the modelled wind turbine.

In these simulations, often a fixed lidar scanning behaviour, a specific wind field reconstruction method and fixed further signal processing steps like filtering are assumed. Rarely, the actual influences of all these elements in the so called lidar measurement chain on the control behaviour have been studied in detail. So it is the aim of the thesis to contribute to the analysis of the sensitivity of the lidar measurement chain elements on the overall control performance.

From the above introduced necessities to extend existing wind inflow models, to develop and test parameter reconstruction algorithms and to explicitly study all relevant lidar measurement chain elements in a feedforward pitch control strategy, the following three research objectives are given for this thesis:

1. The development and evaluation of a reconstruction method for multiple inflow parameters from measurements with a turbine mounted lidar.

2. The experimental study of the reconstruction of wind field parameters using a two-dimensional scanning spinner lidar within a wind farm.

3. The modelling of a full measurement chain with a turbine mounted lidar and the analysis of a feedforward pitch control strategy.

For the modelling and experimental tasks this thesis, the focus on a specific lidar technology is required. A short-range continuous-wave upwind oriented scanning lidar is chosen. Nevertheless, most results can be regarded independent of the specific lidar technology and are declared respectively.

1.3   Structure of the Thesis

The thesis is organized as follows: After the introduction Chapters 1 and important basics about the lidar measurement principle in Chapter 2, the main contents of the thesis are developed in three steps, compare Figure 1-3.

Step 1 focusses on the lidar sensor, its constraints and the directly affecting data processing. Theory and experimental analyses are covered in Chapter 3 and 0 respectively.

In Step 2 wind field reconstruction as one issue of the sensor concept is analysed in detail in theory and simulation and a new model is developed and tested in Chapter 4. In Chapter 5, experimental parameter reconstruction results are presented.

Step 3 covers the modelling of a full lidar measurement chain and lidar based pitch control simulations with assessment of the performance and a sensitivity analysis.

In Chapter 7 the results referring to the three research objectives given in Section 1.2 are concluded and an outlook is given.

theory	simulation	experiment

Chapter 1

introduction

Chapter 2

lidar measurement principle

Chapter 3

1.

wind predictability constraints
sensor constraints

Chapter 5

spinner lidar experiment
lidar data processing methods

Chapter 4

2.

wind field reconstruction	
3-para-meter model	5-para-meter model

parameter reconstruction simulation
performance evaluation and comparison

3-parameter reconstruction
comparison and evaluation

Chapter 6

3.

lidar based wind turbine control
filter design
feedforward pitch control

feedforward pitch control performance
sensitivity analysis
other applications

Chapter 7

conclusions and outlook

Figure 1-3: Outline of the thesis structured by chapters, by the three categories theory, simulation and experiment and by the steps 1. lidar measurement, 2. wind field reconstruction and 3. control applications.

Figure 1-4: NEG Micon NM80 wind turbine (today Vestas) equipped with a lidar in the rotating hub. Setup and experiments are presented in Chapter 5.

2 Lidar Measurement Principles

The notation "light detection and ranging" can be regarded as an imprecise formulation of the common technology, since the light source implicitly is given by a laser in all relevant applications. Moreover, the laser source is one of the most characterising, challenging and expensive parts of a lidar. Therefore the acronym ladar – laser detection and ranging – and the word formation laser radar are both used equivalently to lidar.

Lidar is not imaginable without the advantages of laser light, namely high light intensity, narrow frequency range, low beam divergence, large coherence lengths or short intense pulse radiation. The development of lidar technology is therefore closely coupled to that of lasers and its widespread use and applications. Apart from wind anemometry, the latest developments in laser technology include for example optical drives, telecommunications, pointing devices for computing, 3D scanners, projector lamps, welding processes, medical scalpels or automotive lighting. For several products, lasers have the potential to become a disruptive technology. Similarly, in some fields of wind sensing, lasers are about to replace other remote or non-remote sensing techniques, or occupy new fields of application.

2.1   Non-Remote Wind Measurement Techniques

2.1.1   Cup Anemometry

Since mankind began to make use of the wind energy, there had always been the need to know the speed and direction of the wind. In the 15th century, one of the first modern wind speed measurements was mentioned in writing, when Leon Battista Alberti invented the cup anemometer [29]. Several times improved during the last centuries, today the cup anemometer is a mature, economical, robust and easy to maintain technology. Therefore, cup anemometers are recognised as a reference technology for free field wind measurement in wind energy applications, for example in power performance measurements according to IEC 61400-12 [30]. The common three or four cups have different drag coefficients on their two faces, resulting in a rotation signal proportional to the speed of the wind. Disadvantages include the slow response due to the inertia of the rotating mass as well as the limitation to measurements within a small area in the order of several square centimeters, if an inflow area is to be measured. Particularly the latter disqualifies cup anemometers for blade pitch control for wind turbines, since a point-like measurement provides less information about the rotor average wind speed than the rotor speed itself.

2.1.2 Ultrasonic Anemometry

A second class of in situ wind speed measurement techniques is characterised by ultrasonic or briefly sonic anemometers. The measurement principle is based on the detection of the speed of sound between pairs of transducers, which changes with the velocity component of the air in the direction of propagation. Often, two or three pairs of transducers are combined to output the two or full three dimensional wind speed vector. Sonic anemometers can reach high sampling rates of e.g. 100 Hz, which is relevant for turbulence measurements but is not an important criterion for controls. Disadvantageously for the purpose of the thesis, sonic anemometers also measure over a limited space, e.g. along a sound path of around 10 to 20 centimeters [31].

The wind direction signal is also provided by one or two ultrasonic anemometers on many wind turbines. Mechanical wind vanes as an alternative with lower invest costs are less reliable for modern on- or offshore wind turbines.

A further development of ultrasonic wind speed measurements is the so called spinner anemometer [32]. Three ultrasonic sensors are installed on the rotating spinner of a wind turbine rotor. From the three signals, an average wind speed and direction signal in a non-rotating system is calculated. Although the measurement does not cover the whole inflow region, the installation position excludes most unwanted rotor effects on the measurement and provides an alternative to non-remote sensor systems installed behind the rotor on the nacelle.

2.2 Remote Sensing Techniques for Wind Energy Applications

The class of remote sensing devices offers two significant improvements in anemometry for wind energy, compared to non-remote techniques: Firstly and obviously, remote measurements can be taken at locations where the installation of conventional anemometers cannot be justified economically, i.e. at large heights above ground of e.g. more than 200 meters or at offshore locations. For applications related to site assessment, remote sensing has therefore gained increasing interest over the past years, since rotor diameters and tower heights have enlarged. Secondly, measurements at spatially distributed probe points or more precisely volumes can be taken with only one anemometer by the use of a beam splitter or scanner head. As will be shown the speed of scanning can thereby reach the order of several hundred measurements per second. This offers the possibility to obtain information about the overall inflow area without relocating the anemometer or installing multiple devices.

2.2.1 Sodar Anemometry

Sodar– sonic detection and ranging – systems have been investigated since 1964 as remote wind speed sensors [33]. Sodars measure the wind speed and other atmospheric conditions by comparing acoustic signals propagated to the air and their respective backscattered signals. Commonly the Doppler effect – the frequency shift of the backscattered signal with the speed of the air – is used to determine the wind speed in propagation direction.

One of the most important technological disadvantages regarding wind turbine control applications is the relatively low sampling rate in the order of 0.1 Hz [34], [35]. Others are low measurement accuracy [36], large probe and measurement volumes and noise emission.

2.2.2 SAR Anemometry

SAR (synthetic aperture radars) can be installed on moving bases like satellites or aircrafts. Electromagnetic pulses are sent to the sensed surface and the time delay and Doppler shift of the backscattered signal is received. Typical wavelengths of the transmitted radiation range from 2.5 to 30 centimetres. By that, small scale ripples at the sea surface can be sensed, which can be transferred to wind speed information of the local wind based on empirical knowledge [37]. The method is limited to offshore measurements and its accuracy to the empirical model. Supplement wind direction information usually is necessary as an input to the wind speed calculation.

2.2.3 Radar Anemometry

Radar (radio detection and ranging) technology can also be used to detect wind behaviour. A small amount of transmitted radiation is scattered back to a receiver. A Doppler radar analyses the frequency shift and thus calculates the speed of the scattering remote obstacle in beam direction. Radar scattering is most sensitive for structures in the air of the size of half the wavelength, i.e. the order of millimetres to centimetres. Therefore, radars are often used to measure boundary layers and detect clouds, but also as wind profilers to measure wind speeds up to several kilometres.

In a recent research study wind speeds have been measured using two Doppler radars operated in a horizontal configuration within a wind farm of 36 wind turbines [38]. Applications are anticipated in advanced wind farm control and operation.

General disadvantages of current Doppler radars for turbine inflow measurements are spatial resolution limitations and the high power consumption.

2.2.4 Lidar Anemometry

Lidar – light detection and ranging – is related to sodar and radar by the principle of comparing transmitted and backscattered signals to remotely sensed structures. Instead of sound or microwaves, laser light is emitted, enabling the remote fast sensing of small structures in the air, which is not possible with any other anemometer technology. The advantages of lidars include high spatial and temporal resolution, high accuracy, small system sizes, low power consumption, low radiation emissions and no sound emission. A brief introduction into lidar technology is given in the following sections.

2.3 Classification of Lidars

Lidars have been developed for a wide range of applications. The different objectives – environmental characteristics – are detectable by different physical processes, resulting in dedicated lidar devices, see Figure 2-1.

For wind speed measurements, basically elastic scattering of laser radiation by aerosols or molecules is relevant. Inelastic scattering, resonance scattering and the absorption principle are particle specific effects and are therefore used to analyse the composition, concentration or temperature of the sensed air volume. For wind speed considerations, these particle characteristics are mainly irrelevant. Another important class of lidars, not only for research applications, analyses the reflected radiation by hard targets for speed and distance measurements. Since the energy of the reflected signals is larger by several orders of magnitude, the use of these lasers as wind lidars is impossible, even if the wavelength might be suitable for elastic scattering. A more comprehensive description of different lidar principles and technologies is provided by Weitkamp [39].

For wind speed measurements based on elastic scattering of aerosols, basically there exist two principles, coherent Doppler and incoherent direct detection. The former is the most often applied technology and is described in Section 2.4. Alternatively, direct detection offers a method without the use of expensive coherent laser sources and components. The measurement principle is based on the detection of the energy of the scattered laser radiation, resulting in a map of aerosol concentrations. By correlating several concentration maps, the movement of structures in the measurement volume can be tracked and the wind speed can be implied. Field tests have been performed with a prototype [40] and first products entered the market.

In the following, the focus is on turbine mounted devices, measuring wind speed and turbulence with coherent Doppler lidars, being based on the elastic scattering of laser radiation by aerosols.

physical process	device	objective	platform
elastic scattering by aerosols	coherent Doppler wind lidar (pulsed or continuous-wave)	wind speed	ground based
			turbine mounted
			buoy based
		turbulence	…
	incoherent direct detection lidar	wind speed, aerosol concentration	…
elastic scattering by molecules	Rayleigh lidar	temperature, wind speed	…
inelastic scattering	Raman lidar	optical density	…
resonance scattering	resonance fluorescence lidar	temperature, density, clouds	…
absorption by atoms and molecules	differential absorption lidar	ozone, humidity	…
reflection from surface	laser altimeter, laser range finder	topography, distance	ground based
			airborne

Figure 2-1: Classification of lidars based on Chu's categorization [41], extended and sorted by the underlying physical process. Dark grey: class of lidars focussed in this thesis.

2.4   Coherent Doppler Lidar

2.4.1   Measurement Principle

Figure 2-2 illustrates the measurement principle of coherent wind lidar devices using the Doppler effect of light backscattered by aerosols.

A laser beam is emitted and backscattered at a certain distance within a system inherent probe volume by aerosols, i.e. solid particles or liquid droplets in the air. The aerosols are of similar size as the laser wavelength λ and the elastic scattering is called Mie or Lorenz-Mie scattering. It is implicitly assumed that the aerosols move in the direction and with the speed of wind within the backscatter volume.

The backscatter signal changes its frequency by a small frequency shift Δf due to the Doppler effect and is received and superimposed by the original transmitted signal of unchanged frequency f. The two signals of neighbouring frequencies, f split from the laser source (local oscillator) and $f + \Delta f$ from the receiver are combined in a frequency mixer, which outputs a beat signal with dominant frequencies $2f + \Delta f$ and Δf. In practise the nonlinear mixing also produces a constant component and higher frequency components, which have to be filtered out. The beat component, the Doppler frequency Δf, is found by spectral analysis of the lower frequency range. The resulting spectrum will be referred to as backscatter spectrum in the following.

The speed component in beam direction of the aerosols and thereby of the wind, v_{LOS}, is then proportional to the Doppler frequency Δf [12]:

$$v_{LOS} = \frac{\lambda}{2} \Delta f,$$ (2.1)
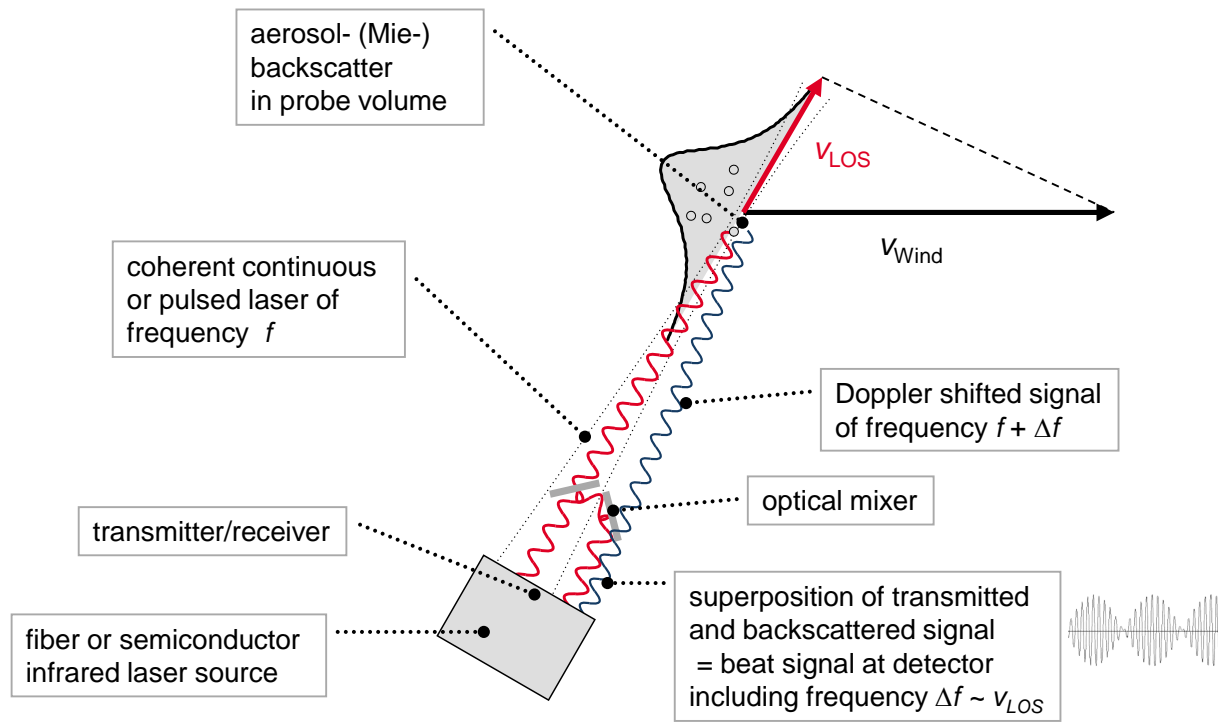
Figure 2-2: Measurement principle of homodyne coherent Doppler wind lidars.

The described architecture is known as homodyne detection, because the frequency of the transmitted signal and the frequency of the local oscillator in the optical mixer are equal. A disadvantage of current lidars according to the homodyne detection principle is that positive and negative line-of-sight wind speeds result in the same (symmetric) backscatter spectra and therefore the radial wind speed direction cannot be discriminated. In vertical lidars for site assessment, wind direction measurements from additional sensors are used to solve this ambiguity. A current research

approach by Abari et. al. proposes an image-reject method for a homodyne coherent Doppler wind lidar as a further solution [42]. However, sign ambiguity is a minor problem for turbine mounted, horizontal oriented inflow scanning wind lidars, since flow directions against the inflow direction for an operating turbine at relevant wind speeds are very unlikely.

A related architecture is known as heterodyne detection. Here, the transmitted signal is phase shifted by an additional frequency offset f_{offset}, whereas the reference in the optical mixer remains the same. As a result, the beat signal occurs at $f_{\text{offset}} + \Delta f$, the obtained spectrum is not symmetrical and positive and negative wind speed can be distinguished. Some current wind lidars work according to the heterodyne detection principle, but require additional optoelectronic components.

2.4.2 Functional Design

A Doppler lidar comprises a semiconductor or, recently increasingly, a fibre laser source emitting laser radiation in a small bandwidth at the typical wavelength of $\lambda \approx 1.5$ µm. Around this wavelength band, reliable photodiodes are available from telecommunication components [43]. A co-located detector, often combined with the transmitter in the form of a transceiver, receives the backscatter signal from the air. The backscatter signal is mixed and superimposed with the reference beam, a fraction of the emitted laser beam. Referring to [12], the backscatter signal power can be approximated by

$$P_S = \pi \, \beta \, \lambda \, P_T \qquad\qquad (2.2)$$

with transmitted signal power P_T and backscatter coefficient β.

β varies with the aerosol concentration and takes values of 10^{-8} m^{-1} in clear air inside the boundary layer [12]. Consequently, the received signal power is extremely low, in this example reduced by a factor of $5 \cdot 10^{-14}$. This is emphasizing the need for high sensitive opto-electronic components in the receiver. Supplementary to Equation (2.2), further factors are introduced in literature to describe power reducing behaviour in the measurement chain of transmission, backscatter and receiving, e.g. an efficiency parameter of optics and electronics [44] or a transmission term [39].

2.4.3 Continuous-Wave and Pulsed Radiation

In current laser sources of lidars, the radiation is emitted either in continuous-wave or in pulsed form. This not only influences the construction of the anemometer, but also the signal processing and the measurement principles and possibilities. A continuous-wave wind lidar focusses the beam at a specific distance. To measure in multiple distances, sequential refocussing is necessary. In a region around this focus length, the so called probe volume, the laser light is backscattered, whereas most of

the backscattering occurs around the centre of the volume. The width of the probe volume thereby scales with the square of the focus length. Large sample volumes at large distances can be disadvantageous for applications. Also, strong reflections from targets even out of focus such as remote clouds clouds can influence the measurements, but algorithms to detect and correct cloud effects have been developed [45].

A pulsed wind lidar uses the time of flight to determine the distance in which backscattering occurs. By that, receiving the backscatter signal at multiple times allows for the wind speed detection from multiple distances using the same laser pulse. The weighting function describing the backscatter behaviour within these range gates depends on the pulse duration and the rage gate window, but not on the measurement distance. Consequently large maximal measurement distances up to several kilometres can be reached by pulsed wind lidars. Disadvantageously, the time resolution, typically 0.1 to 10 Hz [46], is lower than in continuous-wave lidars (50 to 400 Hz), and range resolution and velocity resolution are inversely proportional [46], so that a trade-off between these two measurement goals is necessary.

2.4.4 Signal Processing

In practice, the Doppler shift frequency Δf cannot be extracted from the detector output directly. Rather, the output signal is converted to a digital signal and spectrally analysed applying e.g. the fast Fourier transform (FFT). The obtained spectrum of the backscattered and superimposed signal, generally has a peak in the region of the most often occurring wind speeds within the probe volume (for details see the spatial averaging effect in Section 3.2.3).

The spectrum peak is the basis of determining the wind speed in the region around the measurement distance, i.e. the focus distance of the optical unit of a continuous-wave lidar or the range gate of a pulsed lidar respectively. For obtaining a valuable wind speed signal, several methods have been developed to analyse the Doppler spectrum. As proposed in [47] the calculation of the spectrum's centroid has revealed as the preferred method to get the mean wind speed, which is then assumed proportional to the frequency of the centroid. Others include e.g. the detection of the frequency of the maximum or median of the backscatter spectrum intensity. When averaging over a longer time period like ten minutes, however, the choice of the method is not critical.

In Chapter 5.2 a full signal processing scenario is described and useful extensions for horizontal lidars are developed. The algorithm is applied by means of experimental raw lidar data.

3   Lidar Inflow Measurement

Applying wind lidars for wind turbine inflow measurements causes new challenges in correctly interpreting the acquired data, compared to conventional ground based operation. While operators of ground based lidars typically are interested in wind speeds measured in one or several specific heights, the turbine mounted application virtually aim at predicting wind fields in the rotor plane. This additionally requires a step of predicting the approaching behaviour of the wind. Air flow predictability and its constraints are therefore considered in Subsection 3.1.

Secondly, wind field reconstruction constraints caused by the lidar wind sensor itself are regarded, including the important limitation of measurements to the beam direction of the laser light, typical effects visible in the backscatter spectrum, the spatial averaging effect of lidars and the consideration of temporal resolution and availability with special focus on turbine mounted applications.

Thirdly, specific requirements regarding the aimed control applications are derived.

3.1   Air Flow Predictability Constraints

The measurement of air flow in front of a wind turbine is a special case of flow measurement, because the boundaries, obstacles, cross-, up- or downstream regions and influencing effects from neighbouring rotors (wakes) in the inflow area are generally not known. In contrast to e.g. the flow of a fluid within a tube, where these uncertainties can mostly be excluded, furthermore the unbounded air stream can expand.

Besides changed wind conditions also the actual transit time between the measurements and the impact on the rotor plane is unknown and has to be estimated.

All flow effects follow known physical laws and should be regarded deterministic. If the complete initial state of the flow up to an arbitrary height and width was known, as well as all boundary surfaces, and the physical composition of the air, the evolution of the inflow could be predicted up to a given precision. Since these conditions can generally not be fulfilled, in practical applications it is recommended to distinct the wind field evolution into deterministic effects, being characterised by quasi-predictable behaviour, and turbulent effects, which can be regarded unpredictable.

3.1.1   Deterministic Wind Field Evolution

Wind turbines are designed to extract a part of the kinetic energy of an air flow during operation. The impulse theory derived by Betz [48] in 1920 builds a simplified model

of the air flow around a rotor. One of its essential results is the limitation of extractable energy by a lossless energy conversion from an ideal air flow to approximately 59.3%. In these idealised conditions wind speed reduces by one third in the rotor plane and by two thirds behind the rotor, compared to the undisturbed inflow wind speed at distance d, cf. Figure 3-1. To estimate the travel time of wind approaching the rotor due to the deceleration, two idealised speed decrease behaviours are regarded, a speed step and a linear speed decrease. An idealised speed step as shown in Figure 3-2 represents the latest possible speed decrease just within the rotor plane. In this simple model, wind of constant speed U_1 arrives at the rotor plane after the time $t_1 = d/U_1$. An upper travel time estimation is derived by the idealised assumption of a linear decrease in speed from U_1 to $2/3\,U_1$. In this case, the travel time is given by $t_2 = 6/5\,d/U_1$. The idealised models result in a time difference of $t_2 - t_1 = 1/5\,d/U_1$, representing the maximum travel time prediction error, if wind approach with constant speed U_1 is assumed. Practically, the distance d to undisturbed inflow is considered to be around 2.5 to 4 times the rotor diameter of modern wind turbines [49], so that e.g. wind speeds of 10 m/s in front of a rotor of 100 m diameter can lead to a maximum travel time prediction error of 5 to 8 seconds.

In reality, the wind speed decrease will always be between these two idealisations. Typical wind speed decrease upwind a specific turbine and for specified inflow and boundary conditions can e.g. be calculated applying CFD techniques. A sigmoidal function is proposed as a good approximation for the typical decrease and depicted in Figure 3-2. Then, the maximum travel time prediction error is less than $1/5\,d/U_1$, but can still be in the order of one second. In Chapter 6 it will be shown that timing errors of that order can significantly influence the control performance of a lidar based blade pitch control strategy, so consequently the actual systematic wind speed decrease upwind a lidar controlled wind turbine needs to be known sufficiently precisely.

Other deterministic effects like the expansion of the stream tube as sketched in Figure 3-1 and the wake rotation seem to be of minor relevance for upwind measurements and inflow prediction. Expansion can be assumed to axisymmetric so that the azimuthal distribution does not change. Spin can be approximated to originate from the blade interaction in the rotor plane. Both have rather significant influence on the wake behind the rotor [50], which is currently discussed in the field of wind farm operation optimization, e.g. by applying yaw control for active flow direction control [51] [52].
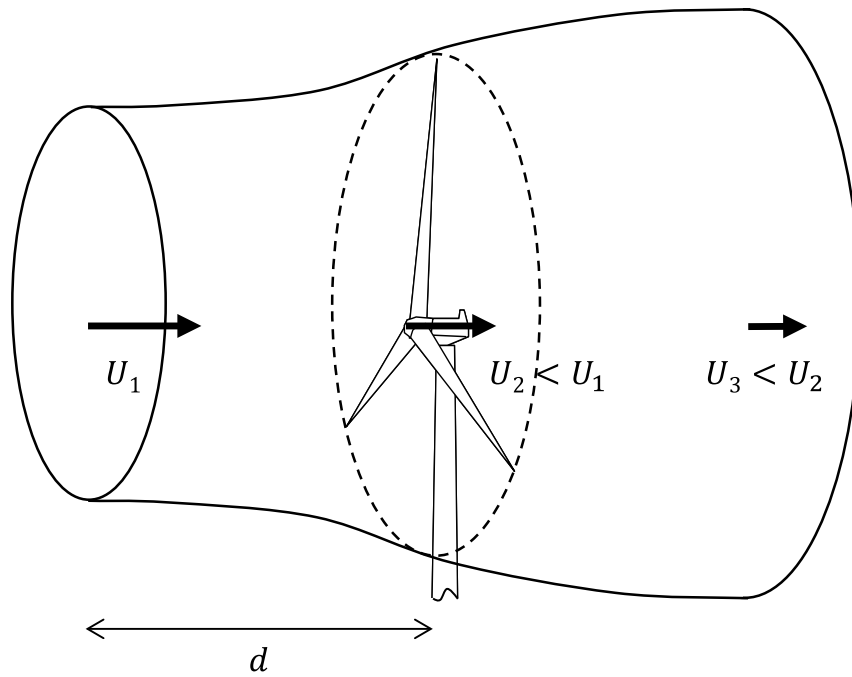
Figure 3-1: Air flow around a wind turbine: Schematic expansion and deceleration.
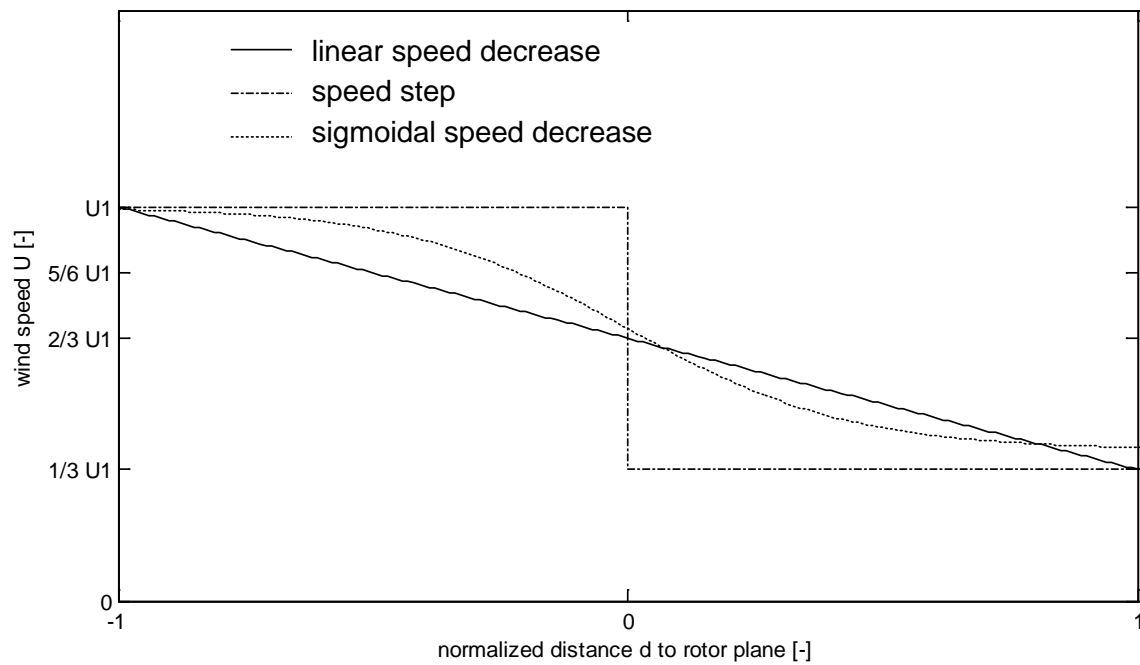
Figure 3-2: Estimation of wind speed decrease in front of a rotor

3.1.2   Stochastic Wind Field Evolution

Besides the discussed deterministic behaviour upwind a wind turbine, there are macroscopically unpredictable turbulent effects everywhere in air flow. Predictability of two signals with same amplitude in this regard refers to a degree of similarity of upstream wind speed measurements to (later) downstream measurements. As a measure for this degree, often the characterisation by two measures is proposed: the so called spectral coherence and the phase. If two measurements upstream and downstream are linear dependent, i.e. very similar, the coherence tends towards 1, whereas a low degree of similarity is expressed by coherence values tending towards 0. Mathematically, coherence of two signals a and b is given by

$$\gamma_{ab} = \frac{|\Phi\{R_{ab}(t)\}|^2}{|\Phi\{a(t)\}|^2\,|\Phi\{b(t)\}|^2},$$

(3.1)

where R_{ab} denotes the cross-correlation of the signals a and b and $\Phi\{\cdot\}$ is the Fourier transform operator. Thus spectral coherence is the magnitude of the cross spectrum, normalized by the power spectral densities of the two signals and expresses the linear dependency of two signals as a function of frequency.

The second measure of similarity of two signals is the linearity of their phase and the frequency, where phase φ_{ab} is given by

$$\varphi_{ab} = \arctan\left(\frac{\mathrm{Im}\{\Phi\{R_{ab}(t)\}\}}{\mathrm{Re}\{\Phi\{R_{ab}(t)\}\}}\right).$$

(4.1)

For frequency ranges where phase and frequency behave linearly, turbulent structures can be assumed to travel with the mean wind speed and can therefore be predicted at a downstream location.

If the coherence approaches 1 and the phase is observed to be linear with frequency, the air flow is called "frozen turbulence", since all turbulent structures do not change, and the so-called Taylor assumption is valid [53].

To analyse this effect, the spectral coherence and phase of wind speed measurements separated in stream direction have been analysed for different separation distances and have been presented in [54] [55] and [56]. The measurements are based on experimental data of a horizontal lidar in 125 meters above ground, without the influence of a wind turbine. Pulsed lidar signals are gathered simultaneously from different range gates and compared to an ultrasonic anemometer signal.. Coherence and phase are exemplarily shown in Figure 3-3 for a separating distance of 20 meters. They are plotted semi-logarithmically versus the wavenumber $k = 2\pi f/\overline{U}$, i.e. the frequency normalized by the mean wind speed $\overline{U}$. To ensure that the lidar system is able to capture turbulence structures within the analysed wavenumber range, the power spectrum of the measured wind speed can be analysed. The power spectrum, or power spectral density, decomposes a signal

into contributions from different frequencies or wavenumbers. In [57] the power spectra of the regarded lidar system are presented and compared to a reference power spectrum of a high accurate ultrasonic anemometer. This lidar is able to capture structures up to the noise level around the wavenumber 0.1 m^{-1}, but reduces the signal power at wavenumbers above 0.01 m^{-1} to 0.02 m^{-1} due to the spatial averaging effect. In a study of Angelou et al. [58] on a later version of the cw lidar, the detection of turbulent fluctuations up to wavenumbers between 0.1 and 0.2 m^{-1} was demonstrated.

Analysing the coherence and the phase it can now be observed that for small wavenumbers or frequencies, the coherence tends towards 1 and the phase follows the linear trend, while high frequent wind speed fluctuations are less correlated. Moreover, an upper wavenumber limit $k*$ of coherent and in-phase signals can be derived. Phase seems to be more suited to derive wavenumber limits than coherence, due to the abrupt detachment of the linear behaviour.
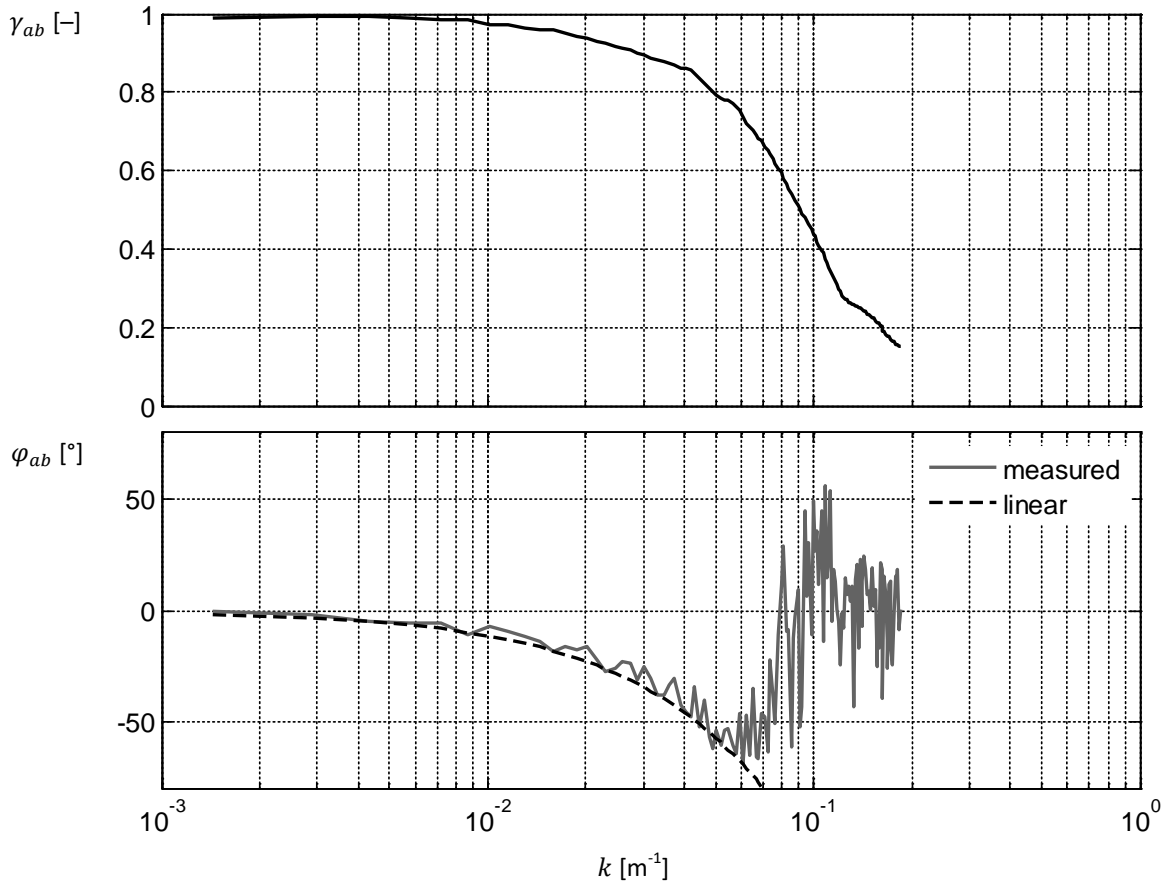
Figure 3-3: Spectral coherence and phase of two measured longitudinal wind speed signals $a(t)$ and $b(t)$ separated by 20 meters in inflow direction, as a function of wavenumber k.
Up to a wavenumber limit of $k* \approx 0.06$ m^{-1}, the phase is linear with wavenumber and frequency, and coherence exceeds 0.7.
During the period of 3000 s, mean wind speed was 7.26 m/s and turbulence intensity 5.5%.

Accordingly, wavenumber limits for different separation distances can be determined. The resulting dependence in Figure 3-4 suggests that at short distances and small wavenumbers, turbulence structures practically can be predicted (area below the curve).

The method offers a quantitative formulation of the similarity of wind speed signals and a practical distinction into predictable and stochastic (unpredictable) wind evolution in terms of frequency and distance. However, the relation will vary with the lidar technology and the measurement volume. A larger measurement volume will e.g. result in lower wavenumber limits and thus a smaller predictable range. Also different environmental conditions should be studied in more depth. Nevertheless, the results will exemplarily be used in the filter design process presented in Chapter 6.1.6.
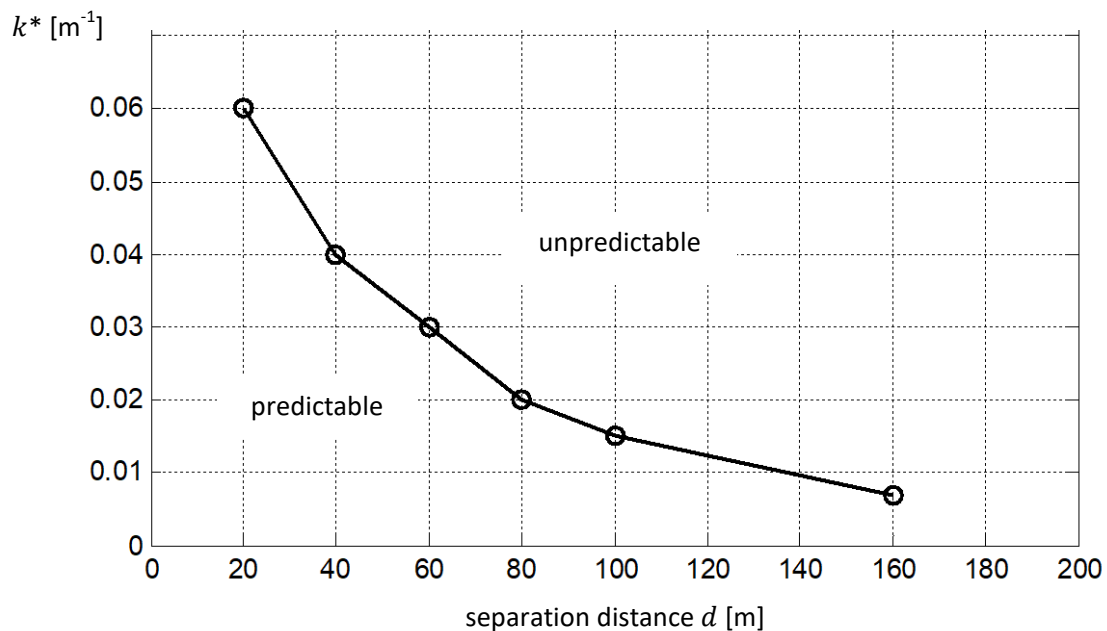
Figure 3-4: Wavenumber limit $k*$ experimentally determined for different separation distances d.

3.2   Sensor Constraints

The sensor system itself restricts the dimensional, spatial and temporal resolutions of the measurement. Here, a scanning single-beam lidar is considered. It can also be replaced by multiple fixed oriented lidar beams or can be transferred to similar remote sensing technologies.

3.2.1 Dimensional Limitation

The tightest restriction of single-beam based remote sensing technology results from the measurement of the component in beam direction, confer Figure 2-2. Measurements in beam direction are often referred to as line-of-sight measurements in the literature.

If the beam is oriented parallel to the direction of the local wind vector inside the probe volume, the obtained signal represents the true wind speed, while in all other scenarios the measured speed is smaller by a factor of $\cos\alpha$, where α denotes the misalignment angle. Lidar measurement errors due to this effect have been investigated in e.g. [59], where it was found that large scan opening angles, dominantly reduce the coherence of measured and predicted wind speed.

Moreover, from these measurements, the characterisation of the wind field might not be possible uniquely. The limitation and resulting interpretation ambiguities concerning lidars have been formulated in 2009 by Schlipf [60] and Bingöl et al. [61] and is sometimes referred to as Cyclops dilemma.

The problem is illustrated in Figure 3-5: A turbine mounted lidar measures two horizontal line-of-sight wind speeds in a fixed remote distance, v_1 and v_2. In the left figure, linear horizontal shear occurs, resulting in a larger wind speed measurement referring to the left beam compared to the right beam. The same measurements are obtained in the situation in the right figure, but caused by homogeneous horizontal inflow direction and zero shear. Consequently, horizontal (and respectively vertical) shear and direction parameters cannot be estimated concurrently and uniquely by beam measurements in one distance.

In Chapter 4, methods to overcome the reconstruction ambiguities are developed.
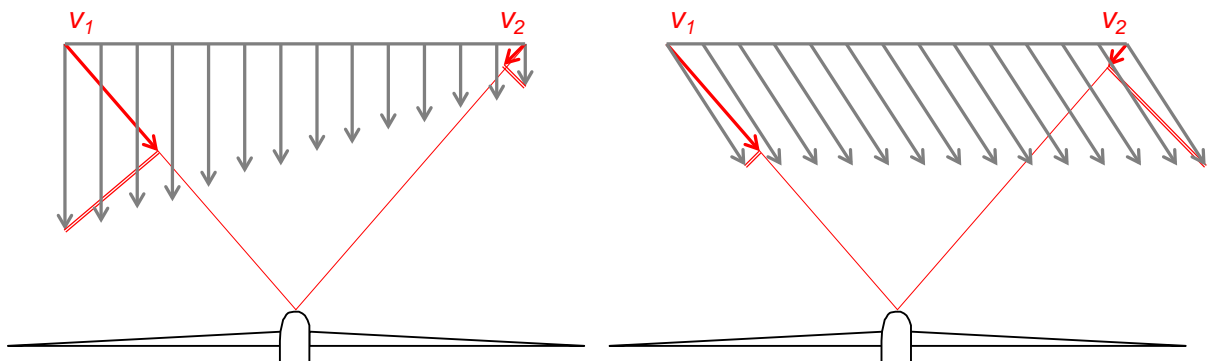
Figure 3-5: Ambiguity in remote wind field reconstruction assuming one beam source location and measurements in one plane.
Exemplarily, for two different inflow situations, one with horizontal shear (left) and one with horizontal direction (right), the remotely measured wind speeds v_1 and v_2 are identical. Hence, from the measurements, the different horizontal inflow characteristics cannot be distinguished.

3.2.2 Backscatter Spectrum Broadening

To determine the line-of-sight wind speed the correct interpretation of the backscatter spectrum is essential. While in laboratory conditions extreme narrow peaks can occur [62], enabling perfect interpretation as certain line-of-sight wind speed, in practical applications, spectrum interpretation is often less clear. Multiple peaks can occur due to beam reflections at hard targets or clouds, which have to be filtered out. Moreover, the thinness of backscatter spectrum peaks is limited.

According to [63] the thinness is influenced by the lidar itself and the wind conditions: The Fourier transform bin width and the scanning transit-time broaden the peak. Both can be reduced by the design of the lidar. For a current cw lidar this effect is in the order of 200 kHz each and of minor relevance. Wind conditions within the probe volume can contribute to the spectrum peak broadening by turbulent wind speed variations or by regular wind speed differences, e.g. due to wind shear.

3.2.3 Spatial Averaging Effect

The spatial resolution of a lidar is inherently influenced by the focusing and sampling behaviour of the device. Backscattering as described in Subsection 2.4.1 occurs at aerosols distributed over a probe volume. The centre of the volume, the focus point, usually represents the location with highest backscatter probability, whereas the probability of backscattering from focus far locations tends towards zero. The obtained wind speed information is therefore a weighted spectrum of wind speeds and the interpreted overall wind speed is thus an average value for the considered probe volume. This effect has to be minded for example when calculating turbulence or standard deviations from lidar line-of-sight measurements, which are generally underestimated when omitting it.

According to [64] the probability of the beam of a continuous-wave lidar being scattered in a certain distance z can be approximated by the normalised Cauchy distribution

$$Q_{cw}(\mathrm{z}) = \frac{1}{\pi} \frac{z_R}{z_R^2 + z^2} \cdot 1 \text{ m},\qquad(3.1)$$

with z_R the Rayleigh length parameter being approximated by the quadratic function in the focus distance z_focus

$$z_R = \frac{4\lambda}{\pi d_t^2} z_\text{focus}{}^2,\qquad(3.2)$$

d_t being the lidar aperture diameter and λ the wave length.

Figure 3-6 shows the weighting functions of a cw lidar (ZephIR lidar regarded in Chapter 5) for the focus distances 38 m, 78 m and 98 m.

Spatial averaging has to be explicitly modelled for realistic simulations as considered in the Subsection 6.1.3. As will be seen, averaging of inflow wind speed measurements is inevitable for use for control, and therefore spatial averaging can be a positive contribution.
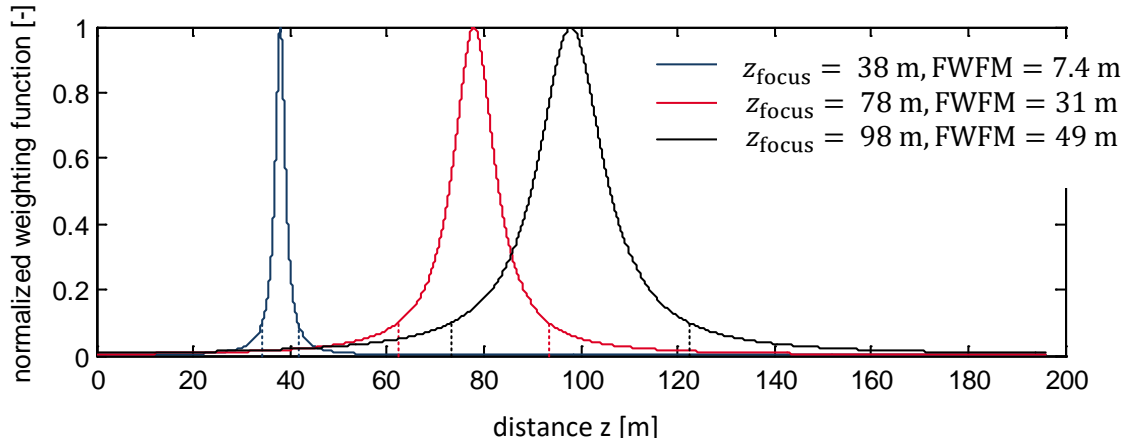
Figure 3-6: Normalized spatial weighting functions of the ZephIR lidar at three focus distances along with the functions' full widths (dashed to dashed, FWFM) at 10% of the maximum.

3.2.4 Temporal Resolution and Availability

A lidar's temporal resolution is limited by the sampling frequency and the speed of a possible scanner. With sampling rates currently up to 500 Hz [65], continuous-wave lidars theoretically seem suited for all wind energy applications in terms of speed. Practically, single measurements can be useless due to beam reflections, unfavorable weather conditions or other sources of weak signal-to-noise ratios (SNR). By aggregating fast sampled signals, data loss due to low SNR can be reduced significantly.

Data availability of lidars is most often analysed for ten-minute averages, which is a scale relevant for yaw control, performance monitoring and site assessment.

In literature, availability quotas of 95 to 99 percent are named [66] for at least 100 valid values within 10 minutes, applying a sampling rate of 50 Hertz. The most relevant atmospheric constraints are

- strong precipitation with droplet sizes of more than 2.5 millimetres

- cloud scattering (mostly studied for vertical lidars).

Dense fog with sight distances below 100 meters can occur extremely seldom at wind speeds exceeding 10 meters per second [67], which is the lower boundary of the relevant wind speed region for pitch control. Too low aerosol concentration are

neither said to significantly contribute to data losses, but comprehensive studies are rarely available.

Data availability for higher sampling rates in the range of one Hertz is rarely analysed so far, especially for the relevant influencing factors strong precipitation and cloud scattering.

In Subsection 5.2.3 the signal availability of experimental data of a turbine mounted scanning lidar during a period of 170 hours is analysed.

3.3   Control Requirements

The different wind energy applications which can be addressed with turbine mounted lidars result in different requirements on a lidar regarding sampling rate, scanning possibilities and availability.

Lidar-based individual feedforward blade pitch control (IFF) aims at helping reducing loads on the components by individually adjusting the blade pitch angles. IFF can be assumed to be most demanding in all three categories. The temporal resolution of vertical shear information can be useful up to once or twice the rotational speed (1P, 2P), which can e.g. be in the order of 0.2 to 0.6 Hz for a 2.5 MW wind turbine. Each shear update requires rotor plane distributed wind speed information, for vertical shear at least measurements taken above and below the hub height. The reduction of loads induced by horizontal shear, which often occurs within wind farms, requires at least two additional measurements left and right respectively.

Lidar based collective feedforward blade pitch control (CFF) aims at improving the speed limitation at above rated conditions. Collective speed control has most influence on frequencies below 1P. Scanning and averaging over the rotor plane is useful, because the whole wind field influences the speed. In literature, the order of ten distributed measurements per second is given [68].

Yaw control of current wind turbines is distinctly slower than the above control loops. Commonly, the rotation of the nacelle about the tower axis is limited to 0.5°/s to keep gyroscopic moments low. Also, the number of yaw actions is limited, depending on the directional deviation, in the order of 1 per 20s [69].

4   Modelling and Reconstruction of Inflow Wind Field Measurements

Modelling in engineering science is the process of describing systems using the mathematical notation with a reduced complexity, so that the relevant system behaviour is captured. Here, the focus is on the reduction of the wind speed distribution within a wind field to a finite number of wind field characteristics, referred to as wind field parameters in the following, to understand turbine inflow and especially provide input signals for controls. Next, the problem is formulated to calculate these wind field parameters from a limited subset of information, i.e. from turbine mounted lidar measurements. The solution of this problem will be referred to as lidar based wind field parameter reconstruction and will turn out to have a significant dependency on the geometry of the lidar measurements, as well as on the model that is used.

The two steps modelling and reconstruction are described for three wind field parameters in Section 4.1 and developed for five parameters in Section 4.2. The two approaches are compared applying a Monte Carlo Simulation and the results are discussed in Section 4.4.

4.1   Three Parameter Wind Field Models and Reconstruction

When assuming a turbine mounted lidar measuring in other directions rather than horizontally staring, additional output of the system besides averaged wind speed is needed for some applications. Scanning to the left and right might provide direction information, up and down vertical shear signals. First commercial turbine mounted lidars are specified to output up to three wind field parameters, so that they are applicable, whereas so far their accuracy has not been proven in studies for often.

4.1.1   Three Parameter Wind Field Models

In [70] Schlipf et.al. introduced concepts using three parameters to model wind fields. All relevant three parameter models include averaged wind speed, one parameter in horizontal and one in vertical direction. This second and third parameters can for example be shear or direction, but it appears disadvantageous to formulate models using two horizontal (or two vertical) parameters. This important constraint is derived from the understanding of ambiguities in wind field reconstruction assuming one lidar beam source location. As mathematically proven in [70], shear and direction both horizontally or both vertically cannot be reconstructed uniquely. In Subsection 3.2.1 the "line-of-sight limitation" introduces the reconstruction ambiguities.

Following this constraint, there are two favourable three parameter models derived to describe the wind speed vector field $\vec{v}$ in u-, v- and w-components as a function of rotor plane coordinates y and z:

1. Linear shear model including averaged wind speed u_0, horizontal and vertical shear s_h and s_v.

$$\vec{v}(y,z) = (u_0 + s_h y + s_v z) \begin{bmatrix} 1 \\ 0 \\ 0 \end{bmatrix} \qquad (4.1)$$

   This model assumes both a vertical and a horizontal linear variation of the wind speed over the rotor plane and no wind direction deviation from the u-direction towards the rotor. The assumptions are fulfilled if yawing errors are implied minor, vertical wind direction can be neglected and further nonlinear effects like spatially occurring turbulence are small. In flat terrain these conditions often occur. Also, wind farm wake effects can approximatively be captured by the shear parameters. However, varying upflow is not included, e.g. at mountainous sites.

   The model can easily be extended by known wind direction offsets $\delta_{h,fixed}$, $\delta_{v,fixed}$

$$\vec{v}(y,z) = (u_0 + s_h y + s_v z) \begin{bmatrix} \cos(\delta_{v,fixed})\cos(\delta_{h,fixed}) \\ \cos(\delta_{v,fixed})\sin(\delta_{h,fixed}) \\ \sin(\delta_{v,fixed}) \end{bmatrix}, \qquad (4.2)$$

   for example to take into account a known rotor tilt angle or known yaw errors.

2. Nonlinear shear and direction model parameterized by wind speed u_0, vertical shear s_v and horizontal direction δ_h:

$$\vec{v}(y,z) = (u_0 + s_v z) \begin{bmatrix} \cos(\delta_h) \\ \sin(\delta_h) \\ 0 \end{bmatrix} \qquad (4.3)$$

   This model seems most useful for practical applications due to its significance for yaw control and based on the assumption that vertical shear and horizontal direction signals dominate the wind field characteristics. In flat terrain with undisturbed inflow these assumptions can be fulfilled, while wake effect and upflow is not captured.

Corresponding models including an upflow parameter but no vertical shear parameter are less useful for practical applications. The reason is the typical occurrence of vertical shear due to the aerodynamic drag at the surface within the planetary boundary layer.

4.1.2 Three Parameter Reconstruction

Reconstruction of the parameterized wind field models requires the formulation and solving of equations comprising i remote wind speed measurements v_i and the parameters to be determined. In the following, the use of a continuous-wave scanning lidar with below characteristics is assumed:

- The lidar is located in the centre of the rotor and deviations of this position are considered small compared to the rotor diameter.

- The rotor tilt angle has no effect on the measurements, because the vertical inclination of the beam orientation is considered and the longitudinal shift of measurement points is smaller than the length of the probe volume.

- The approaching distance of the wind field during one scan is small compared to the probe volume. This applies if one full scan is finished very fast. Then, all measurements can be considered coinstantaneous.

- The movement of the laser beam within the duration of backscatter signal receiving is small compared to the probe volume. The measurements at the discrete scanning positions can then be regarded as using a fixed beam orientation for this measurement.

- The measurements are taken in a fixed axial distance from the rotor. If spherical measurements are to be analysed, the axial separation is considered small compared to the probe volume.

Then, a set of n coinstantaneous remote measurements with beam scattering directions $\vec{b}_i$ at a fixed horizontal distance $x = \xi$: $\vec{b}_i = [\xi \quad -y_i \quad -z_i]$ are assumed.

The formulation of the orthogonal projections $\vec{v}_{l,i}$ of wind vectors $\vec{v}_i$ on beam directions $\vec{b}_i$ give

$$\vec{v}_{l,i} = \frac{\vec{v}_i \cdot \vec{b}_i}{\vec{b}_i \cdot \vec{b}_i} \, \vec{b}_i$$

$$\Leftrightarrow |\vec{v}_{l,i}| = \frac{\vec{v}_i \cdot \vec{b}_i}{|\vec{b}_i|} = \frac{1}{|\vec{b}_i|} \vec{v}_i \cdot \begin{bmatrix} \xi \\ -y_i \\ -z_i \end{bmatrix} \tag{4.4}$$

and result in the requested equations of measured wind speeds and parameters, depending on the two models introduced in Section 4.1.1:

$$(1) \quad |\vec{v}_{l,i}| = \frac{1}{|\vec{b}_i|}(u_0 + s_h y_i + s_v z_i) \begin{bmatrix} 1 \\ 0 \\ 0 \end{bmatrix} \cdot \begin{bmatrix} \xi \\ -y_i \\ -z_i \end{bmatrix} \tag{4.5}$$

$$= \frac{1}{|\vec{b}_i|} \underbrace{[\xi \quad \xi y_i \quad \xi z_i]}_{A_1} \underbrace{\begin{bmatrix} u_0 \\ s_h \\ s_v \end{bmatrix}}_{x}$$

$$
(2) \quad |\vec{v}_{l,i}| = \frac{1}{|\vec{b}_i|} (u_0 + s_v z_i) \begin{bmatrix} \cos(\delta_h) \\ \sin(\delta_h) \\ 0 \end{bmatrix} \cdot \begin{bmatrix} \xi \\ -y_i \\ -z_i \end{bmatrix}
$$

$$
= \frac{1}{|\vec{b}_i|} (\xi u_0 \cos(\delta_h) + \xi z_i s_v \cos(\delta_h) \tag{4.6}
$$

$$
- y_i u_0 \sin(\delta_h) - y_i z_i s_v \sin(\delta_h))
$$

Reconstruction based on the linear wind field model results in a system of linear Equations (4.5) in the variables u_0, s_h and s_v. It can be solved if the rank of matrix A_1 equals three. If three measurements are used, the solution is unique, which is satisfied for example for three measurement directions at 120° azimuth offset.

In case of more than three measurements and $\mathrm{rank}(A_1) = 3$ a method to minimize the quadratic error $\left\| A_1 x - |\vec{v}_{l,i}| |\vec{b}_i| \right\|_2$ can be applied, for example the generalized (right) inverse $A_1^+ = A_1^T (A_1 A_1^T)^{-1}$ can be used to determine the solution [71]. In terms of the minimized quadratic error this solution is also unique regardless the calculation algorithm.

The nonlinear wind field model (4.3) results in a problem formulated in the nonlinear Equations (4.6) to determine the unknown parameters u_0, s_v and δ_h. Here the use of an optimization method is required for fitting the model to at least three measurements. Calculations of this kind have been successfully applied in practical applications, see e.g. [72].

4.2   Five Parameter Wind Field Model and Reconstruction

Recently a new five parameter inflow model was proposed in [73]. Two sensing principles for estimating the parameters of this model are presented here, based on the assumption of one and two measurement distances respectively. This results in two different reconstruction methods, each elaborated in one of the next subsections.

4.2.1   Five Parameter Wind Field Model

Five parameters are proposed to characterise the mean behaviour of a three dimensional wind vector field within a two dimensional plane $x = 0$ in front of the turbine:

mean wind speed u_0 [m/s]	vertical shear s_v [m/s /m]	vertical direction δ_v [°]	horizontal shear s_h [m/s /m]	horizontal direction δ_h [°]
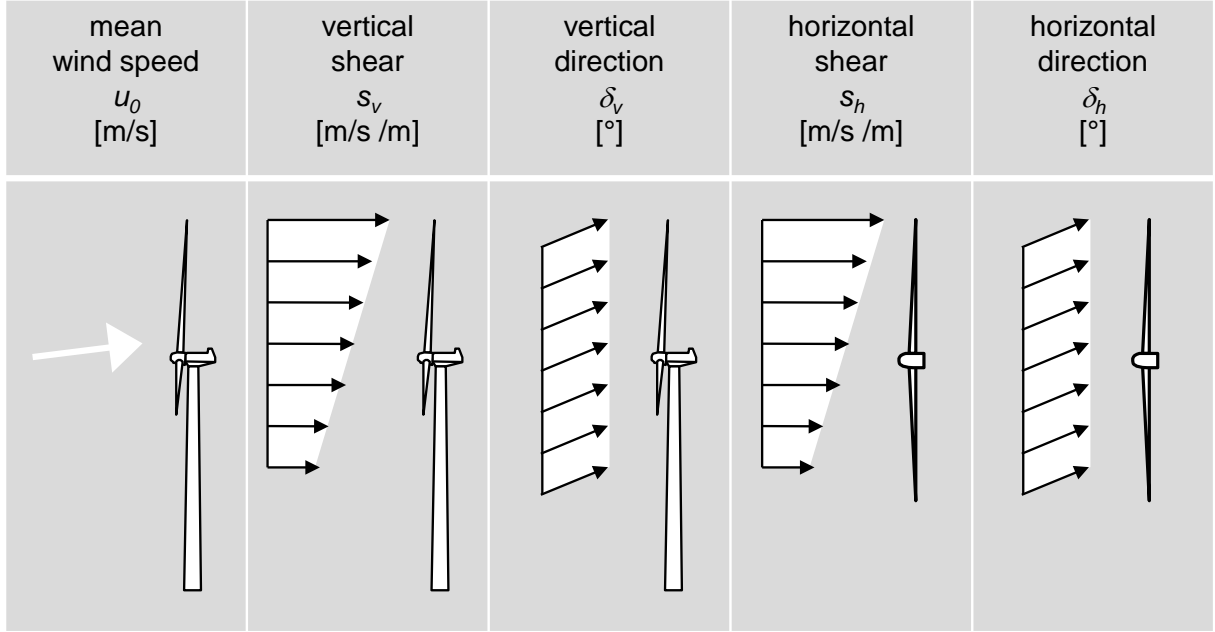
Figure 4-1: Considered set of five parameters describing the inflow.

The rotor plane averaged wind speed u_0 is aligned with the rotor plane averaged wind directions δ_h and δ_v. The shear values s_h and s_v describe the slope of linearly ascending wind speeds in y- and z-direction respectively.

The choice of the five parameters is motivated by the capabilities of wind turbines to react to wind conditions: The averaged wind speed is relevant for rotor speed and collective pitch action, the horizontal wind direction influences the yaw orientation, and shear and direction can be regarded in individual pitch control.

According to the model, wind vectors $\vec{v}$ are then given depending on their position (y, z) in the wind field plane by the nonlinear model

$$\vec{v}(y, z) = (u_0 + s_\mathrm{h}y + s_\mathrm{v}z) \begin{bmatrix} \cos(\delta_\mathrm{v})\cos(\delta_\mathrm{h}) \\ \cos(\delta_\mathrm{v})\sin(\delta_\mathrm{h}) \\ \sin(\delta_\mathrm{v}) \end{bmatrix} \tag{4.7}$$

4.2.2 Five Parameter Reconstruction using Two Measurement Distances

In addition to the assumptions of the three parameter reconstruction of subsection 4.1.2, in the following the simultaneous acquisition of measurements in a plane at a second axial distance is assumed respectively. Particularly, it is assumed that the Taylor's frozen turbulence hypothesis [53] is fulfilled, i.e. that the wind field doesn't change while travelling between the two measurement distances.

In the following, two-dimensional wind speed information in measurement planes upwind the turbine as illustrated in Figure 4-3 are assumed to be given.The information may be obtained either

- by focusing two lidar beams on one measurement point, the beams originating from two positions on the x-axis, cf. Figure 4-2 a) or

- by focusing one lidar beam subsequently on two upwind positions, the focus points being separated in x-direction, cf. Figure 4-2 b).

While the first method requires two lidar beams and the ability to place their radiation outlets significantly separated in x-direction, the second method needs one beam outlet only but requires refocusing and/or re-adjusting of the scan direction. Regardless the actual way of acquiring the two-dimensional wind speed information in the measurement plane, the respective reconstruction method is called "two distance reconstruction" here, because using two axially separated measurement distances, and applying Taylor's frozen turbulence hypothesis, currently seems the most practical way.

Assuming now that two measurements $\vec{v}_{1,i}$ and $\vec{v}_{2,i}$ in beam direction in each measurement plane P_i are given, a corresponding vector $\vec{m}_i$ lying in plane P_i can be calculated, so that $\vec{v}_{1,i}$ and $\vec{v}_{2,i}$ are orthogonal projections of $\vec{m}_i$, see Figure 4-2 c).

This is fulfilled, if the following two dot products are zero:

$$\langle \vec{v}_{1,i}, (\vec{m}_i - \vec{v}_{1,i}) \rangle = 0$$
$$\langle \vec{v}_{2,i}, (\vec{m}_i - \vec{v}_{2,i}) \rangle = 0$$

(4.8)

As the vector $\vec{m}_i$ is lying in plane P_i it can be expressed as a linear combination of $\vec{v}_{1,i}$ and $\vec{v}_{2,i}$

$$\vec{m}_i = \lambda_{1,i} \vec{v}_{1,i} + \lambda_{2,i} \vec{v}_{2,i}$$

(4.9)

with scalars $\lambda_{1,i}$ and $\lambda_{2,i}$.

Inserting (4.9) into (4.8) gives

$$\langle \vec{v}_{1,i}, (\lambda_{1,i} \vec{v}_{1,i} + \lambda_{2,i} \vec{v}_{2,i} - \vec{v}_{1,i}) \rangle = 0$$
$$\langle \vec{v}_{2,i}, (\lambda_{1,i} \vec{v}_{1,i} + \lambda_{2,i} \vec{v}_{2,i} - \vec{v}_{2,i}) \rangle = 0$$
$$\Leftrightarrow \underbrace{\begin{bmatrix} \langle \vec{v}_{1,i}, \vec{v}_{1,i} \rangle & \langle \vec{v}_{1,i}, \vec{v}_{2,i} \rangle \\ \langle \vec{v}_{2,i}, \vec{v}_{1,i} \rangle & \langle \vec{v}_{2,i}, \vec{v}_{2,i} \rangle \end{bmatrix}}_{A} \begin{bmatrix} \lambda_{1,i} \\ \lambda_{2,i} \end{bmatrix} = \begin{bmatrix} \langle \vec{v}_{1,i}, \vec{v}_{1,i} \rangle \\ \langle \vec{v}_{2,i}, \vec{v}_{2,i} \rangle \end{bmatrix}$$

(4.10)

representing a system of two linear equations to determine $\lambda_{1,i}$ and $\lambda_{2,i}$.

The system has one solution if the determinant of A is not zero:

$$\det A \neq 0$$

$$\Leftrightarrow \ \langle \vec{v}_{1,i}, \vec{v}_{1,i} \rangle \cdot \langle \vec{v}_{2,i}, \vec{v}_{2,i} \rangle - \langle \vec{v}_{2,i}, \vec{v}_{1,i} \rangle \cdot \langle \vec{v}_{1,i}, \vec{v}_{2,i} \rangle \neq 0$$

$$\Leftrightarrow \ \left| \vec{v}_{1,i} \right|^2 \left| \vec{v}_{2,i} \right|^2 \neq \left| \langle \vec{v}_{1,i}, \vec{v}_{2,i} \rangle \right|^2 \qquad (4.11)$$

(4.11) is fulfilled if and only if $\vec{v}_{1,i}$ and $\vec{v}_{2,i}$ are nonparallel and not zero, according to the Cauchy–Schwarz inequality.

Calculating $\lambda_{1,i}$ and $\lambda_{2,i}$ by solving (4.10) and inserting into equation (4.9) finally results in the projections $\vec{m}_i$.

On the other hand, the vectors $\vec{m}_i$ can be interpreted as the orthogonal projections of the three dimensional wind speed vectors $\vec{v}(y_i, z_i)$ to planes P_i and will hence be referred to as projection measurements $\vec{m}_i$ in the following. $\vec{m}_i$ can be expressed by using the wind speed vector $\vec{v}$ by

$$\vec{m}_i = \begin{bmatrix} m_{u,i} \\ m_{v,i} \\ m_{w,i} \end{bmatrix} = \langle \vec{v}, \vec{e}_u \rangle \vec{e}_u + \langle \vec{v}, \vec{e}_i \rangle \vec{e}_i \qquad (4.12)$$

The measurement planes are thereby spanned by the unit vectors

$$\vec{e}_u = \begin{bmatrix} 1 \\ 0 \\ 0 \end{bmatrix} \text{ and } \vec{e}_i = \begin{bmatrix} 0 \\ e_{v,i} \\ e_{w,i} \end{bmatrix} \qquad (4.13)$$

respectively, which can be constructed pairwise orthonormally, i.e. $\langle \vec{e}_u, \vec{e}_i \rangle = 0$ and $|\vec{e}_i| = 1 \ \ \forall i$. This implies that $e_{v,i}^2 + e_{w,i}^2 = 1$, meaning that the unit vectors are on the unit circle in the v-w-plane.

In the next subsection three of the projection measurements $\vec{m}_i$ are used to reconstruct a wind field as modelled above, comprising five parameters averaged in the inflow plane.
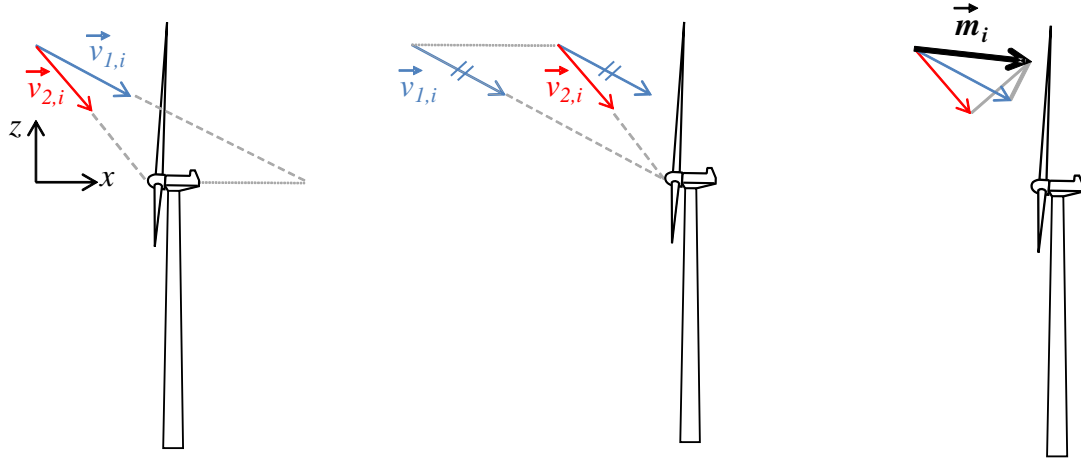
Figure 4-2: Determination of the wind vector projection

a): Two lidar beams (dashed), both focused on one point, the outlets being separated in x-direction.

b): Refocusing lidar setup, subsequently measuring $v_{1,i}$ and $v_{2,i}$.
$v_{1,i}$ is shifted in time and assumes perfect approach to the second measurement distance.

c): The wind vector projection $\vec{m}_i$ (bold) is the intersection of the orthogonal lines (grey) to the measurements $v_{1,i}$ and $v_{2,i}$ in beam direction.
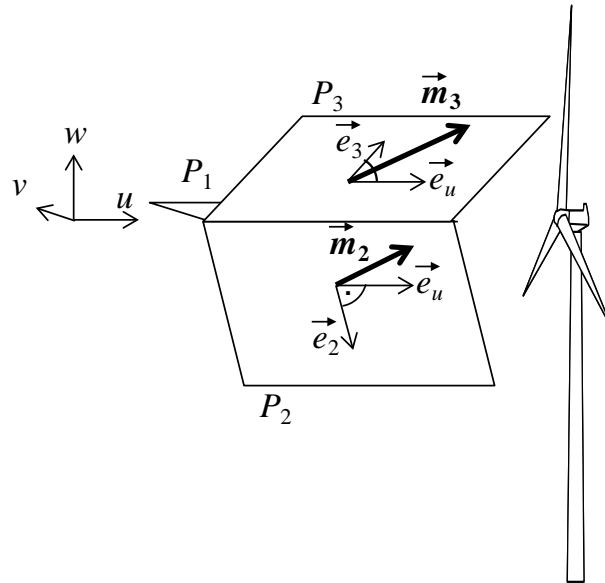
Figure 4-3: Measurement planes P_i, spanned by vectors $\vec{e}_u$ and $\vec{e}_i$, containing two-dimensional projection measurements $\vec{m}_i$.

Wind Field Reconstruction using Three Measurement Planes

Now, three measurement planes are assumed to be non-parallel and are spanned by $\vec{e}_u = \begin{bmatrix} 1 & 0 & 0 \end{bmatrix}^{\mathrm{T}}$ and

$$\vec{e}_1 = \begin{bmatrix} 0 \\ e_{v,1} \\ e_{w,1} \end{bmatrix}, \vec{e}_2 = \begin{bmatrix} 0 \\ e_{v,2} \\ e_{w,2} \end{bmatrix} \text{ and } \vec{e}_3 = \begin{bmatrix} 0 \\ e_{v,3} \\ e_{w,3} \end{bmatrix} \tag{4.14}$$

respectively, which can be constructed pairwise orthonormally, i.e. $\langle \vec{e}_u, \vec{e}_i \rangle = 0$ and $|\vec{e}_i| = 1 \ \ \forall i$.

The wind speed at position (y_i, z_i) is assumed to be given by the five parameter model (4.7). The projections $\vec{m}_i$ with components $[m_{u,i}, m_{v,i}, m_{w,i}]$, $i = \{1,2,3\}$ are assumed to be determined by the measured wind speeds $\vec{v}_{1,i}$ and $\vec{v}_{2,i}$ in beam directions, and applying equations (4.9) and (4.10).

Model (4.7) can then be inserted into the projection definition (4.12):

$$\begin{bmatrix} m_{u,i} \\ m_{v,i} \\ m_{w,i} \end{bmatrix} = \langle \vec{v}, \vec{e}_u \rangle \vec{e}_u + \langle \vec{v}, \vec{e}_i \rangle \vec{e}_i$$

$$= (u_0 + s_{\mathrm{h}} y_i + s_{\mathrm{v}} z_i) \begin{bmatrix} \cos(\delta_{\mathrm{v}}) \cos(\delta_{\mathrm{h}}) \\ e_{v,i}^2 \cos(\delta_{\mathrm{v}}) \sin(\delta_{\mathrm{h}}) + e_{v,i} e_{w,i} \sin(\delta_{\mathrm{v}}) \\ e_{v,i} e_{w,i} \cos(\delta_{\mathrm{v}}) \sin(\delta_{\mathrm{h}}) + e_{w,i}^2 \sin(\delta_{\mathrm{v}}) \end{bmatrix} \tag{4.15}$$

The evaluation of the equation (4.15) for $i = \{1,2,3\}$ produces a system of nine nonlinear equations for the five unknown parameters.

In the following it is demonstrated that these nine equations are sufficient to solve the problem.

Without loss of generality it is assumed that $e_{v,1} = 1$ and $e_{w,1} = 0$, i.e. the first measurement plane is oriented horizontally as illustrated in Figure 4-3.

Then from (4.15) the three equations for $\vec{m}_1$ become

$$\begin{bmatrix} m_{u,1} \\ m_{v,1} \\ m_{w,1} \end{bmatrix} = (u_0 + s_{\mathrm{h}} y_1 + s_{\mathrm{v}} z_1) \begin{bmatrix} \cos(\delta_{\mathrm{v}}) \cos(\delta_{\mathrm{h}}) \\ \cos(\delta_{\mathrm{v}}) \sin(\delta_{\mathrm{h}}) \\ 0 \end{bmatrix} \tag{4.16}$$

and can be condensed to

$$\tan(\delta_{\mathrm{h}}) = \frac{m_{v,1}}{m_{u,1}} \tag{4.17}$$

For $m_{u,1} \neq 0$ Equation (4.17) uniquely yields the direction δ_{h} within the range $\left(-\frac{\pi}{2}, \frac{\pi}{2} \right)$.

Analogously, an equation for the averaged vertical wind direction δ_v can be derived from the set of three equations of the second projection measurement $\vec{m}_2$ by dividing $m_{v,2}$ and $m_{u,2}$:

$$\tan(\delta_\mathrm{v}) = \frac{\left(\frac{m_{v,2}}{m_{u,2}} - e_{v,2}^2 \tan(\delta_\mathrm{h})\right) \cos(\delta_\mathrm{h})}{e_{v,2} e_{w,2}} \tag{4.18}$$

By inserting result (4.17) and using the trigonometric identity

$$\cos(\delta_\mathrm{h}) = \frac{1}{\sqrt{1 + (\tan(\delta_\mathrm{h}))^2}}, \quad \delta_\mathrm{h} \in \left(-\frac{\pi}{2}, \frac{\pi}{2}\right) \tag{4.19}$$

(4.18) results in

$$\tan(\delta_\mathrm{v}) = \frac{\frac{m_{v,2}}{m_{u,2}} - e_{v,2}^2 \frac{m_{v,1}}{m_{u,1}}}{e_{v,2} e_{w,2} \sqrt{1 + \left(\frac{m_{v,1}}{m_{u,1}}\right)^2}} \tag{4.20}$$

Equation (4.20) yields the vertically averaged wind direction δ_v if $e_{v,2}, e_{w,2} \neq 0$, i.e. if P_2 is not parallel or perpendicular to P_1. If P_2 is perpendicular to P_1, i.e. if $e_{v,2} = 0$, δ_v is given by

$$\tan(\delta_\mathrm{v}) = \frac{\frac{m_{w,2}}{m_{u,2}}}{\sqrt{1 + \left(\frac{m_{v,1}}{m_{u,1}}\right)^2}} \tag{4.21}$$

As an intermediate result it can be observed that two projection measurements $\vec{m}_1, \vec{m}_2$ on two arbitrarily turned measurement planes which are not parallel are sufficient to derive both the horizontally and vertically averaged wind directions δ_h and δ_v, each in the range $\left(-\frac{\pi}{2}, \frac{\pi}{2}\right)$.

To calculate the parameters u_0, s_h and s_v the equations from the u-component in Equation (4.15) for $i = \{1, 2, 3\}$, yield a set of linear equations

$$\begin{bmatrix} 1 & y_1 & z_1 \\ 1 & y_2 & z_2 \\ 1 & y_3 & z_3 \end{bmatrix} \begin{bmatrix} u_0 \\ s_h \\ s_v \end{bmatrix} = \frac{1}{\cos(\delta_h)\cos(\delta_v)} \begin{bmatrix} m_{u,1} \\ m_{u,2} \\ m_{u,3} \end{bmatrix} \tag{4.22}$$

The linear equation (4.22) has exactly one solution if the determinant of the coefficient matrix is unequal to zero. It can be shown that this is always the case if the direction of the three measurement beams are linearly independent. This holds in

particular if the measurement points (y_1, z_1), (y_2, z_2) and (y_3, z_3) are located at different positions on a circle.

Using (4.17), (4.20) and (4.22) all five wind field parameters can be calculated assuming three projection measurements $\vec{m}_i$ in three measurement planes, whereas at least two planes need to be nonparallel. The average wind direction requires two projection measurements from two nonparallel planes only.

In this subsection, nine nonlinear equations (4.15) from three measurement planes were used to calculate five unknown parameters. These three planes are commonly necessary, only two planes can be insufficient. This can be observed when inserting the important special case $\delta_h = \delta_v = 0$ into (4.15) for $i = \{1, 2\}$.

Only two nontrivial equations remain,

$$m_{u,1} = u_0 + s_h y_i + s_v z_i$$

$$m_{u,2} = u_0 + s_h y_2 + s_v z_2$$

(4.23)

which do not enable the calculation of the three unknown parameters u_0, s_h and s_v.

Although in cases with nonzero wind directions the reconstruction of the parameters might be possible with two measurement planes only, in practical applications nonzero directions will always be within the scope of wind lidar measurements and hence necessitate a third measurement plane.

Wind Field Reconstruction using Multiple Measurement planes

If more than three projection measurements are available and can be assigned to one common wind field, reconstruction of the five wind field parameters can be improved and made more robust against in-wind-field turbulence, i.e. local deviations of wind speeds from the model.

For this purpose, two alternative solutions are proposed.

Firstly, the parameter estimation can be formulated as the optimization problem

$$\left\| \underline{\vec{m}} - \underline{\vec{f}}(\underline{x}) \right\|_2^2 \xrightarrow[\underline{x}]{} \min$$

(4.24)

where $\underline{\vec{m}}$ represents an array of n projection measurements $\vec{m}_i$, $n \geq 3$, and $\underline{\vec{f}}$ represents an array of n modelled projection measurements $\vec{f}_i(\underline{x})$, $\underline{x}$ being the vector of the five wind field parameters.

The problem (4.24) can be solved by varying the parameters $\underline{x}$ and minimizing the sum of squares of the differences between model and measurement. The Levenberg-

Marquardt and the Trust-region-reflective algorithm [74] give good numerical results. Disadvantageously, the speed and the local solution of nonlinear optimisation in general depend on the initial search values.

Secondly, as an alternative way, a quasi-linear formulation of the problem can be chosen to improve the calculation performance. Projection measurements are assumed to fulfil the projection measurement Equations (4.15). From the first equation in (4.15) it follows

$$u_0 + s_\mathrm{h}y_i + s_\mathrm{v}z_i = \frac{m_{u,i}}{\cos(\delta_v)\cos(\delta_h)}, \quad \delta_\mathrm{h} \in \left(-\frac{\pi}{2},\frac{\pi}{2}\right) \tag{4.25}$$

Inserting (4.25) in (4.15), equation 2, results in

$$m_{v,i}\cos(\delta_h) = e_{v,i}^2 m_{u,i}\sin(\delta_h) + e_{v,i}e_{w,i}m_{u,i}\tan(\delta_v) \tag{4.26}$$

which can be rearranged to the system of equations

$$\underbrace{\begin{bmatrix} e_{v,1}^2 & e_{v,1}e_{w,1} \\ \vdots & \vdots \\ e_{v,n}^2 & e_{v,n}e_{w,n} \end{bmatrix}}_{A_1} \begin{bmatrix} \tan(\delta_h) \\ \tan(\delta_v)\cos^{-1}(\delta_h) \end{bmatrix} = \underbrace{\begin{bmatrix} \frac{m_{v,1}}{m_{u,1}} \\ \vdots \\ \frac{m_{v,n}}{m_{u,n}} \end{bmatrix}}_{b_1} \tag{4.27}$$

Equation (4.27) represents a system of linear equations in the variables $\tan(\delta_h)$ and $\tan(\delta_v)\cos^{-1}(\delta_h)$ and can be solved if $\mathrm{rank}(A_1) = 2$, i.e. if the number of nonparallel measurement planes with components $e_v \neq 0$ is $n \geq 2$. If the components e_v of the nonparallel measurement planes are zero, equation 3 of system (4.15) can be used, producing the system

$$\underbrace{\begin{bmatrix} e_{v,1}e_{w,1} & e_{w,1}^2 \\ \vdots & \vdots \\ e_{v,n}e_{w,n} & e_{w,n}^2 \end{bmatrix}}_{A_2} \begin{bmatrix} \tan(\delta_h) \\ \tan(\delta_v)\cos^{-1}(\delta_h) \end{bmatrix} = \underbrace{\begin{bmatrix} \frac{m_{w,1}}{m_{u,1}} \\ \vdots \\ \frac{m_{w,n}}{m_{u,n}} \end{bmatrix}}_{b_2} \tag{4.28}$$

Efficient linear algebra computational algorithms like LAPACK [75] can be used.

As a result, the mean directions δ_h and δ_v are obtained uniquely, assuming $\delta_\mathrm{h}, \delta_\mathrm{v} \in \left(-\frac{\pi}{2},\frac{\pi}{2}\right)$.

From equation 1 in (4.15) a second system with variables u_0, s_h and s_v can be formulated

$$\underbrace{\begin{bmatrix} 1 & y_1 & z_1 \\ \vdots & \vdots & \vdots \\ 1 & y_n & z_n \end{bmatrix}}_{A_3} \begin{bmatrix} u_0 \\ s_h \\ s_v \end{bmatrix} = \frac{1}{\cos(\delta_h)\cos(\delta_v)} \underbrace{\begin{bmatrix} m_{u,1} \\ \vdots \\ m_{u,n} \end{bmatrix}}_{b_3} \tag{4.29}$$

and solved if $\mathrm{rank}(A_3) = 3$, i.e. if three independent measurement directions exist. Again, efficient algorithms can be used to calculate the solution with least error square.

Finally, mean wind speed in stream direction u_0 and vertical and horizontal shear values are obtained uniquely.

4.2.3   Five Parameter Reconstruction using a Single Measurement Distance

As introduced in the Section 3.2.1, the simultaneous determination of wind shear and direction from measurements taken in a single plane is affected by ambiguities and numerical issues. Nevertheless, here a method is developed to give the best possible reconstructed parameters using a single measurement plane. Its performance is compared to the reconstruction method based on two measurement planes.

Five Parameter Estimation

Wind vectors given by the five parameter model as in Equation (4.7) are assumed to be projected on conical lidar beam directions. The measured velocities v_l in beam direction depend on the azimuthal position θ of the scan and the five wind field parameters:

$$\begin{aligned} v_l(\theta) = \frac{1}{R}&(u_0 + s_h R_z \cos(\theta) + s_v R_z \sin(\theta)) \\ &[\cos(\delta_v)(R_x \cos(\delta_h) - R_z \cos(\theta)\sin(\delta_h)) - R_z \sin(\theta)\sin(\delta_v)] \end{aligned} \tag{4.30}$$

with R_z the radius of the measurement circle in the y-z-plane, R_x the measurement distance in x-direction, R the focus length.

Term (4.30) can be rewritten employing trigonometric identities to get

$$v_l(\theta) = \frac{1}{R}(a_1 + a_2 \cos(\theta) + a_3 \sin(\theta) + a_4 \sin(2\theta) + a_5 \cos(2\theta)) \tag{4.31}$$

where

$$\underline{a} = \begin{bmatrix} a_1 \\ a_2 \\ a_3 \\ a_4 \\ a_5 \end{bmatrix} = \begin{bmatrix} u_0 R_x \cos(\delta_h) \cos(\delta_v) - \dfrac{1}{2} s_h R_z^2 \sin(\delta_h) \cos(\delta_v) - \dfrac{1}{2} s_v R_z^2 \sin(\delta_v) \\ s_h R_x R_z \cos(\delta_h) \cos(\delta_v) - u_0 R_z \sin(\delta_h) \cos(\delta_v) \\ s_v R_x R_z \cos(\delta_h) \cos(\delta_v) - u_0 R_z \sin(\delta_v) \\ \dfrac{1}{2} R_z^2 (-s_v \sin(\delta_h) \cos(\delta_v) - s_h \sin(\delta_v)) \\ \dfrac{1}{2} R_z^2 (-s_h \sin(\delta_h) \cos(\delta_v) + s_v \sin(\delta_v)) \end{bmatrix} \tag{4.32}$$

are non-physical parameters. It can be proven that the parameterization of v_L by $\underline{a}$ is unique, so that in a first step $\underline{a}$ can be obtained using a least squares fit of the measurements $v_L(\theta)$.

In a second step, the physical wind field parameters have to be determined by solving the nonlinear Equation (4.32) which emerges to be numerically unstable due to multiple neighbouring solutions and large gradients. Also the suitable choice of initial values for the solving algorithm is important.

In the following section parameter reconstructions based on simulated measurements in a single measurement distance are performed and compared to reconstructions based on two measurement distances.

4.3   Wind Field Reconstruction Simulation

To evaluate and compare the two presented methods to reconstruct five wind field parameters from turbulent wind fields, firstly typical fluctuations of lidar measurements due to turbulence are analysed. Afterwards, the results are used to model turbulent measurements of synthetic wind fields. Finally, based on the turbulent measurements, the reconstruction algorithms to determine estimates of the wind field parameters are evaluated.

4.3.1   Wind Speed Fluctuations in Experimental Lidar Data

The wind speed fluctuations "seen" by a horizontal lidar are analysed using experimental data of a conical scanning continuous-wave ZephIR lidar mounted in the non-rotating spinner at hub height of 59 meters.

A timeseries of approximately 40 minutes with a sampling rate of 50 Hz, resulting in 115,175 conical measurements, was chosen. The turbulence intensities range from 7.6% to 10.1% and the vertical shear is smaller than 0.1 s^{-1}, which can be considered typical for this near shore site. For each 50 measurements of one conical scan, a unique parameter set $\underline{a}$ is calculated using a least squares fit of the 50 equations (4.31). The deviations Δv_l to the fitted model can then be calculated and are shown in the histogram in Figure 4-4. The deviations are found to fulfil the Kolmogorov-

Smirnov test [76] for normality in 75% of the samples and are therefore modelled as Gaussian distributed in the following.

Further, the turbulent fluctuations of the difference of measured velocities and modelled velocities in beam direction Δv_l during one conical scan are quantified and referred to as *conical turbulence intensity*, defined by

$$T_{I,c} = \frac{\sigma(\Delta v_l)}{\overline{v_L}}$$

(4.33)

with standard deviation $\sigma(\Delta v_l)$ and $\overline{v_l}$ indicating the mean velocity in beam direction, both with respect to all measurements during one conical scan.

This definition has the advantages of providing dynamic data (e.g. one intensity value per second), of representing rotor distributed information and of being independent of the current wind field parameters by regarding the deviations of the model and by normalising by the mean wind speed.

A histogram of the conical turbulence intensity is determined from the experimental spinner lidar data, cf. Figure 4-5. In 95% of all samples the conical turbulence intensity does not exceed the range 1% to 8%.

So it was found that conical lidar measurements deviate from wind fields characterised by five parameters with the deviation being approximately normally distributed, and that the conical turbulence intensity of the lidar measurements ranges from 1% to 8% at a near shore site during typical wind conditions. These results are used in the following simulation of different wind conditions to test the wind field parameter reconstructions.
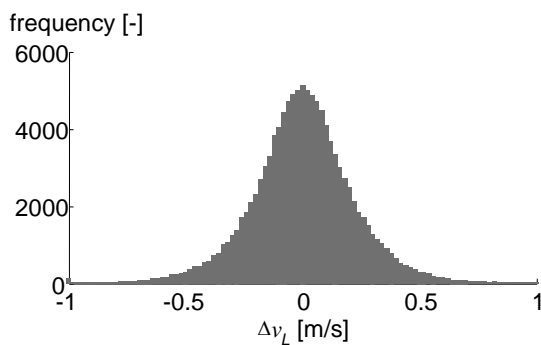

Figure 4-4: Velocity deviations: Experimentally determined distribution of deviations of measured velocities from fitted velocities in beam direction applying the five parameter model.
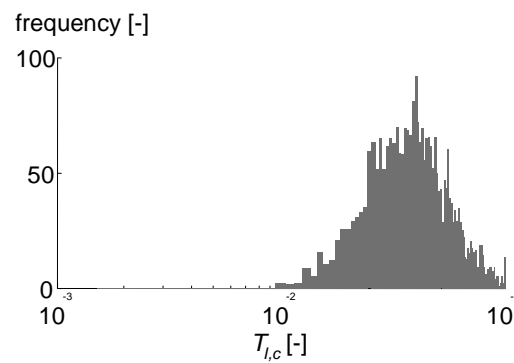

Figure 4-5: Turbulence intensity distribution: Experimentally determined distribution of the turbulence intensity of measurements in beam direction.

4.3.2 Monte Carlo Wind Field Simulation and Parameter Reconstruction

Simulated lidar measurements of synthetic wind fields evaluated using the five parameter model are assumed to be affected by statistical errors Δv_l in the following. The aim of the following computational experiment is to study the accuracy, and by that the practical applicability, of the presented different five parameter reconstruction methods. Whereas in the preceding sections the fundamental reconstructability has been deduced, the basic difference is that statistical fluctuations in the wind field are explicitly considered as they can represent spatial turbulence of real wind fields.

The parameter set $[u_0, s_h, s_v, \delta_h, \delta_v] = [10.0 \frac{\text{m}}{\text{s}}, 0.003 \text{ s}^{-1}, 0.02 \text{ s}^{-1}, 6.0°, 10.0°]$ was chosen to model the wind fields and to be reconstructed. The parameters are in a typical order during inflow conditions at rated wind speed.

Lidar measurements are simulated to be acquired via the geometrical projection on the 62 equi-azimuthal locations on a circle, with lidar beam width of $R = 96 \text{ m}$ and opening angle $\beta = 30°$. Inspired by the experimental lidar study above, the wind speed fluctuation in beam direction Δv_l is modelled $(0, \sigma)$-normally distributed with standard deviation $\sigma(\Delta v_l) = T_{I,c} \cdot \overline{v_l}$. It is thereby irrelevant if the fluctuations origin from spatial or temporal turbulence or if the lidar measurement principle contributes to the deviation. All sources are phenomenologically covered. As usual for Monte Carlo experiments a large number of random samples is produced, in this case 1000 series of 62 conical measurement errors each. For each experiment, both single distance and two distances five parameter reconstruction algorithms are employed to calculate parameter estimates. The two distance method additionally uses a second independent series of measurement errors. Root mean square errors of all experiments are then calculated for each parameter estimate and for both estimation methods, as a measure of the accuracy of the estimation.

All simulations and calculations are repeated with stepwise varied conical turbulence intensity in the range of 0.1% to 10%.

The results are shown in Figure 4-6. It can be seen that at vanishing turbulence both methods give perfect estimates of all five parameters, which signifies that any inflow behaving perfectly according to the five parameter model can be reconstructed even using measurements in only one distance. At increasing turbulence the single plane method produces large estimation errors. In the region of experimentally measured conical turbulence intensity of around 4% the direction error for instance exceeds 5° horizontal and 10° vertical.

The estimation method based on two measurement planes shows much better performance with very low estimation errors, for instance with direction errors below 1° over the whole region of occurring turbulence intensities. The remaining dependence on the conical turbulence intensity can be explained by the subset of

conical measurements taken from the whole wind field, and by the simplification of independent fluctuations in both of the two planes.
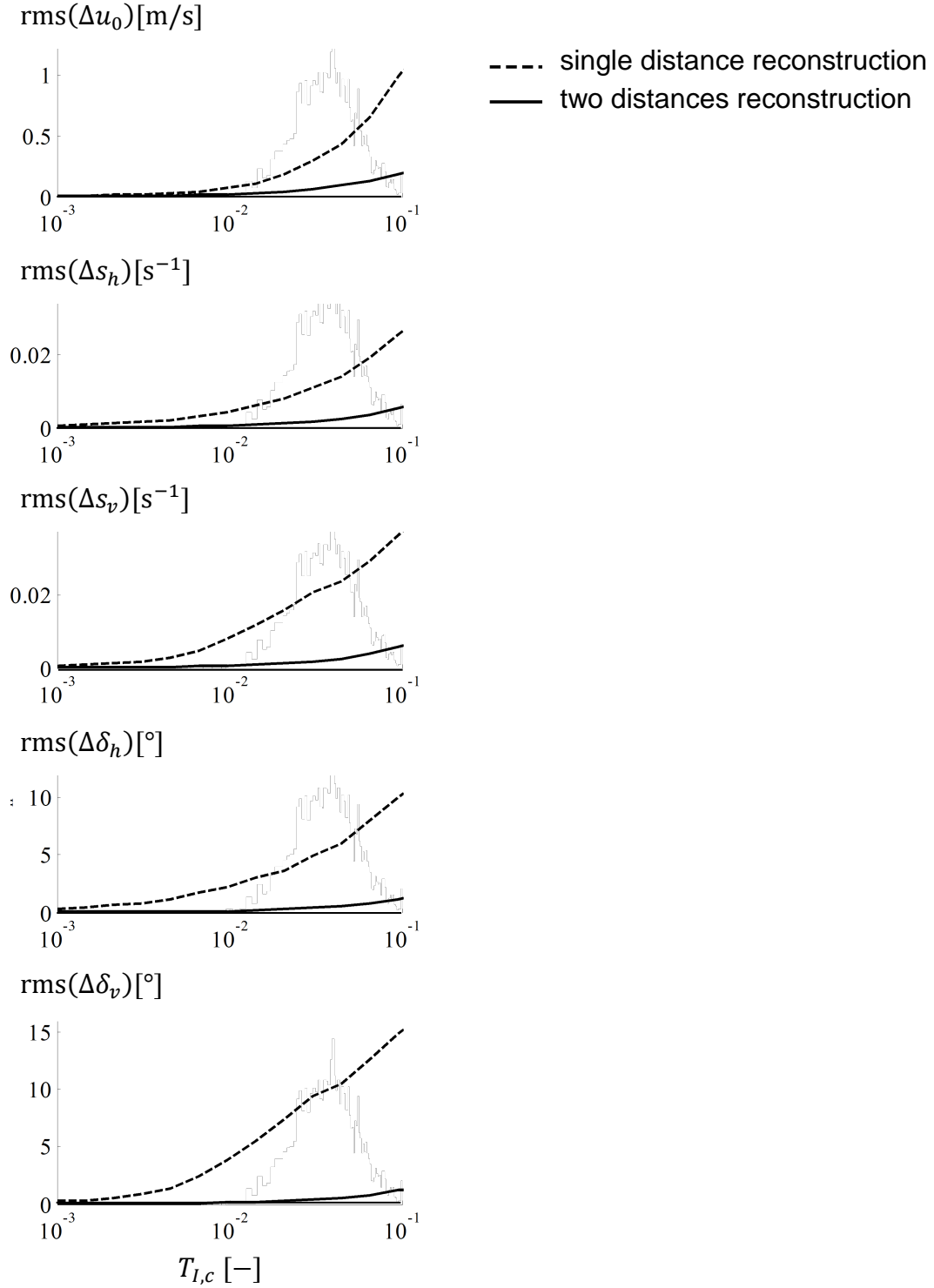

Figure 4-6: Root mean square errors of parameter estimations with respect to modelled conical turbulence intensities, calculated applying a Monte Carlo method, using one measurement distance (dashed), and two distances (solid).

4.4   Comparison of Geometric Reconstruction Methods

Different methods to reconstruct sets of wind field parameters have been presented.

A set comprising five wind field parameters is presented which describes the mean wind speed, wind shears and wind directions. All parameters can be relevant in wind energy applications. Different reconstruction methods for these five parameters have been developed, based on different lidar scan strategies.

In Subsection 4.2.2 it was found that using lidar measurements from at least two independent directions and on at least three focussed points within the wind field to be characterised, all five parameters can uniquely be reconstructed. As an approximation, the independent directions could be achieved with measurements in two distances and different angles, thereby assuming frozen turbulence between the distances. An approach to use more measurements than required is developped.

In Subsection 4.2.3 measurements in only one axial distance in front of a wind turbine rotor are considered. It is found that the determination of all five parameters is not unique and numerically unstable.

From the performed Monte-Carlo-Simulations of generic turbulent wind fields and simulated reconstruction it can be concluded that reconstruction uncertainties are much lower applying the two distances method. Assuming one measurement distance, all five parameters can be reconstructed with decreasing error for decreasing turbulence intensity, i.e. in very homogeneous cases with vanishing deviation from the wind field model. However, in all practical relevant cases with common turbulence intensity, as found by real measurements, the resulting reconstruction errors – and thereby the uncertainties – become unacceptably large, e.g. in the order of 5 to 10 degrees for wind direction errors.

In practice, measurements in two distances are therefore required to obtain all five parameters with low uncertainty in turbulent conditions.

In Table 4-1 the previous observations are summarized by assembling lidar scan strategies with their capabilities with respect to different reconstructable parameter sets. Most commercial lidars currently use two or more focus points in one plane, or measurements in multiple planes are not on a line in axial direction, resulting in the given restrictions. According to the presented results the extension of lidar designs to a second focus distance offers potential for improved wind field reconstruction.

Table 4-1: Lidar scan strategies and possible parameter reconstructions

lidar scan strategy		wind speed	vertical shear	vertical direction	horiz. shear	horiz. direction
1 distance	1 point	●	○			
	2 points	●	1 from 4			
	≥ 3 points	●	1 from 2		1 from 2	
2 distances	2 x 2 points	●	●	●	○	○
		●	○	○	●	●
		○	○	●	○	●
	2 x ≥ 3 points	●	●	●	●	●

5 Experimental Study of Inflow Wind Measurements

In the research and development process of industrial applications, and particularly for components, sensors and controls of wind turbines, the extensive use of experimental full scale studies is essential since the full complexity of the atmospheric wind flow and the dynamics of the entire system can hardly be reproduced only by numerical simulations yet.

Experimental studies in the field of turbine mounted scanning lidars are still rarely performed due to long preparatory periods, high expenditures and the need for collaboration between different stakeholders such as wind turbine manufacturers, operators, lidar manufacturers and scientists. So far, important inflow experiments have been performed by NREL, DTU and SWE as introduced in Section 1.2. A recent analysis by Schlipf et al. [77] at the NREL suggests that the so called rotor effective wind speed can be obtained using upwind pulsed scanning lidar data and rotor speed data to generated useful signals for feedforward pitch control. A study by Scholbrock et al. [78] indicates that wind direction signals obtained by a circular scanning continuous-wave lidar can provide useful yaw information under certain conditions.

Rarely, wind speed and wind direction information obtained by a turbine mounted lidar being affected by wakes of neighbouring turbines are studied. Also, the high frequent inflow scanning is new to turbine mounted lidar sensing. It needs deeper investigations on how to process the raw data and enables new insights into the inflowing wind.

The experimental study described here was carried out as part of "Integration of Wind LIDARs in Wind Turbines for Improved Productivity and Control" [79], a research project led by DTU Wind Energy and supported by The Danish National Advanced Technology Foundation. First results have been presented at EWEA Annual Event 2013 [65]. Recently, a further analysis was presented at [80].

This chapter focuses on the following selected topics:

1. The development of specific signal processing algorithms for raw signals of a new setup of a horizontally scanning lidar.

2. The statistical evaluation of wind speed and wind direction measurements applying the new turbine mounted scanning lidar setup and developed signal processing method, with special focus on the influence of the wakes of surrounding turbines in a wind farm.

3. The experimental study of wakes as detected by lidars in the inflow of a wind turbine.
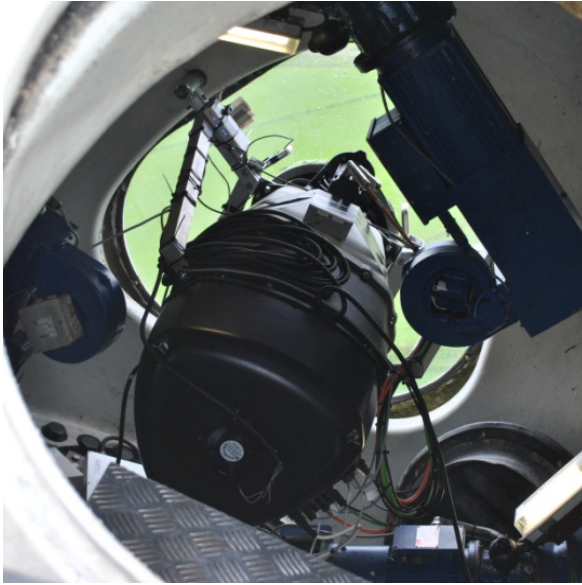
Figure 5-1: ZephIR lidar enhanced with a 2D scanning head (SpinnerLidar) designed by DTU Wind Energy, mounted in the rotating hub, scanning through a hole in the front window (in direction of view).

Figure 5-2: Downwind view on the experimental turbine with two ultrasonic acoustic resonance wind speed and direction sensors mounted on top of the cooler.

5.1   Experimental Setup

5.1.1   Double Prism Scanner

The regarded experimental setup comprises a two-dimensional laser scanner head developed by DTU Wind Energy. In the patent application [81], technical specifications are described in detail.

As a further development of the previous experiment of 2009 reported in [14] and [82] where a one-dimensional scanner head with one rotating prism was considered, the new two-dimensional laser scanner head comprises two coupled rotating prisms, also called Risley prism pair. A sectional view is shown in Figure 5-3. The special design enables the laser beam to be deflected to any point on a spherical segment upwind the sensor, the *field of regard*. Thus, the measurements are also referred to as *full two-dimensional*.
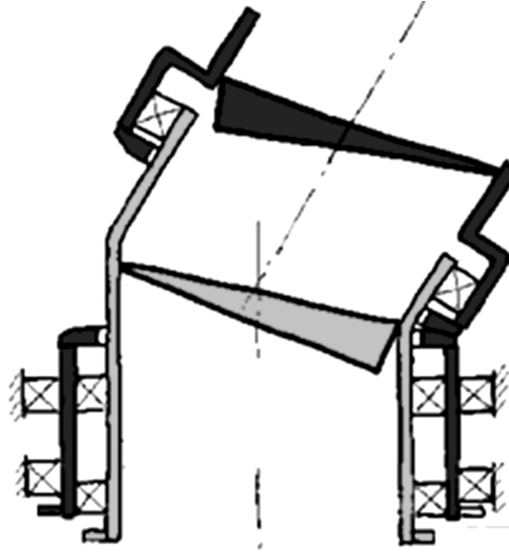
Figure 5-3: Cross-sectional view of the double prism scanner head developed at DTU with support from IPU, Lyngby, Denmark [81].
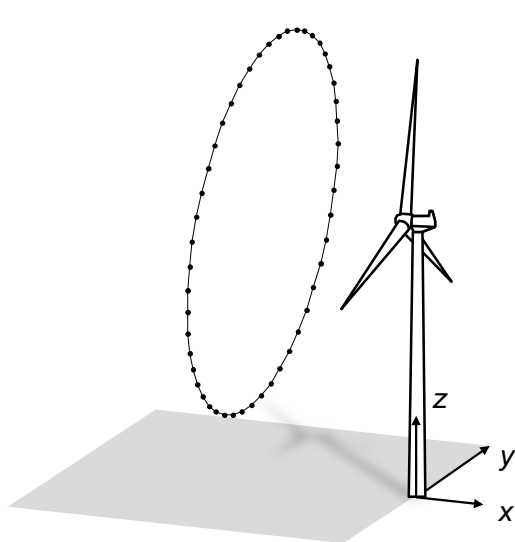
Figure 5-4: Conical scan pattern of the first spinner integration project 2009 [14], illustrated at standstill of the rotor.

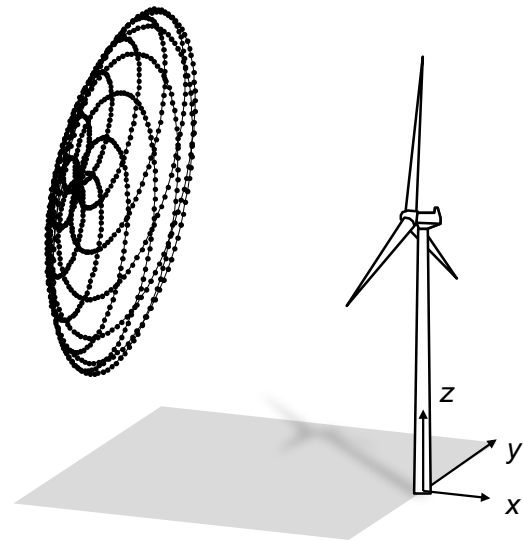*Figure 5-5: Full two-dimensional scan pattern of the second spinner integration project 2012 [65], illustrated at standstill of the rotor.*

The two rotating prisms with beam deviation angles each of 15° enable the deflection of infrared laser radiation between 0° and 30° in total, with respect to the optical axis of the device, and depending on their relative angle difference $\phi_1 - \phi_2$.

5.1.2 Instrumented Wind Turbine

The scanner is mounted on top of a continuous-wave lidar and is integrated into the centre line of the rotating hub of a NEG Micon NM80 test turbine at a height of 59 meters above ground. The specifications of the instrumented wind turbine are given in Table 5-1 and a picture of the lidar mounted inside the hub can be found in Figure 1-4.

Table 5-1: Specifications of the experimental wind turbine

Type	NM80
Manufacturer	NEG Micon (today Vestas)
Rated power	2.5 MW
Rated rotor speed	17.5 rpm
Number of blades	3
Power regulation	Pitch-regulated, rotor speed variable
Rotor diameter D	80 m
Rotor blade type	LM 38.8 P
Hub height	59 m
Pitch system	Electric DC pitch drives
Tilt angle	5°
Generator	Doubly-fed induction generator, water cooled

5.1.3 Wind Farm Layout and Evaluated Data

The instrumented wind turbine is located at Tjæreborg Enge, Denmark, within a wind farm of eight similar turbines and a met mast near the centre of the park. The find farm is located near the shore within open flat terrain vegetated with grass and with few isolated obstacles. The wind farm was investigated in research studies several times before, further descriptions can for example be found in [14].

The usable data of the experiment were recorded between September 2nd and 19th 2012. Lidar data, scanner data, turbine data and met mast data are available in this period. Lidar scanning frequencies of around 100, 200 and 500 Hz have been used during 8, 4 and 5 days successively. The presented data originates from the first period with scanner frequency of around 100 Hz between September 2nd, 07:00 and September 10th, 08:50 (1019 10-minute periods). A wind speed and direction overview of the period is given in Appendix A.3.

In the following subsections the wind farm layout is presented and the directional sectors of disturbed and undisturbed inflow are analysed.

5.1.4 Sectors of Undisturbed Met Mast Inflow

Figure 5-6 shows the sectors of disturbed and undisturbed inflow of the met mast. The directions to the centres of the neighbouring wind turbines are given and are denoted with square brackets for later reference. The spatial extent of the met mast is neglected and only the sensors at hub height are considered.
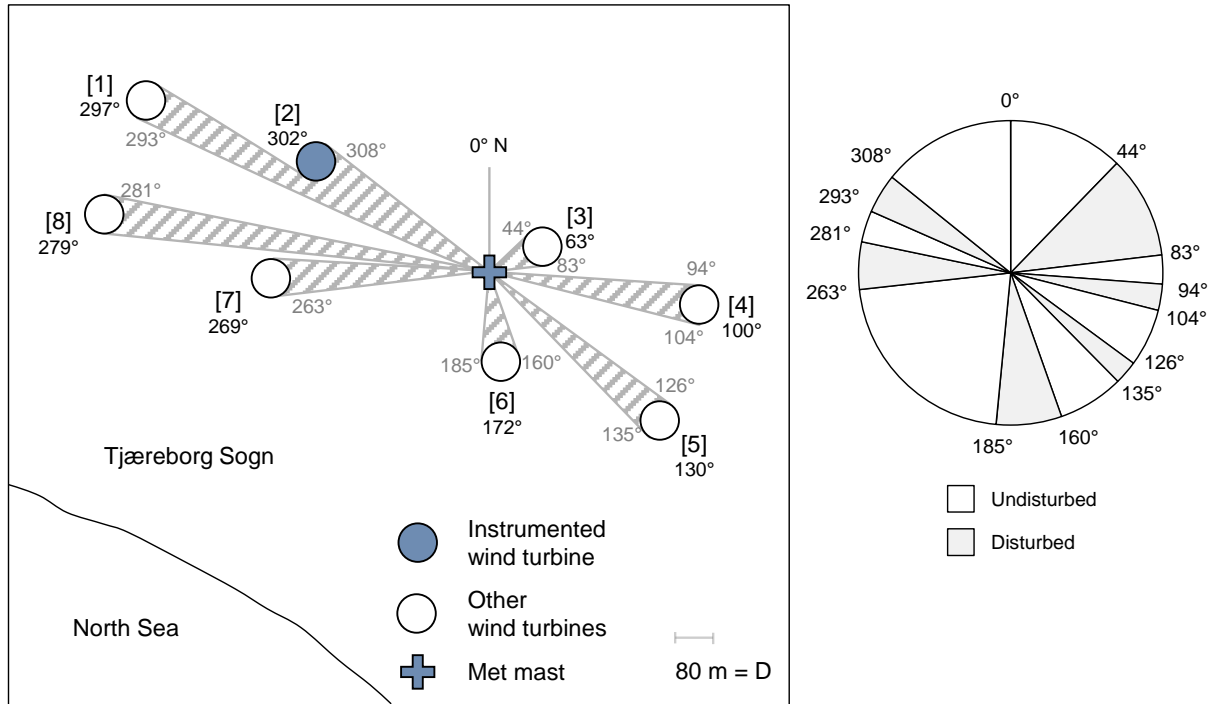

Figure 5-6: The test site with directions and denotation w.r.t. the met mast.Right: Inflow sectors.

5.1.5 Sectors of Undisturbed Turbine Inflow

Figure 5-7 shows the respective sectors of the instrumented turbine. Both the rotor diameters of the disturbing turbines and of the instrumented turbine no. (2) have to be taken into account to find the sectors. The directions to the centres of the neighbouring wind turbines are given and are denoted with round brackets for later reference.
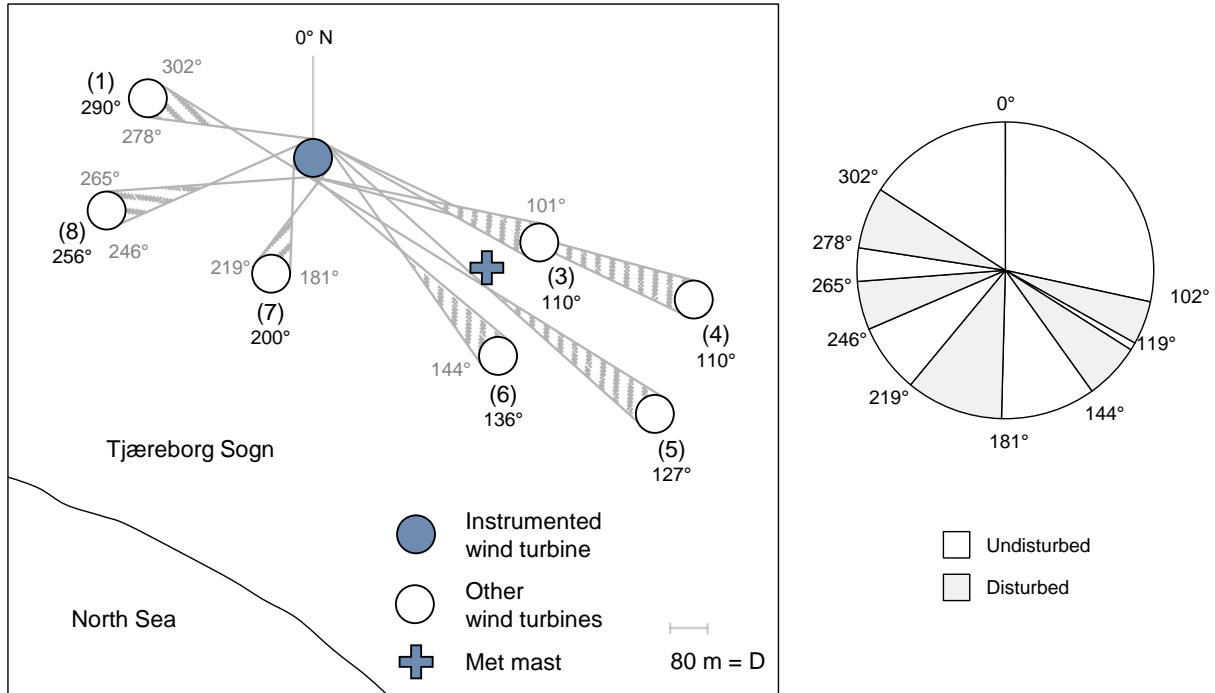
Figure 5-7: The test site with directions and denotation w.r.t. the instrumented wind turbine.Right: Inflow sectors.

5.1.6 Sectors of Undisturbed Lidar Inflow

If a wind speed measurement occupies a larger area than the rotor then the sectors of undisturbed inflow get smaller. In the case of the considered hub mounted upwind oriented lidar with a half cone opening angle of $\theta = 30°$ and focus length $l_{\mathrm{focus}} = 100$ m the situation of the sector limit relative to wind turbine (1) at distance $d_{12} = 379$ m is depicted in Figure 5-8.

Figure 5-8: Limit of undisturbed lidar sector

The relative limit angle δ_h^* can be calculated considering the dotted triangle in Figure 5-8 to

$$\sin(\delta_h^*) = \frac{R + l_{focus}\sin(\theta)}{d_{12}}.$$

(5.1)

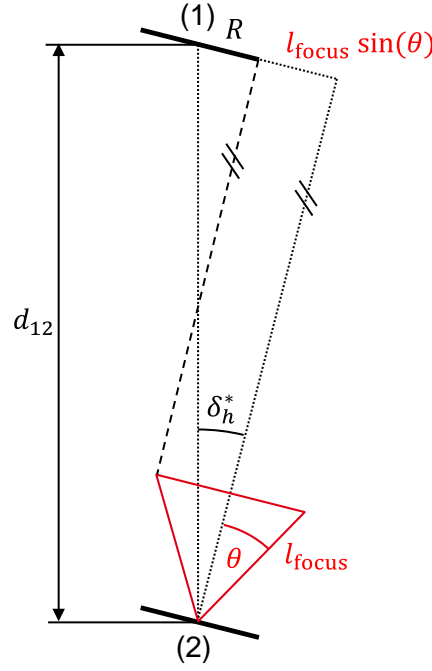Equation (5.1) can be solved for δ_h^* with positive R, l_{focus}, d_{12} and $0 < \theta < \frac{\pi}{2}$ and has one solution, if $R + l_{\text{focus}}\sin(\theta) < d_{12}$, which is fulfilled for all turbines within the considered wind farm $(40\text{ m} + 50\text{ m} < d_{n2}\ \forall n \in [1,8]\backslash 2)$.

If $R + l_{\text{focus}}\sin(\theta) > d_{12}$, i.e. for large scan areas or small distances between the turbines, the lidar always measures in the wake of turbine (1) in the range $-\frac{\pi}{2} < \theta < \frac{\pi}{2}$, or, depending on the focus distance, upwind of turbine (1).

Due to the symmetry, the sectors of disturbed lidar inflow are $\pm\delta_h^*$ relative to the straight orientation towards the neighbouring turbine. In Figure 5-9 all these lidar sectors are given.

Figure 5-9: Sectors of the lidar inflow
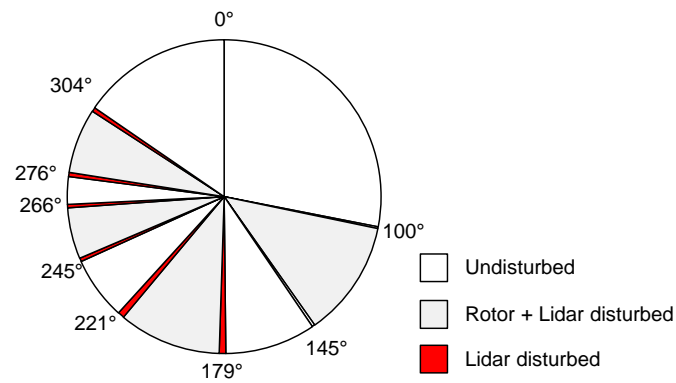
5.1.7 Sectors of Joint Met Mast and Lidar Inflow

The previous analyses are used to conclude the sectors of joint disturbed and undisturbed inflow. A sector is assumed joint undisturbed here if the inflow of both the mast and the lidar are undisturbed, e.g. the sector 221° to 245°. As a simplification, wake meandering is not regarded here.
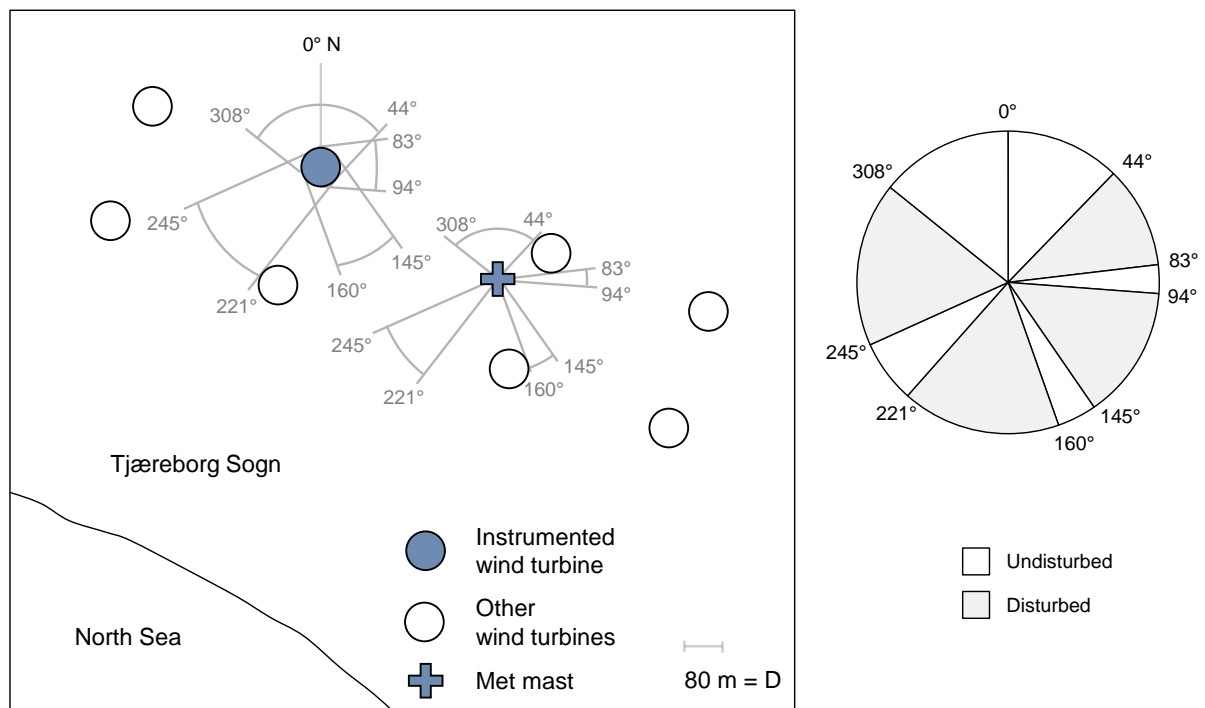

Figure 5-10: Joint mast and lidar sectors

5.2   Lidar Data Processing and Aggregation

The process of using two-dimensional scanning lidar data for analysis is organised in the following steps:

1. Determination of the prism angles ϕ_1, ϕ_2 using counter signals as exemplarily shown in Figure 5-12. Counter resets are detected a posteriori and the prism angles can be calculated from linear interpolation by assuming constant prism rotating speed, which is monitored by a motor controller.

2. Synchronization to the rotor angle signal ϕ_R and further signals of the lidar system. For this purpose, a signal of modulated frequency is generated and recorded at both scanner and lidar data acquisition systems, which comprise real time capable controllers with respective inputs and outputs. By comparing the synchronisation signal, offsets and signal gaps can be eliminated successfully.

3. Calculation of the focus position in ground coordinates for given rotor angle ϕ_R and prism angles ϕ_1, ϕ_2 by applying the calculations steps given in Subsection 5.2.1.

4. Recording of lidar backscatter signals and calculation of averaged power spectra of the returned Doppler shifted laser radiation by applying a real time embedded fast Fourier transform (FFT) algorithm.

5. Preprocessing of stored averaged backscatter spectra to eliminate noise and other unwanted effects and transformation to signals of wind speeds in beam direction as expounded in Subsection 5.2.2.

6. Merging of the signals of the scanner and lidar data processing path to obtain a vector field of wind speeds in beam direction at focus positions, each vector tagged with a time stamp t_i.

7. Aggregation of wind speed vector data within a time interval $\Delta t = [t_{i-m}, t_{i+m}]$ to wind field parameters. The locations of focus positions cover a representative part of the wind field area, to calculate wind field characteristics applying calculation methods of Chapter 4.

```
                            ┌────────────────────┐
                            │   time step $t_i$  │
                            └────────────────────┘
```

$$\text{time step } t_i$$

1. prism angles $\phi_1(t_i),\ \phi_2(t_i)$

2. sync.

rotor angle $\phi_R(t_i)$

4. averaged backscatter intensity spectrum $\bar{I}_B(t_i, f_B)$

3. focus position $[x_G, y_G, z_G](\phi_1, \phi_2, \phi_R)$

5. wind speed in beam direction $v_L(t_i)$

6. vector field of measurements $v_L(t_i, [x_G, y_G, z_G])$

7. aggregated wind field characteristics $p(t_i) = f\big(v_L(t_j)\big) \quad j \in [i - m, i + m]$
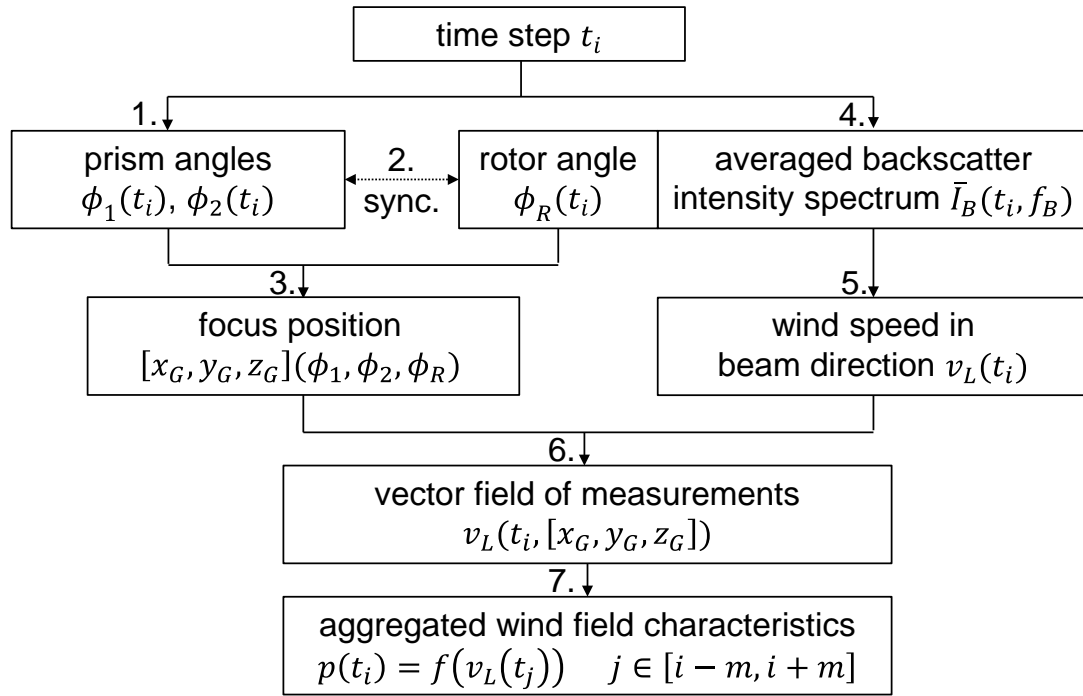
Figure 5-11: Signal processing steps of scanner head data (left path), lidar data (right path) and aggregated wind field data (steps 6 and 7).
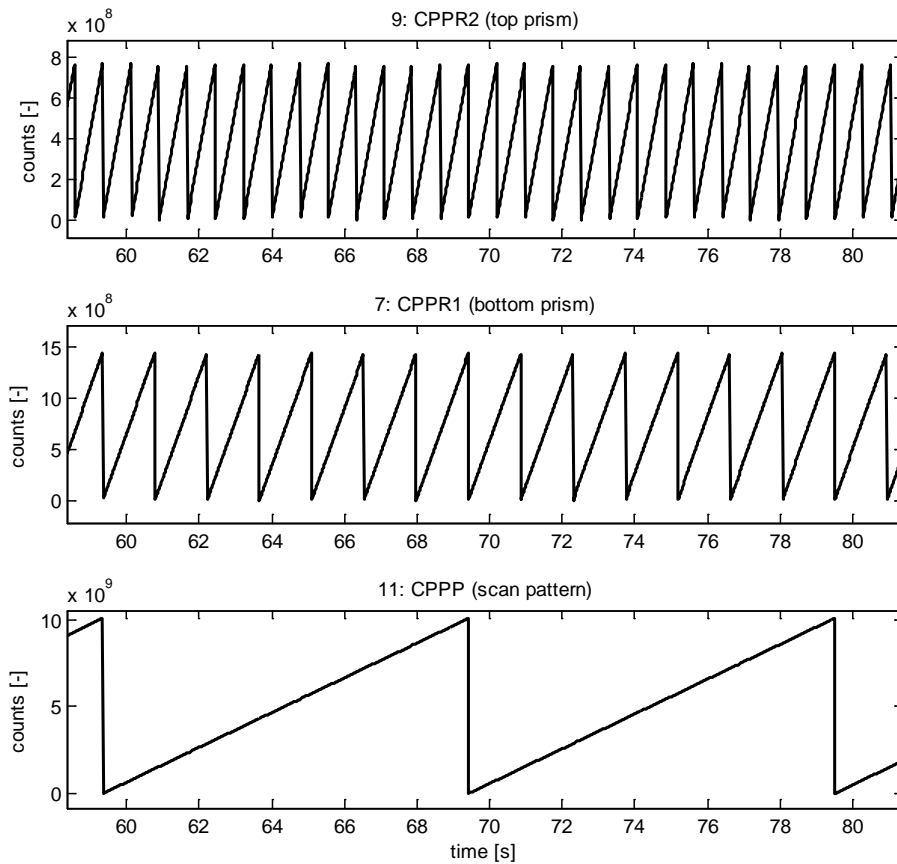

Figure 5-12: Counters for the top and bottom prism rotation and the scan pattern progress. One pattern is finished within 10.075 seconds and the scan pattern counter CPPP is reset when 7 bottom and 13 top prism rotations have been finished.

5.2.1   Geometrical Determination of Focal Positions

The rotating beam intersected with the y-z-plane at distance $\tilde{x} = l_{\text{focus}} \cos(\theta)$ gives the approximated coordinates of the scan pattern by

$$\begin{bmatrix} \tilde{y} \\ \tilde{z} \end{bmatrix} (\phi_1, \phi_2) = \frac{R_{yz}}{2} \begin{bmatrix} -\sin(\phi_1) - \sin(\phi_2) \\ \cos(\phi_1) + \cos(\phi_2) \end{bmatrix} \tag{5.2}$$

with $R_{yz} = l_{\text{focus}} \sin(\theta)$ the maximum scan radius in the y-z-plane. The parametric Equation (5.2) is a special form of an epitrochoid with equal sine and cosine contributions. The exact focus point coordinates are slightly radially shifted by

$$\Delta r = (l_{\text{focus}} - l_0) \frac{r}{l_0 \sqrt{\left(\frac{r}{l_0}\right)^2 + 1}} \tag{5.3}$$

with $r = \sqrt{\tilde{y}^2 + \tilde{z}^2}$ and $l_0 = \sqrt{\tilde{x}^2 + \tilde{y}^2 + \tilde{z}^2}$, to become

$$\begin{bmatrix} x' \\ y' \\ z' \end{bmatrix} (\phi_1, \phi_2) = \begin{bmatrix} -\sqrt{l_{\text{focus}}^2 - (r + \Delta r)^2} \\ \tilde{y} \left(1 + \dfrac{\Delta r}{r}\right) \\ \tilde{z} \left(1 + \dfrac{\Delta r}{r}\right) \end{bmatrix}, \tag{5.4}$$

x', y', z' indicating coordinates in the rotating lidar frame of reference.

A fixed coupling ratio of 13 top prism rotations per 7 bottom prism rotations was chosen to produce a spatially well distributed scan pattern, cf. Figure 5-14.
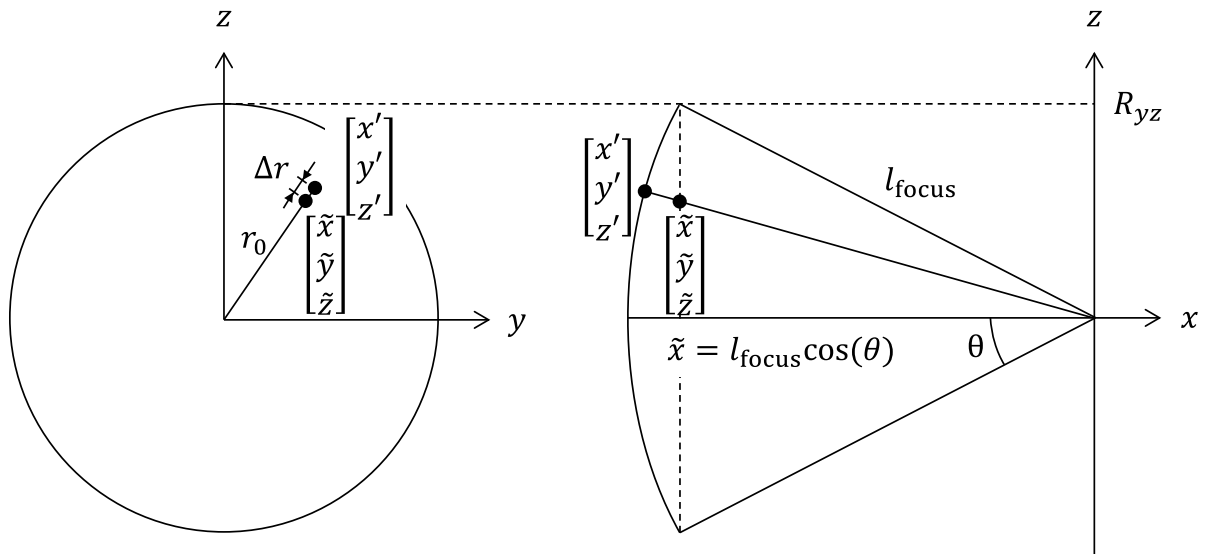

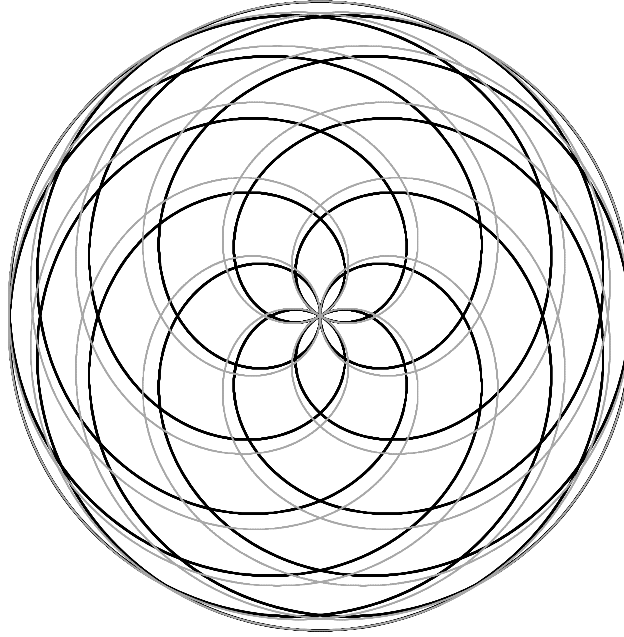*Figure 5-13: Coordinates of scanned points in lidar reference system.*

Figure 5-14: Epitrochoidal trajectory of the double prism scan pattern.
Black: Intersection of the beams and the y-z-plane at $[\tilde{x}, \tilde{y}, \tilde{z}]$
Grey: Exact focus points at $[x', y', z']$.

In a fixed rotor x-y-z-frame of reference the pattern can be obtained by a rotation about the x-axis about the rotor angle of revolution ϕ_R

$$
\begin{bmatrix} x \\ y \\ z \end{bmatrix} = \begin{bmatrix} 1 & 0 & 0 \\ 0 & \cos(\phi_R) & -\sin(\phi_R) \\ 0 & \sin(\phi_R) & \cos(\phi_R) \end{bmatrix} \cdot \begin{bmatrix} x' \\ y' \\ z' \end{bmatrix}
\tag{5.5}
$$

Since the rotation directions of the rotor and the prisms agree, a full scan pattern is completed in less than the duration time for the pattern during stand still.

For a fixed rotor position, the scanned trajectory is shown in Figure A.1-1, whereas for a given constant speed of typically one revolution per 3.8 seconds the resulting scanned trajectory is given in Figure A.1-2 in the Appendix.

Finally, in a ground based yawing x_G-y_G-z_G-frame of reference the focus points are obtained by a rotation about the y-axis about the tilt angle τ:

$$
\begin{bmatrix} x_G \\ y_G \\ z_G \end{bmatrix} = \begin{bmatrix} \cos(\tau) & 0 & \sin(\tau) \\ 0 & 1 & 0 \\ -\sin(\tau) & 0 & \cos(\tau) \end{bmatrix} \cdot \begin{bmatrix} x \\ y \\ z \end{bmatrix}
\tag{5.6}
$$

Equations (5.2) to (5.6) can be used to get all focus positions for known prism angles ϕ_1, ϕ_2, rotor azimuth angle ϕ_R, focus distance l_{focus} and nacelle tilt angle τ.

5.2.2 Backscatter Interpretation Algorithm

Wind lidar systems like the one used for the present experiments continuously record the infrared backscatter signal and periodically calculate backscatter intensity spectra applying real time fast Fourier transform methods, cf. Chapter 2.

The following four established steps of lidar spectrum processing are performed, compare [63]:

1. Raw spectra
   Post processing starts with the raw averaged spectrum. Here, between 400 and 4000 spectra have been averaged, each spectrum being based on 5 µs of backscatter signal, resulting in data rates between 50 and 500 wind speed measurements per second. It has to be considered that a lower number of averaged spectra, necessary for high sampling rates, results in a decreased sensitivity proportional to the ratio of the square root of this number.
   The spectrum is then divided into 256 bins, each representing approximately 0.15 meters per second of wind speed difference in the radial beam direction. Only spectra with intensity values smaller than a certain device specific limit are considered. Spectra with higher intensities originate from strong reflections of the laser beam at the window or other hard targets such as other turbines, birds or the ground. Here, a limit of the dimensionless value of $3 \cdot 10^7$ was chosen, excluding around 4% of the recorded spectra.

2. Whitening
   Secondly, the averaged intensity values of the spectrum are divided by a relative intensity noise (RIN) spectrum, which can be measured in calibration tests or obtained by using appropriate experimental online data as shown in Appendix A.2. Frequency-dependent noise intensity variations are thereby dissolved, the spectrum is whitened.

3. Thresholding
   Next, a threshold level is determined, often using the mean spectrum values at high frequencies plus an offset depending on the standard deviation of those intensities.

4. Removing of noise at low frequencies
   A common method implemented to remove cw-lidar inherent backscatter noise at low frequencies is to ignore intensity values at low frequency bins [83]. It has to be considered that corresponding low wind speeds are lost for further usage. Here, a limit of 5 bins corresponding to a radial velocity of 0.75 m/s was chosen.

As a special effect of the new two-dimensional scanning lidar signals, high backscatter intensity at both low and high frequency bins have been observed, at least partly caused by reflections of the laser beam at the scanner window or other targets like the ground when pointing downwards.

5. Removing of side peaks

In cases where step 4 did not eliminate these lower intense reflections, a filtering approach has been developed to exclude side peaks, i.e. nonzero frequency intensities not adjacent to the main peak where the likely maximum or centroid is anticipated. The approach is realised by an a posteriori algorithm: From the calculated peaks in the past, the likely intensity peak for the next spectrum number is linearly extrapolated. Then, an intensity range is determined, starting at the extrapolated intensity, covering all adjacent nonzero intensities and additionally elements separated by a small number of allowed zero intensities. Finally, other unconnected nonzero intensities are not considered in the peak calculation.

An example can be seen in Figure 5-15, indicating nonzero unconnected elements red marked. Obviously, unwanted outliers are eliminated around spectral numbers 98 (low bins) and 170 (low and high bins), but at the same time likely parts of the true wind induced backscatter bins are erroneously excluded, for example at numbers 120 to 135. As a solution, a further improvement of the algorithm does not ignore all unconnected peaks, but still preserves peaks that are separated by a certain limit of frequency steps, $\Delta f_{\mathrm{bin,max}}$. In Figure 5-15, bottom, a limit of seven frequency bins have been allowed to occur between the main peak and side peaks, preventing the exclusion of likely areas of the main peak as in the Figure 5-15, top.
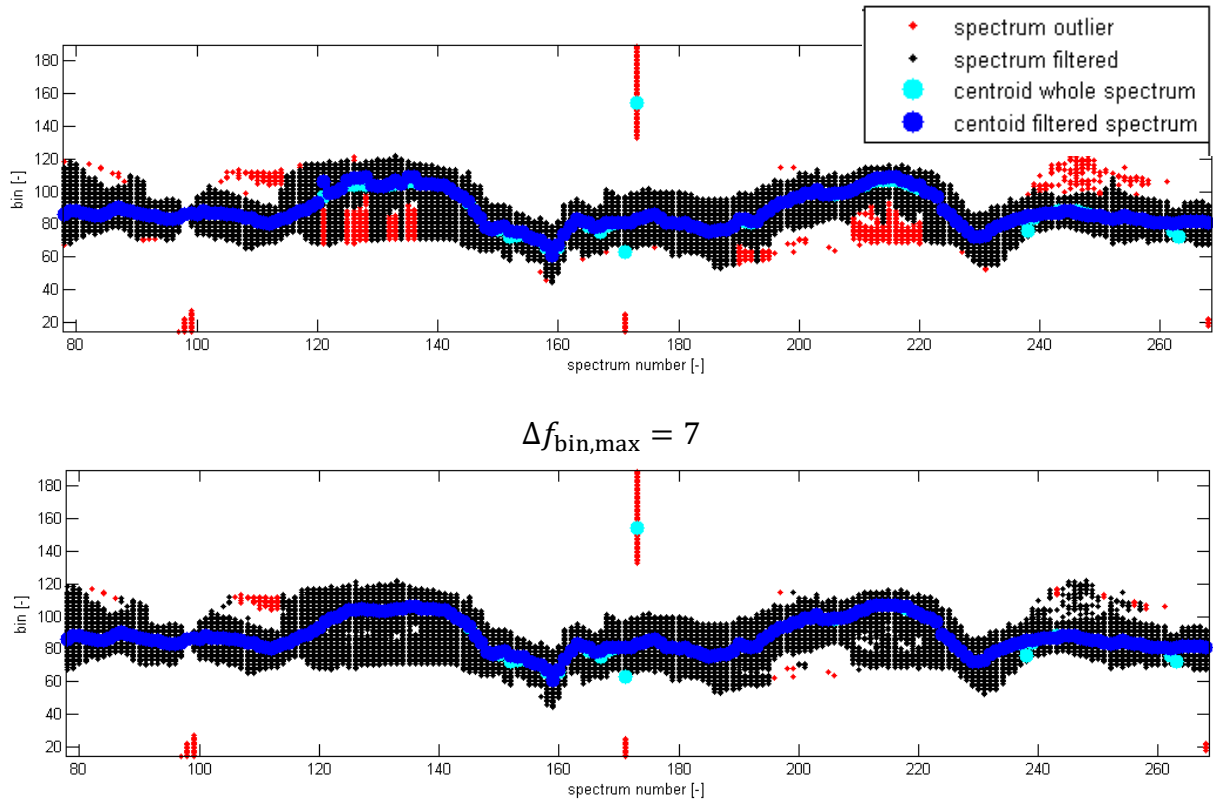
$$\Delta f_{\text{bin,max}} = 7$$
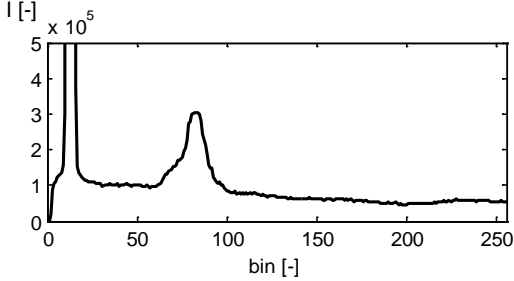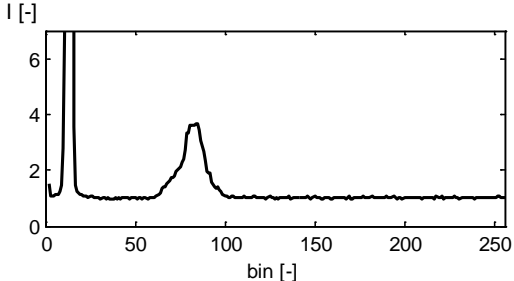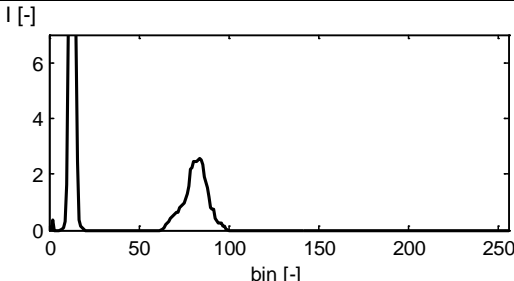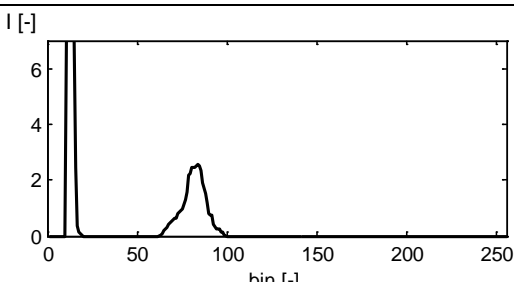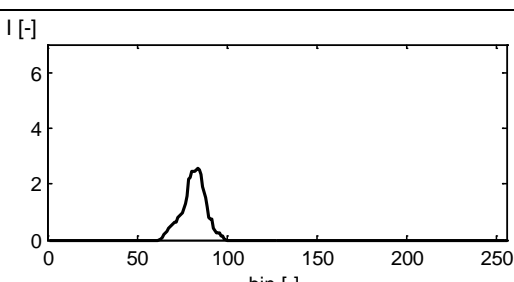
Figure 5-15: Backscatter spectrum processing step 5: Outliers (red) are identified and neglected. Allowing seven connected zeros (bottom) in the neighbourhood of the likely spectrum peak prevents from erroneously defining too many outliers.

Finally, the cleaned spectrum is used to evaluate a single average wind speed value in beam direction during the time interval of spectra acquisition. For that purpose, different methods are possible, while the calculation of the centroid of the averaged spectrum is often preferred due to its robustness against random spectrum peaks. The centroid frequency is then converted to its corresponding line-of-sight wind speed value.

Table 5-2: Steps of lidar backscatter spectrum processing

Step	Example Spectrum	Changed spectra
1. Raw valid averaged spectrum, criterion: all intensities $< 3 \cdot 10^7$		4%
2. Whitened spectrum, divided by a RIN spectrum		100%
3. Thresholded spectrum: The mean white noise level + 5 times the standard deviation between bins 200 and 250 is subtracted		100%
4. Cut spectrum: Bins 1-5 are set to zero		59%
5. Cleaned spectrum using cleaning algorithm to eliminate "unconnected" peaks		20%

5.2.3 Signal Availability

Line-of-sight lidar data of the above introduced experimental setup was calculated during the evaluated period of 170 hours with data of a sampling rate of approximately 100 Hz. If the abovementioned steps of backscatter spectrum processing did not result in valid radial wind speed, the single measurement was marked invalid.

In Figure 5-16 the amount of identified invalid data at 100 Hertz is plotted against the wind speed. When lidar signals are considered invalid, the radial wind speed is linearly interpolated. Invalid data can be found at all wind speed ranges and is similarly distributed as the valid data. At the minimum wind speed (0.75 m/s in this analysis) the amount of valid and invalid data is significantly higher due to cw-lidar inherent low speed measurement limitations. By a more restrictive cutting of the low end of the spectra, e.g. up to a radial wind speed of 1 m/s the quality of the data and the availability could be slightly improved.
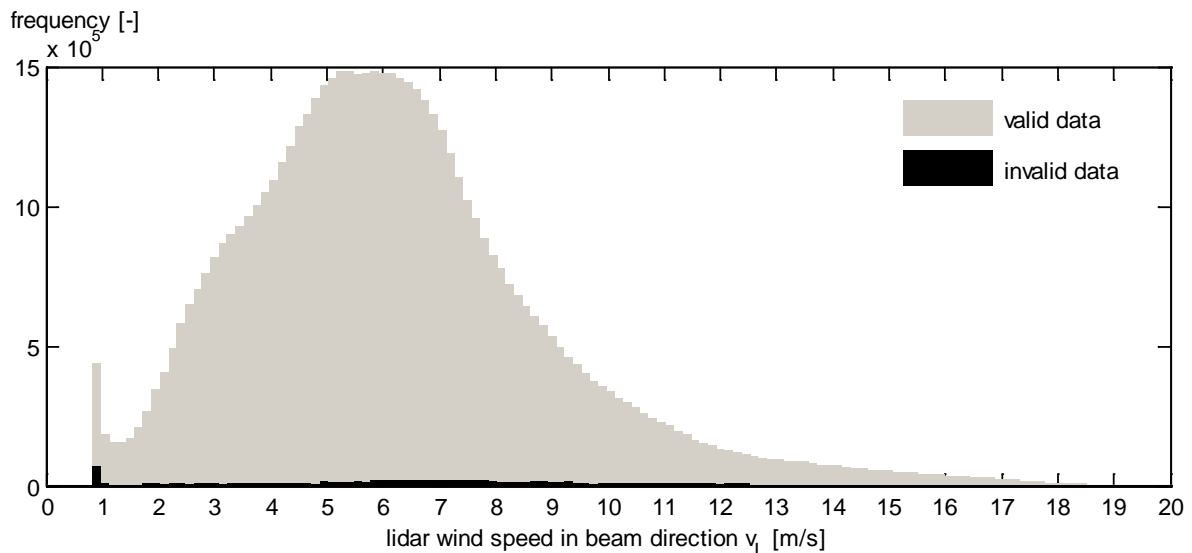
Figure 5-16: Frequency of valid and invalid experimental lidar data plotted against wind speed v_L in beam direction.

Data loss is expected to decrease when aggregating multiple line-of-sight values within short periods of time. Therefore the same experimental data is transformed to the lower data rates 50, 10 and 1 Hz. Values are considered valid if at least one value to be aggregated is valid, i.e. if one valid wind speed is found using the backscatter interpretation steps described in Table 5-2 in Subsection 5.2.2. In Table 5-3 the remaining data loss rates are listed, ranging down below 0.1% for 1 Hz aggregated data.

Table 5-3: Relative data loss due to weak SNR during the test period

data rate	data loss
100 Hz	1.9 %
50 Hz	1.3 %
10 Hz	0.5 %
1 Hz	< 0.1 %

5.3   Lidar Measurement Results

After the calculation of line-of-sight velocities from the raw backscatter spectra described in Section 5.2, the experimental lidar data can be analysed according to the objectives introduced at the beginning of this chapter, namely the accuracy of the determination of wind speed and direction signals and the dynamics of wind field characteristics.

5.3.1   Wind Speed Accuracy in a Wind Farm

As a first step, and often applied in lidar data studies, it is proposed to perform a validation test by statistically comparing averaged wind speed signals of the lidar system to those of other sensors.

Hub Lidar versus Nacelle Sensor

Here, averaged data of the hub mounted two-dimensional scanning lidar ("turbine lidar") is compared to averaged data of a nacelle mounted ultrasonic acoustic resonance wind speed and direction sensor system ("nacelle sensor"). Lidar data is processed following the steps described in Section 5.2 and applying the nonlinear three parameter model of Section 4.1.1 comprising vertical shear and horizontal direction parameters, followed by the corresponding reconstruction algorithm. The resulting wind speed parameter in yawing ground coordinates is averaged for each ten minute interval.
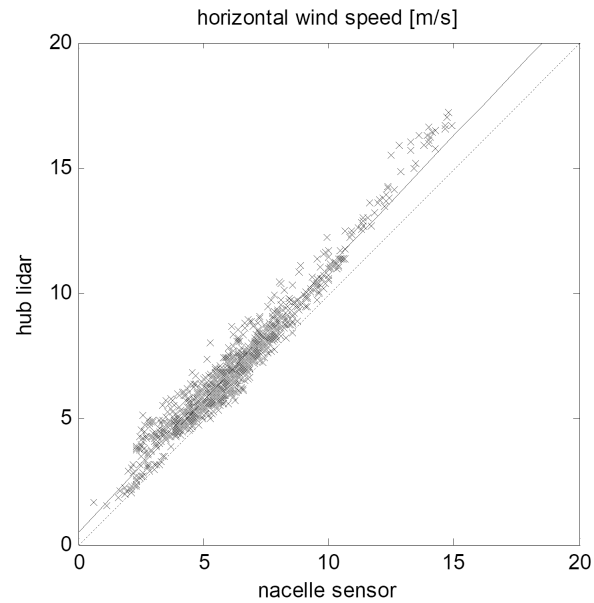
Figure 5-17: 10-minute averages of the horizontal wind speed
obtained by the lidar relative to the standard nacelle measurement.
Dashed: $y = x$; Solid: $y = 1.053\,x + 0.500\ m/s;\ r^2 = 0.952$

As expected, the averaged horizontal wind speed measured by the lidar on the sphere segment at 86.6 to 100 meters upwind is higher than the nacelle wind speed measurement around 10 meters behind the rotor plane, where the energy extraction by the rotor has produced a significant speed deficit. A linear regression analysis reveals 0.5 meters per second difference on average over all wind speeds and all direction sectors, and an increasing tendency for higher wind speeds. Despite the different physical measurement principles, measurement volumes and locations, the correlation of the averaged wind speed signals is high, with a coefficient of determination exceeding 0.95.

Hub Lidar and Nacelle Sensor versus Met Mast Ultrasonic

Ten minute intervals of 20 Hz data of the ultrasonic anemometer mounted at hub height on the adjacent met mast are averaged in intervals of ten minutes over the same experimental period and compared against the nacelle and lidar based data. Wind speed differences of the averaged signals are calculated accordingly and related to the mean wind direction defined by the met mast measurement.

The differences in wind speed, as can be seen from Figure 5-18, range from -5 to 5 meters per second and depend on wind direction, in a similar way for both the nacelle anemometer and the hub lidar. The nacelle anemometer has a slight systematic negative offset of around 0.5 m/s in the joint undisturbed sector between 221° and 245°. A calibration of the nacelle anemometer to compensate this systematic difference could be a possible application of the regarded lidar for this turbine.

The other systematic differences that occur at both analyses can be explained by wake effects of surrounding wind turbines, i.e. the speed deficit caused by the energy extraction of other rotors in the wind farm as mapped in Figure 5-6 and Figure 5-7.

The cases of positive difference, i.e. when nacelle and hub lidar instruments measure higher wind speeds, occur generally around wind directions 175°, 266°, 279° and 303° , where wakes of turbines [6], [7], [8] and [2] towards the met mast can be expected.

During wind directions with negative speed difference at 200°, 256° and 290°, wakes of turbines (7), (8) and (1) obviously reduce the speed of wind reaching the instrumented turbine.
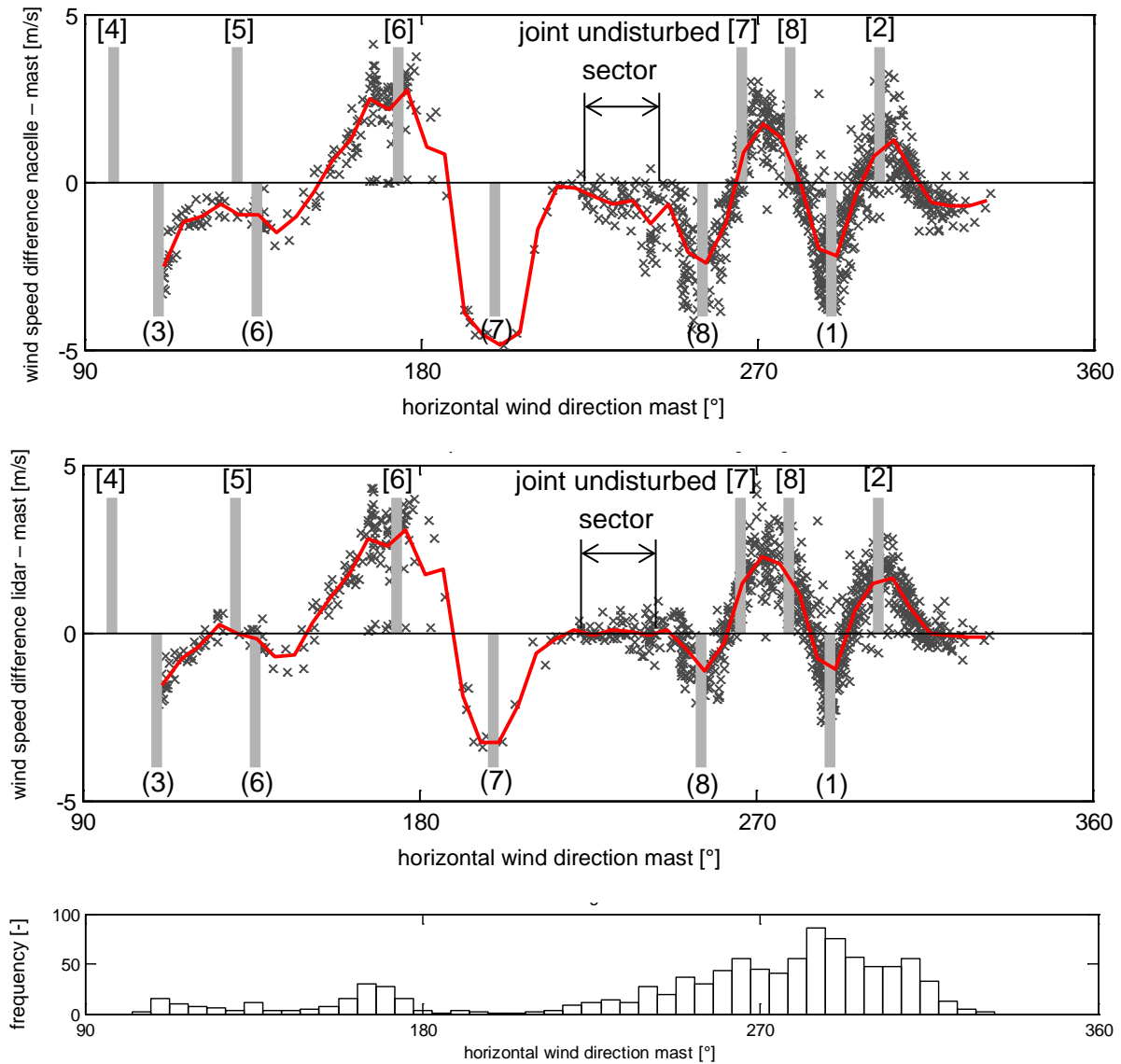
Figure 5-18: Deviations of nacelle (top) and lidar (middle) 10-minute averages of wind speed measurements from met mast reference, relative to the wind direction measured by the met mast.
Solid red line: Mean difference per direction bin of five degrees.
Vertical lines indicate directions of neighbouring turbines relative to the considered NM80 (below zero) and to the met mast (above zero), according to Figure 5-6 and Figure 5-7.
Wakes directed to the turbine produce a positive difference, wakes to the met mast a negative difference.
Bottom: Frequency distribution of wind directions measured by the mast sensor.

5.3.2   Wind Direction Accuracy in a Wind Farm

Hub Lidar versus Nacelle Sensor

The lidar experiment described above also allows the calculation of 10-minute averages of the wind direction, in the same way as the wind speed in the previous subsection. These direction data and the ten minute averages of the nacelle sensor

direction data are corrected with the yaw data of the wind turbine, to get absolute direction values, and are compared in the following.

In Figure 5-19 the relation of lidar and nacelle direction is shown. In the joint undisturbed sector between 221° and 245° (see details in Figure 5-19, right) the signals show linear dependency with an offset of around 4°. The offset could be caused by errors in the alignment or calibration of one of the sensors lidar, nacelle direction or yaw orientation. Possibly, the wake behind the rotor of the instrumented turbine induces wind direction changes on the nacelle sensor, which are not or not perfectly corrected.

In the disturbed direction sectors the differences in the averaged direction signals of the considered lidar and the nacelle sensor are large and are analysed in more detail in the following subsection.
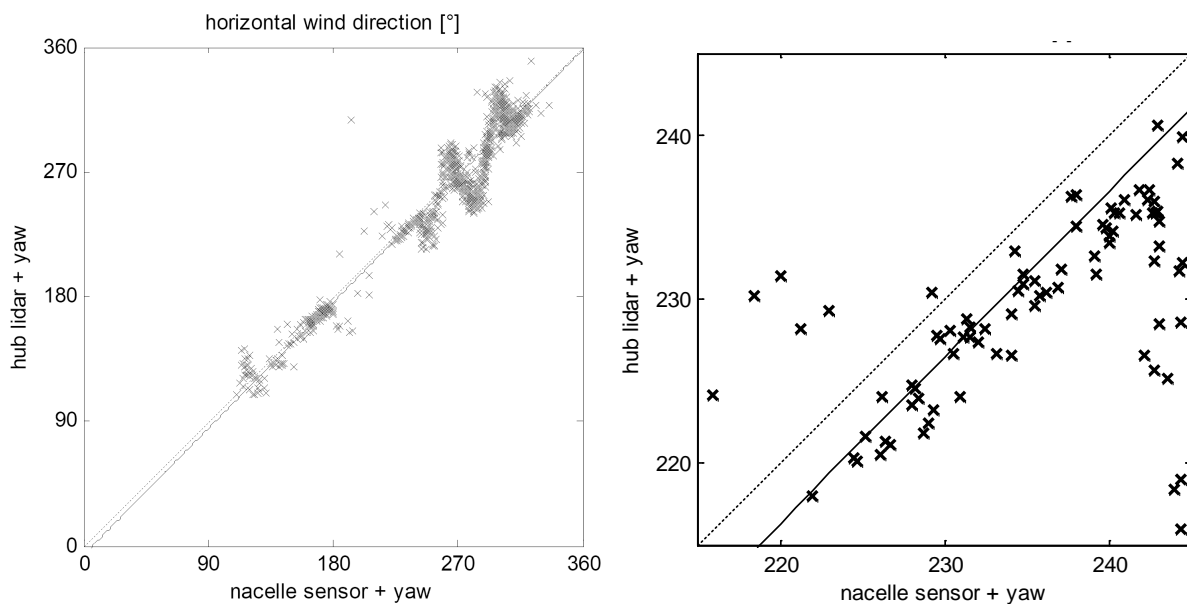
Figure 5-19: 10-minute averaged horizontal wind direction obtained by the lidar relative to the standard nacelle measurement, both corrected by the yaw direction.
Dashed: $y = x$; Solid: $y = 1.013\,x - 6.459\,°$; $r^2 = 0.927$
Left: Overall data; Right: Zoom on joint undisturbed sector 221°-245°

Hub Lidar and Nacelle Sensor versus Met Mast Ultrasonic

Hub lidar, nacelle sensor and met mast signals are processed as in the preceding subsection, and the yaw direction is added to both the lidar and the nacelle horizontal wind direction signals.

Figure 5-20 and Figure 5-21 present a comparison of the directions in x-y-plot form: IN average over all directions, the signals show an offset of around51° (nacelle sensor) and 47° (experimental lidar) due to a missing calibration of the met mast direction signal. In the following, the met mast signal is corrected by 51° to give met

mast direction data in a ground system of reference. At this point, it cannot finally be decided whether the conventional nacelle anemometer or the lidar wind direction calculation method produce an absolute offset in the experiment, which would be a matter of sensor direction calibration.

While the correlation of the nacelle based direction and the mast as reference is very high, with a coefficient of determination of $r^2 = 0.996$ and a deviation in the slope of 1.8%, the lidar based horizontal wind direction measurement is significantly affected by errors. These errors seem to systematically be caused by the absolute wind direction.
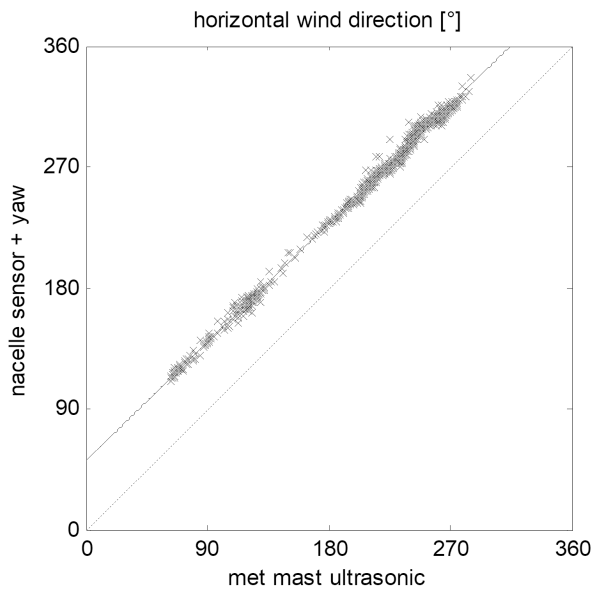
Figure 5-20: Nacelle wind direction relative to met mast measured direction at hub height.
Dashed: $y = x$
Solid: $y = 0.982\,x + 51.0\,°$; $r^2 = 0.996$
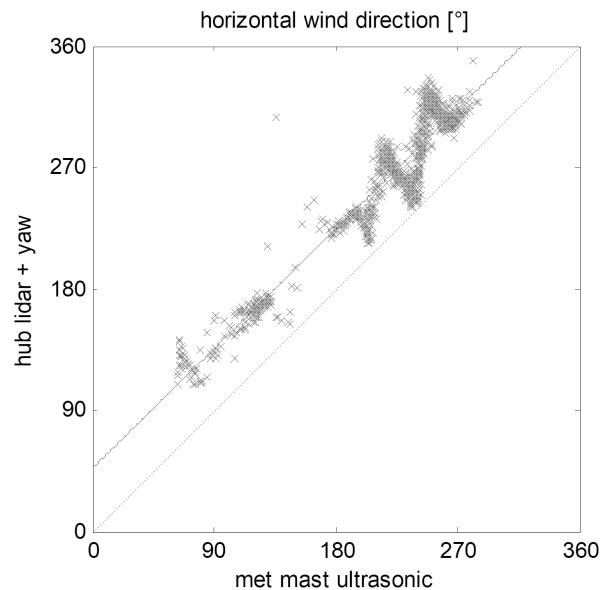
Figure 5-21: Lidar wind direction relative to met mast measured direction at hub height.
Dashed: $y = x$
Solid: $y = 0.987\,x + 46.7\,°$; $r^2 = 0.910$

In Figure 5-22, the difference in the wind direction between hub lidar and met mast as well as between nacelle sensor and met mast are analysed regarding their dependency on the wind direction.

In the undisturbed sector between 221° and 245°, the nacelle sensor offset is around zero degrees in average (as expected due to the correction), and the lidar direction difference to the mast is around -4°.The pattern of the differences is different than that of the wind speed differences observed in Section 5.3.1. There are significant deviations in the direction signal based on the lidar data, and relatively minor differences in the nacelle signal. For example at around 282°, the lidar direction is 25° lower, in average, with several ten minute intervals exceeding -40° difference, while the nacelle's average deviation is -2.3° only.
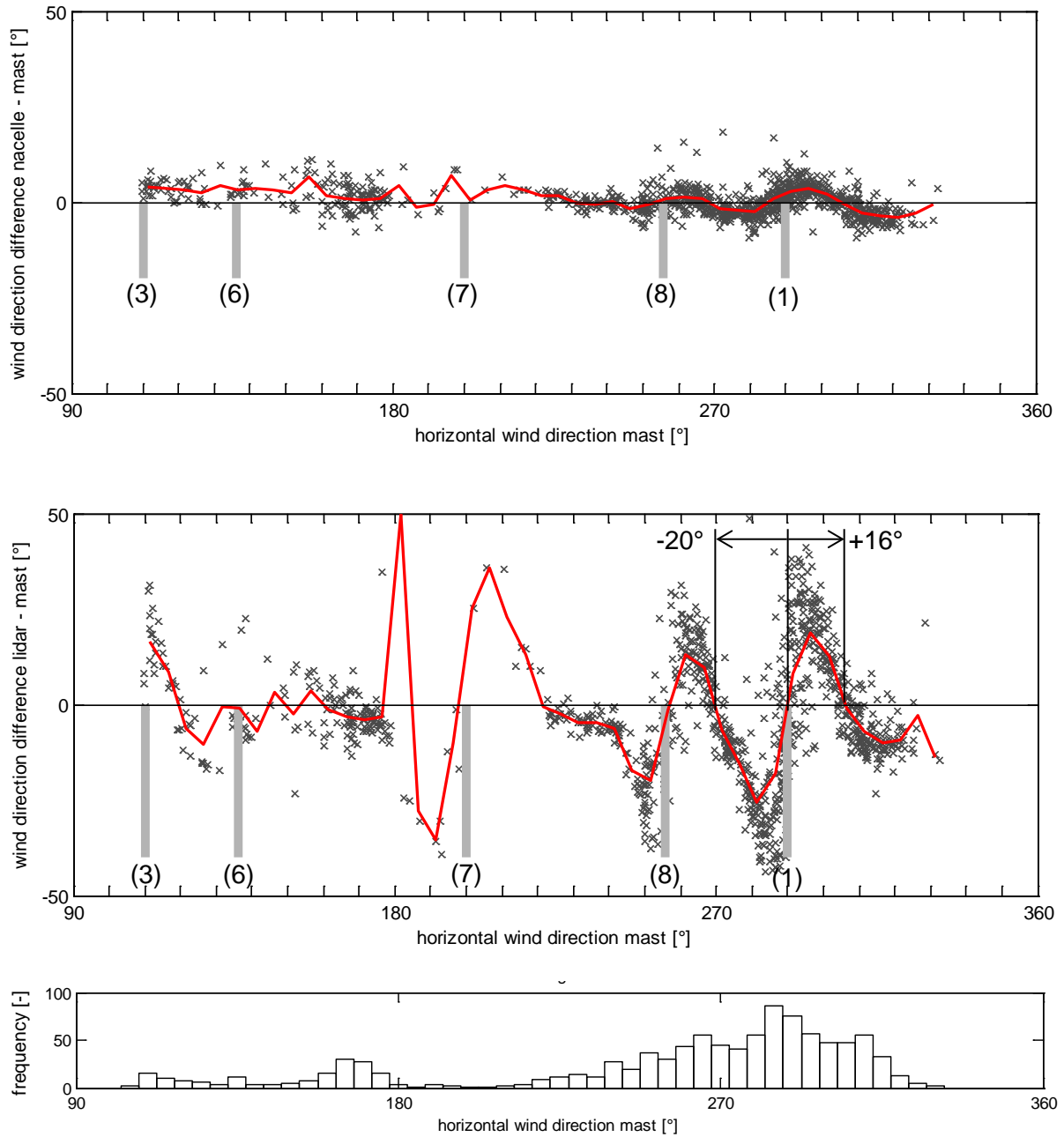
Figure 5-22: Deviations of nacelle (top) and lidar (middle) wind direction measurements from met mast reference, relative to the met mast wind direction.
Solid line: Mean difference per direction bin of five degrees.
Vertical lines below zero indicate directions of neighbouring turbines relative to the instrumented turbine, according toFigure 5-7.
Bottom: Frequency of wind directions measured by the mast sensor.

This substantial weakness of the directional lidar signal can be explained by the measurement principle and parameter reconstruction method: The measurements are distributed over a sphere segment of 100 m diameter, whereby wakes likely are able to cover a part of the measurement area, resulting in horizontal shear. However, the reconstruction method, as shown in Section 4.1, relies on the assumption of zero

horizontal shear. As this assumption is violated, wake induced horizontal shear is misinterpreted as horizontal direction, causing the observed differences to the mast reference.

The problem is illustrated by considering different orientations of the turbine – and thereby wake situations – in Figure 5-23. Turbine (2) with rotor diameter D is assumed to be located downwind turbine (1) with the same rotor diameter. The turbines are further assumed to be equally oriented. The wake of turbine (1) is modelled to approach turbine (2) in the direction of the turbine orientation (no yaw error) and without any other wake movement (no meandering) or resizing (no wake widening). The outer circle of the lidar measurement of turbine (2) has a diameter of 100 m and is located at a distance of 86.6 m to the turbine.

The situation in which the wake of turbine (1) just not touches the lidar measurement is illustrated in Figure 5-23 in the first and fifth situation ("no wake"). It was considered in Subsection 5.1.6 and the relative angle limit was found to around $\delta_{\mathrm{h}}^* = \pm 14°$.

At straight orientation towards the neighbouring turbine, the full wake hits the lidar measurement (Figure 5-23, middle). Here, too, the wake does not affect the direction calculation by the lidar.

Between these two situations a partial wake affects the region of the lidar measurement and hence distorts the wind direction calculation. If the left lidar measurement area is in the wake of turbine (1), the lidar direction interpretation assumes too large directions, and if the right area is in the wake, too small directions are concluded.
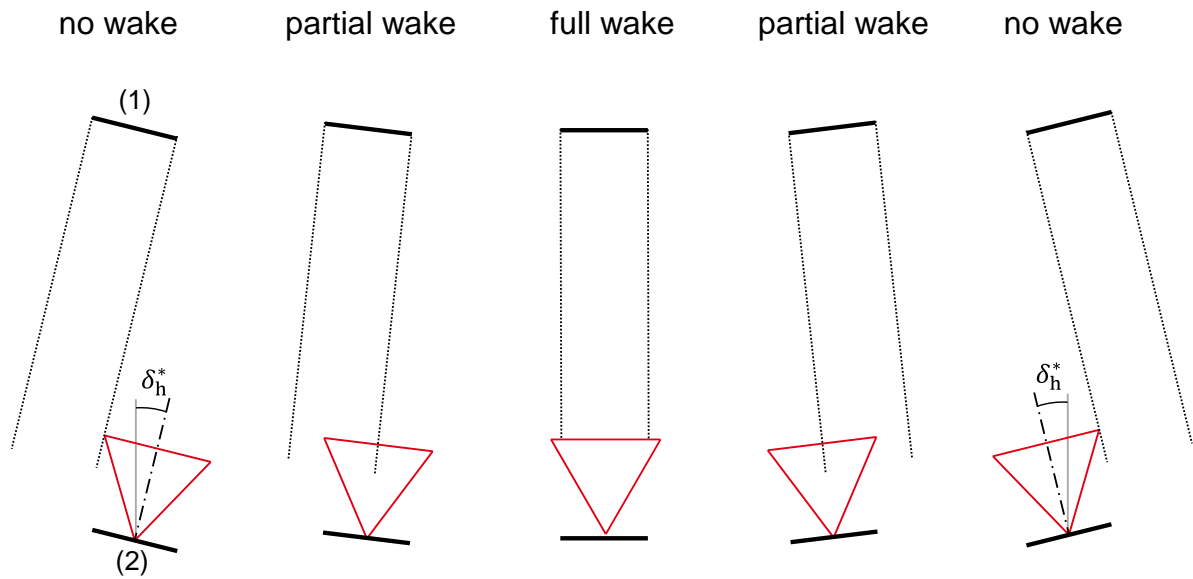
Figure 5-23: Different wake effects on the lidar measurement
Left and right (no wake): Geometric situation in which the projected wake margin of turbine (1), dotted, touches the edge of the lidar scan, red, at turbine (2).
Second and fourth situation (partial wake): Maximum/ minimum observed horizontal shear and hence direction misinterpretation is expected.
Middle (full wake): Wake effect is centred in the measurement area with minor average effect on the calculated wind direction.

The theoretical determination of the wake limit can be verified in the experiment. According to Figure 5-22 at direction (1) -20° and +16° respectively, the averaged wind direction difference crosses zero, matching the theoretical limits $\pm 14°$ well. Thereby it is indicated that the assumption of a "frozen" wake evolution is sufficient in the sense to estimate directions of possible wake effects in the measurement.

Between the situations of no wake effect and full wake, the observed direction error reaches its maximum and minimum respectively, so that during one complete cycle – no wake, partial wake, full wake, partial wake and no wake, as illustrated in Figure 5-23 – in good approximation a sinusoidal[1] symmetrical behaviour of the direction error can be observed.

A supplementary analysis in Figure 5-24 does not indicate any noticeable dependency of this behaviour on the average wind speed in the analysable range between 4 and 10 meters per second.

---

[1] Sinusoidal behaviour can be expected if the lidar sphere diameter is not significantly larger than the rotor diameter of the wake generating turbine.
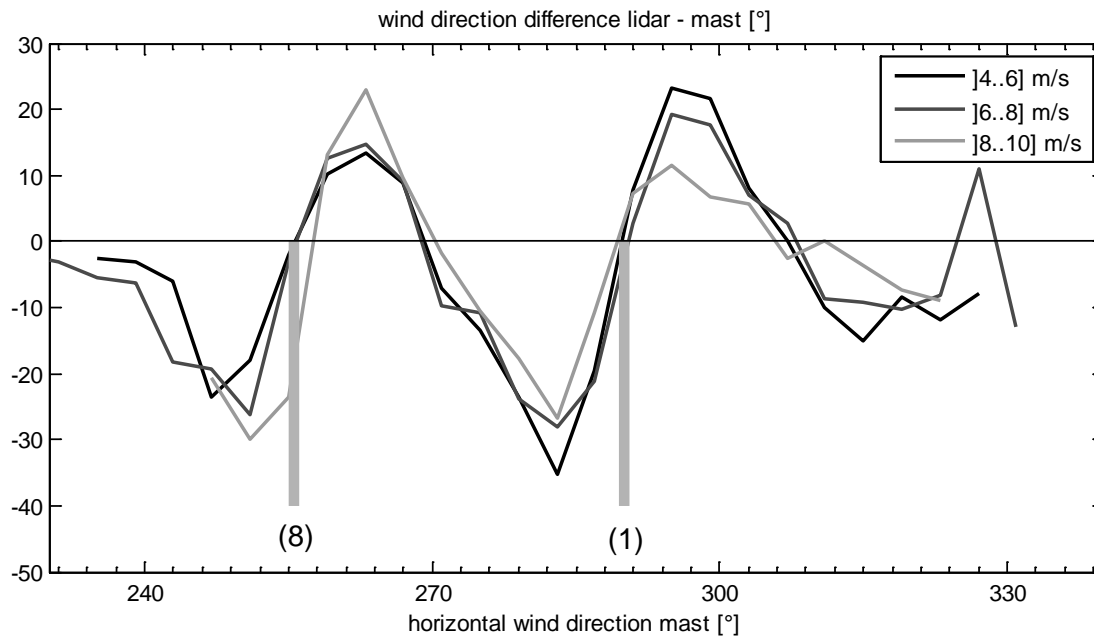
Figure 5-24: Mean wind direction differences between lidar and mast reference, evaluated for three wind speed ranges, comprising 30%, 31% and 13% of total 1004 ten minute intervals, respectively. Independent of the wind speed, the wind direction estimation errors behave similarly.

Wake Effect Observation by the Two-Dimensional Scanning Lidar

The described phenomenon is finally verified by the direct observation of spatially distributed wind speeds over the measurement segment during an event of yawing into the wake of a neighbouring turbine. In Figure 5-25 lidar measurements in beam direction are projected onto the u-component of the wind direction, i.e. towards the turbine, averaged within ten seconds of measurement and illustrated colour coded. In Figure 5-26 the wind direction reconstructed using the lidar measurements and the three parameter model besides the direction measured by the nacelle sensor and the yaw direction are plotted.

During seconds 251 to 300 the inflow can be approximated homogeneously and the calculated wind direction parameter is below 15°, showing similarity to nacelle measured direction.

During seconds 301 to 360 low wind speeds in the right measurement area and inhomogeneous inflow can be observed. The nacelle sensor measures significantly larger directions (+19.1° in average). Why does the lidar not see the increasing direction? As the wind changes from 271° to 271°+13°=284°, the direction leaves the undisturbed sector and the partial wake of turbine (1) hits the right measurement area of the lidar. This causes underestimated wind directions.

During seconds 355 to 385 the turbine yaws by +10°, the inflow is non-stationary (changing with time) as seen from the lidar, and inhomogeneous. After yawing (seconds 391 to 400), a clear area of reduced wind speed in the lower right area of

the circle can be observed, which is the area of the projected wake of turbine (1). Again, the partial wake of turbine (1) hits the measurement and the direction is underestimated by more than 20°.
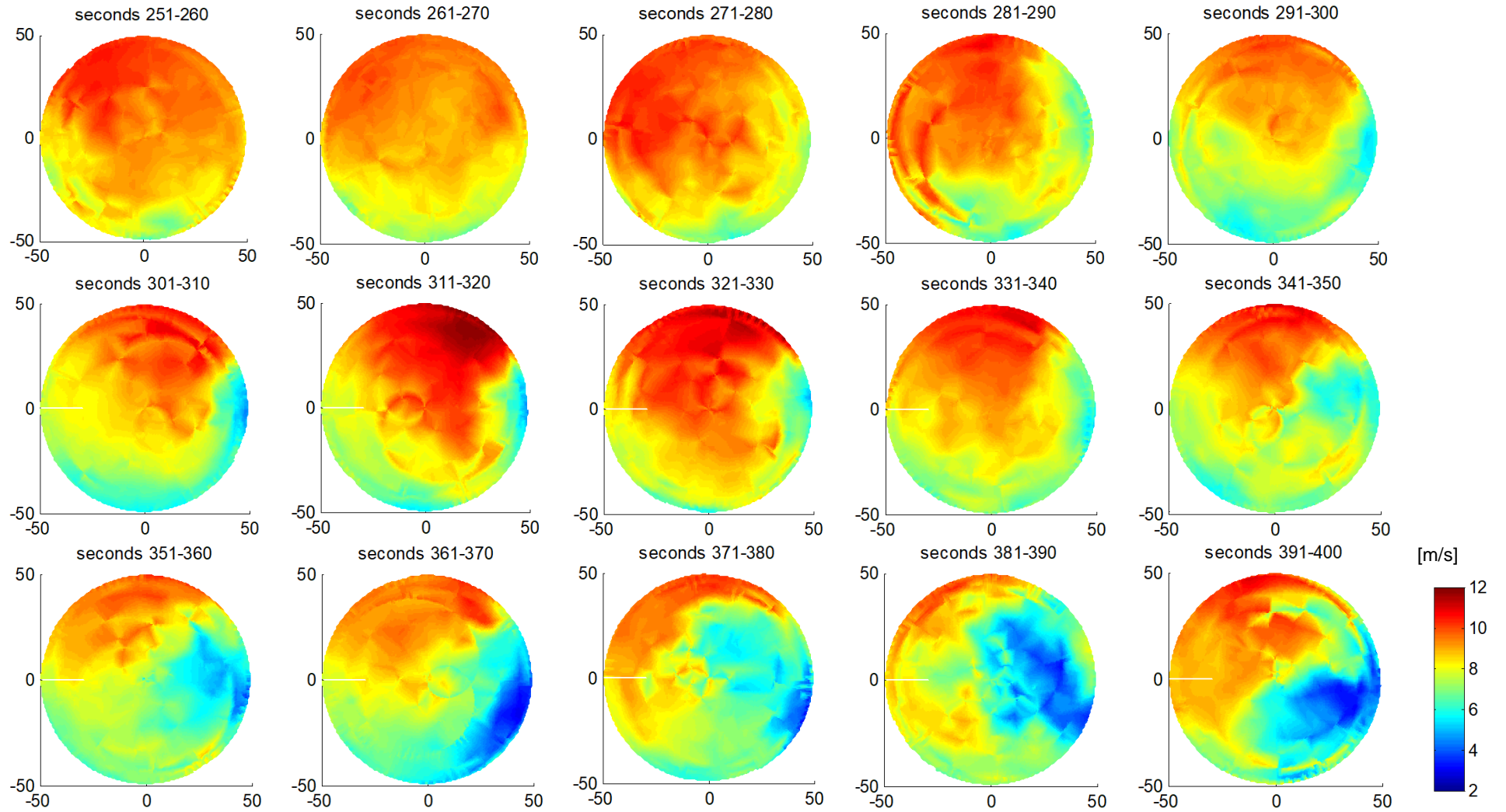
Figure 5-25: Lidar measurement projections onto the u-component during measurements on 2012-09-04 at 14:30. At seconds 381 to 400 reduced wind speeds in the lower right area indicate the wake of neighbouring turbine (1).
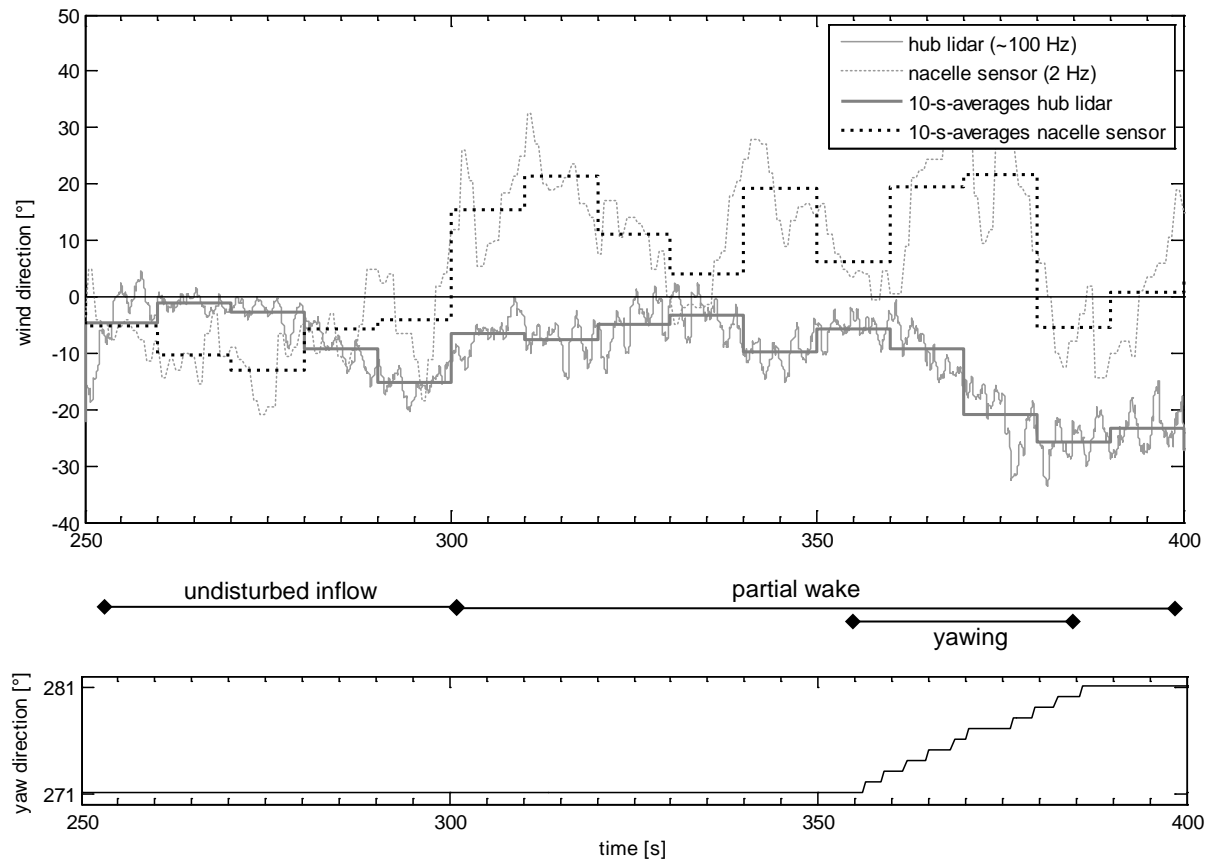
Figure 5-26: Time series of lidar and nacelle measured wind direction

(top) and yaw direction (bottom) during the same time period as in Figure 5-25. (The quantisation of the 20 Hz yaw signal is 1° making the signal looking step-like, although the actual yaw speed is constant)

5.3.3 Wind Shear Detection by the Two-Dimensional Scanning Lidar

Advantages of the high temporal and spatial resolution of the two-dimensional scan strategy shall be demonstrated by exemplarily analysing the wind shear parameter included in several wind field models presented in Chapter 4.

During a selected interval of 24 seconds, a fast drop in the calculated vertical shear parameter can be observed in Figure 5-27, while the averaged horizontal wind speed remains approximately constant and the horizontal wind direction decreases slightly from +8° to -8°. This change in shear of $0.04 \, s^{-1}$ or equivalently 3.2 meters per second wind speed difference between the upper and lower blade position within 5 seconds leads to varying asymmetric loads on the rotor.

An individual pitch controller with one sinusoidal pitch activity per rotor revolution (1P-IPC) would be able to mitigate these loads assuming the tracking speed is sufficiently high, which should be adequate in this case at a first glance.
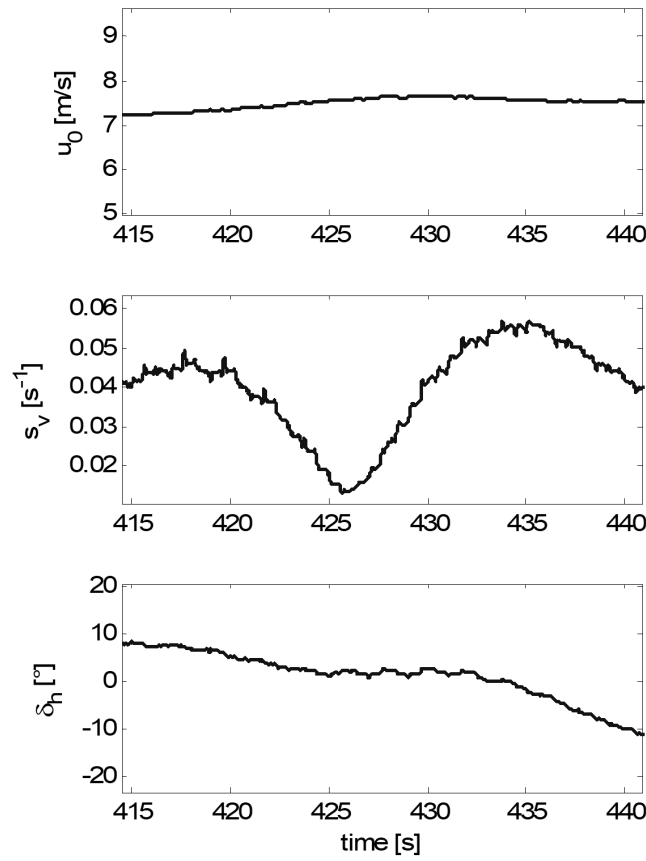
Figure 5-27: Time series of wind speed, vertical shear and direction calculated using the three parameter model.
The time period is the same as in Figure 5-28. Around ten seconds of data are running averaged and centred at
half of the averaging interval.
The linearly approximated shear changes remarkably.

A more detailed analysis can be carried out by considering all two-dimensionally distributed measurements recorded at high sampling frequency of 200 Hz by the hub lidar system. Around two seconds of recorded wind speeds in beam direction are combined to a circular plot, showing the wind speed projections on the u-component towards the turbine colour coded. Twelve plots of this type illustrate the considered interval in Figure 5-28.

At the beginning of this interval there are two areas of low wind speed in the left and bottom area seen from the spinner resulting in a net positive vertical shear. At second 427 wind speeds are almost equally distributed. At seconds 431 to 437 one significant area of high wind speed in the top left area of the rotor develops again resulting in net positive vertical shear. The change in net vertical shear agrees with Figure 5-27.

In contrast, the different wind field characteristics before and after the drop in shear are much more precisely described by the comprehensive analysis than using one

linear parameter. With the development of a more sophisticated wind speed model the input for a more advanced (e.g. *2P-)* individual pitch controller could be generated resulting in further load mitigation potential for a lidar based pitch control strategy.

Figure 5-28: Lidar measured change in the distribution of wind speeds over the rotor plane at a sampling rate of 200 Hz on 2012-09-11 at 23:40. Colour coded are wind speeds measured in beam direction and projected on the u-component towards the turbine.
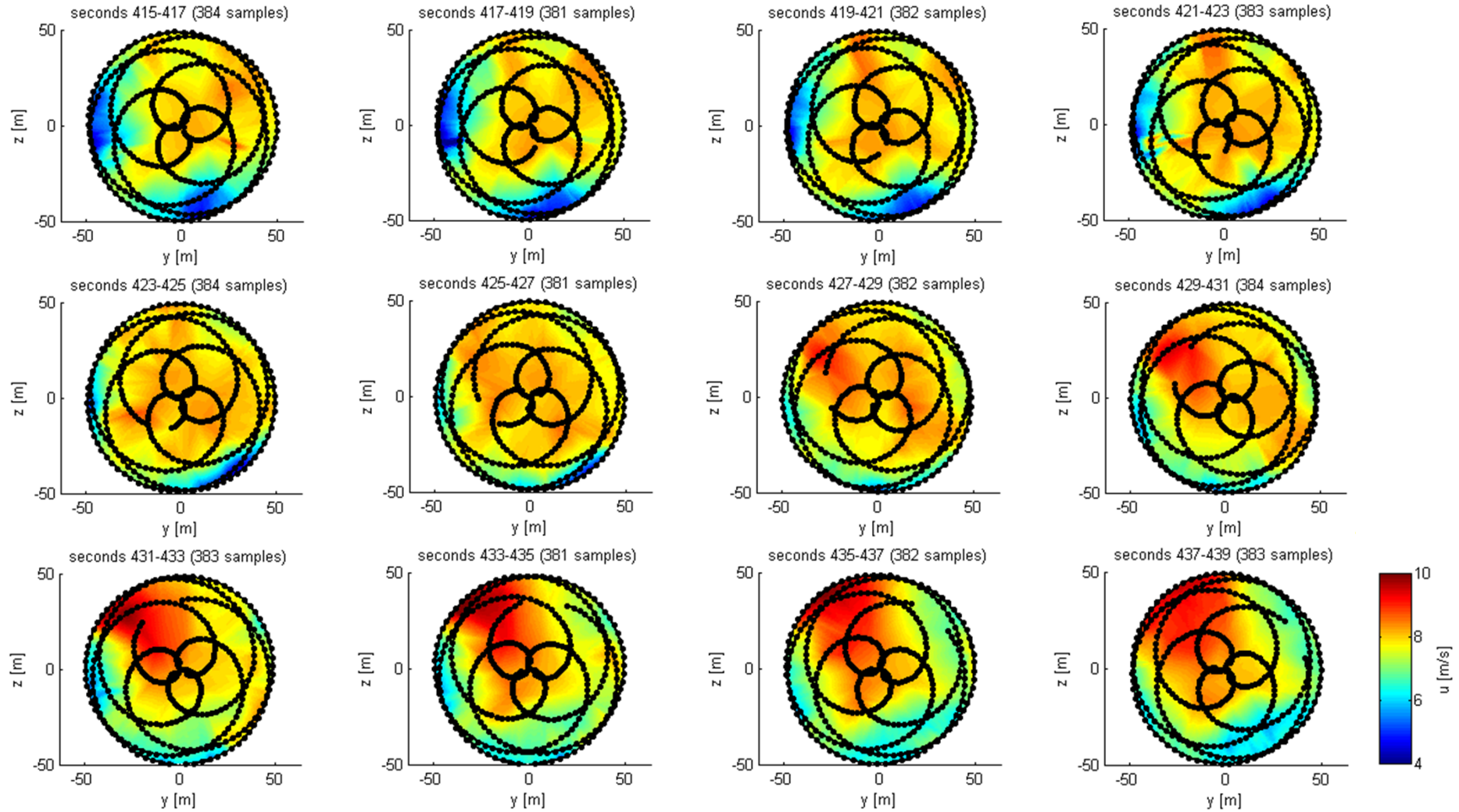
5.4   Measurement Conclusions

In this chapter, data of the first experimental spinner integrated two-dimensional scanning lidar have been processed and analysed. It is found that data processing methods known from vertical wind lidars differ and may necessitate advancements, namely:

- The explicit consideration and treating of outliers in the backscatter spectra, which frequently occur during downwards oriented beams, horizontally or upwards pointing on obstacles or clouds, or in the case of window reflections.

- Secondly, the need for real time and uninterrupted data if control applications are to be served, for example by adequate interpolation.

- The trade-off between higher sampling rate and decreased sensitivity does not exclude rates of up to 500 Hz.

The processed data can then be used to reconstruct wind field characteristics. A three parameter wind field model comprising wind speed, horizontal direction and vertical shear can be fit in case of measurements from a plane in one upwind distance.

The comparison of averaged hub lidar wind speed data to standard nacelle anemometer recordings points out the ability to measure the wind speed deficit produced by the rotor and potentially allows for accurate rotor averaged wind speeds on a smaller time scale. In a wind farm the lidar statistically measures similar wind speed reductions, depending on the turbine orientation, as a nacelle sensor. Thanks to the upwind remote measurement principle, the horizontal wind speed signal seems to be suitable for feed forward pitch control, see Chapter 6, or for other monitoring or safety functions of the turbine operation.

Averaged wind direction data is affected by substantial systematical errors. Two reasons explain the phenomenon:

- In a wind farm, the lidar likely covers wake effects in parts of the two-dimensional measurement segment.

- Due to the limitations of the remote measurements in beam direction and at one focus distance, partial wake effects are inherently misinterpreted to erroneous wind directions.

The maximum errors, up to 49° in 10-minute-averaged measurements, occur when approximately half of the measurement area is covered by a wake. Since all yaw orientations in partial wake directions in a wind farm are affected, which accounts for 60% of all directions in the considered wind farm, during a large proportion of the operating time the direction signal cannot be used reasonably.

Thereby the successful application of lidar systems in wind farms, measuring at one distance, and used for wind direction recordings or yaw control, can be put into question. Potentially, the wind direction reconstruction method proposed in Section 4.2.2 could overcome these restrictions by employing measurements in a second axial distance.

Beneficially the considered high resolving two-dimensional scanning hub lidar can be applied for the study and online detection of wind field structures more complex than linear shear, which could for instance enable higher harmonic pitch control based on lidar signals.

6 Simulation of Lidar Based Wind Turbine Control

After the theoretical considerations regarding modelling and characterisation of inflow wind fields using turbine mounted lidars in Chapter 4 and the experimental testing of advanced setups in Chapter 5, now the focus will be on the application of inflow measurements for pitch control of modern wind turbines and the evaluation via simulation techniques.

Computational simulations become particularly important for several reasons:

- Simulations are reproducible so that the influence of selected simulation parameters can be determined qualitatively and quantitatively.

- The considered control mechanism may not be implemented with all required aspects regarding safety and certification or real-time capability.

- The necessary environmental conditions, especially desired varying wind speeds may require too long measurement periods or might not occur at all.

- The investigated lidar system may not yet exist, or the changes to an experimental lidar setup would require inacceptable efforts.

Here, an integrated approach is applied taking into account all steps from the study of lidar measurement principles, wind field characterisation methods, wind evolution theories, wind turbine structure interactions and impacts on turbine operation, power production, loads and life time of different components. By that, the overall influence of each variation in the configuration can be examined.

This chapter is organized as follows: In Section 6.1 the concept of lidar based pitch control simulation is introduced. Dedicated extensions for wind measurement simulation are presented, filter design methods are developed and feedforward simulation structures are shown.

The load reduction potential of simulated lidar based pitch control is presented in Section 6.2 including a sensitivity analysis. Further applications which could benefit from lidar assistance are discussed in Section 6.3 and summarized together with the results of the pitch control simulations in Section 6.4.

The used aeroelastic computer-aided engineering (CAE) and simulation tool FAST [84] allows the definition of arbitrary real or generic, onshore or offshore, upwind or downwind, two or three bladed wind turbine models of arbitrary geometry, aerodynamic, mechanical and electrical behaviour.

Here, a generic 2.5-MW wind turbine model is applied in the load simulations, whose behaviour is well tested and is in accordance with models of similar real wind turbines. Its basic parameters are listed in Table 6-1 and the steady state

characteristics of rotor speed, electrical power and pitch angle are plotted in Figure B.1-1 in Appendix B.1.

The turbine coordinates and loads referred to in this Chapter are given in Figure 6-2.

Selected contents of this chapter have previously been published in [85].

Table 6-1: Characteristics of the generic reference wind turbine model

Rated power	2.5 MW
IEC class	IIa
Number of blades	3
Rotor diameter	90.37 m
Hub height	95.45 m
Shaft tilt	5°
Rated rotor speed	15.85 rpm
Rotor speed range	10.57..16.29 rpm
Cut in wind speed	3.22 m/s
Cut out wind speed	25 m/s
Rated wind speed	10.71 m/s
Partial load pitch angle	2.1°
Gearbox Ratio	1 : 113.56
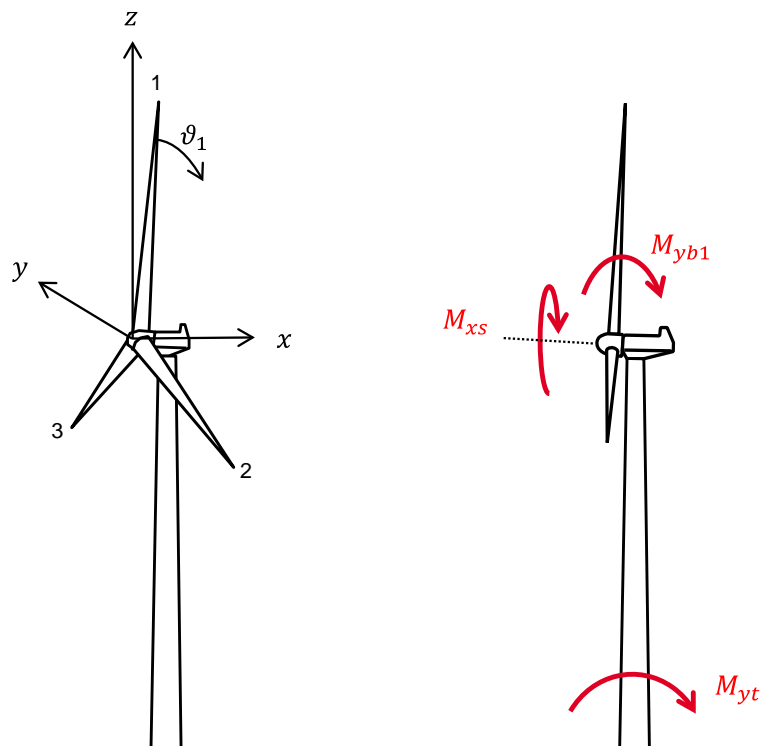
Figure 6-1: Non-rotating non-tilted turbine coordinate system (left)
and investigated loads in rotating tilted system (right)

6.1   Simulation of Lidar based Feedforward Pitch Control

Originally, aeroelastic computer tools used for the simulation of wind turbines were not designed to simulate lidar wind speed measurements and to integrate a feedforward control strategy. Recently, several tools have been extended in this respect.

In [86] an extension of the commercial wind turbine design software Bladed [87] is used in a study on an offshore wind turbine model with collective feedforward pitch control based on lidar. The extension includes the simulation of simultaneous pulsed measurements as well as continuous-wave (cw) measurements and can be connected via a dynamic-link library to the controller. In [88] the modelling of pulsed and cw lidar measurements for the use in the freely available simulation tool FAST is described. The focus is on the use of a circular scanning cw lidar system and on the influence of distance and scan radius. In [25] a simplified wind speed measurement extension for the design tool FLEX5 has been developed and used for testing model predictive control strategies.

Here, an extension for FAST has been developed independently for cw lidar simulations to provide high flexibility in modelling, parameterization and testing of lidar systems.

The structure of the enhancement is organized in a sequence of data processing steps, starting from wind data handling, wind evolution considerations, measurement simulation, wind field parameter reconstruction, feedforward control algorithm and filtering, see Figure 6-2. The particular elements of the sequence, also referred to as lidar measurement chain in the following, are explained in Subsections 6.1.1 to 6.1.6. The applied feedback control loops for rotor speed Ω and blade loads M_{ybi} are given in Subsection 6.1.7.
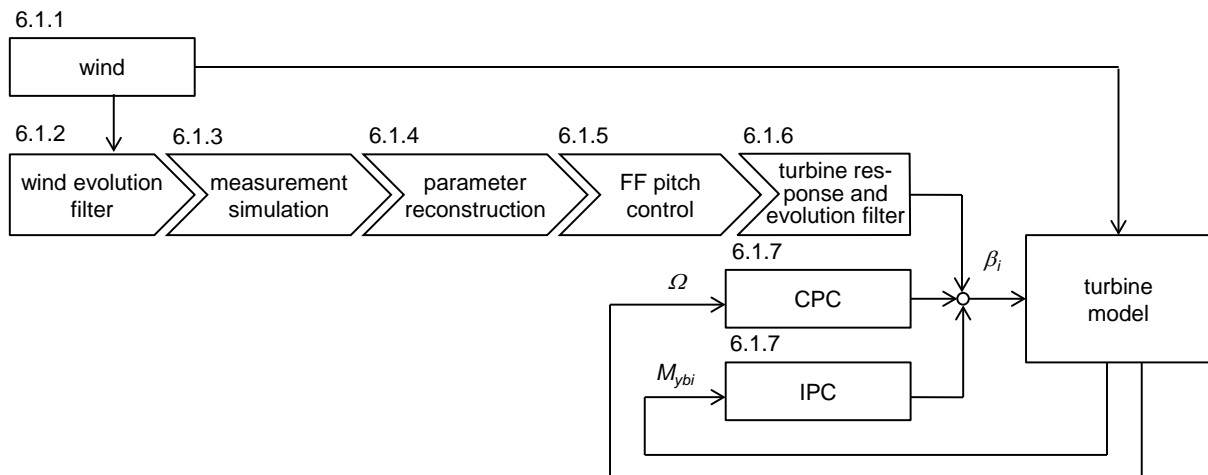

Figure 6-2: Structure of a feedforward blade pitch control scheme with upstream lidar measurement chain and reference to the subsections of the chapter.

6.1.1 **Wind Field Generation and Preparation**

Load cases for wind turbine load simulations are composed of the combination of environmental conditions, i.e. especially inflow wind fields, and turbine operational states. Simulator tools like TurbSim [89] for FAST include algorithms for stochastic processes constructing three-dimensional wind vector fields on a three-dimensional geometry in such a way that given statistical wind field parameters like mean wind speed, turbulence intensity, spectrum and coherence are achieved.

The chosen wind field parameters are given in Table 6-2 enabling 60 simulations with 12 mean wind speeds and 5 wind direction combinations per mean wind speed.

Table 6-2: Wind definition parameters

Wind speed bins	12 (2 to 24 m/s)					
Wind directions	combination	1	2	3	4	5
	horizontal	0°	-8°	8°	0°	0°
	vertical	0°	0°	0°	-6°	6°
Annual averaged wind speed	8.5 m/s					
IEC turbulence type	NTM					
Turbulence class	A					
Turbulence model	Kaimal					
Power law exponent	0.2					
Wind field grid	21 x 21					
Wind fields per second	20					
Length	720 s usable					
	660 s simulated					

Since the desired information of an inflow wind field of a horizontal axis wind turbine rotor is located on a disk, it is computationally advantageous to process the wind data and the lidar simulation on a polar coordinate grid with the origin lying in the centre of the hub. If the wind field data was obtained on a rectangular Cartesian grid the transformation into the polar grid is necessary.
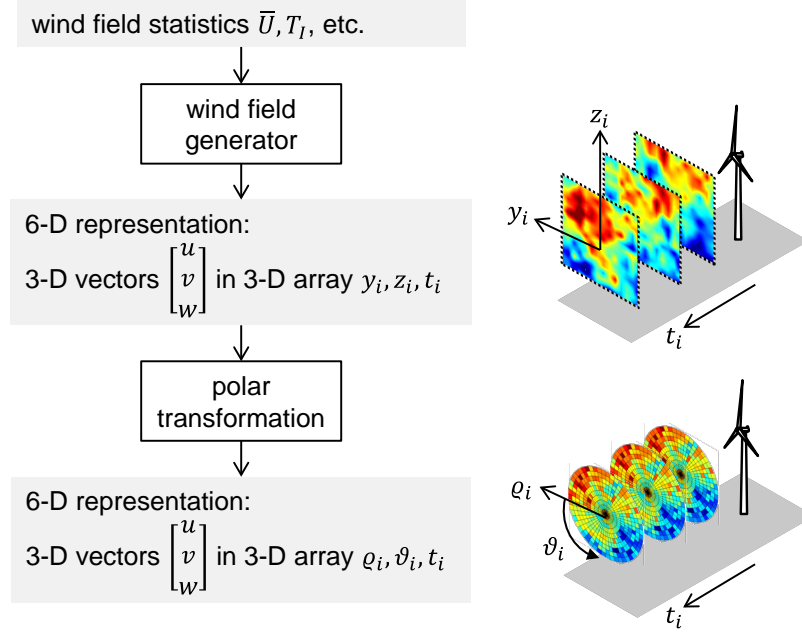
Figure 6-3: Wind field generation and transformation. The u-component is shown in the sketch colour coded on consecutive planes in Cartesian coordinates (middle) for the turbine simulation in FAST and in polar coordinates (bottom) for the developed lidar simulator.

There exist several computational methods to interpolate data from one grid to another, like the function *griddata* or *TriScatteredInterp* in Matlab [90], [91]. *griddata* constructs for each time step a triangulated mesh according to the Delaunay triangulation method. For each triangle a linear, cubic or nearest-neighbour fit gives the interpolant. The existing algorithms are computationally intensive when applied to standard IEC wind fields [92] of e.g. 21 times 21 points and 13,200 time steps.

Conveniently, for all time steps and independent of the interpolation method, the positions of the original and interpolated grid remain the same, so the calculation task is identical for all time steps. Consequently a transformation matrix M can be constructed mapping all values given in Cartesian coordinates U_c onto values in polar coordinates U_p:

$$U_p = M \cdot U_c$$

<div align="right">(6.1)</div>

The matrix elements $M_{i,j}$ depend on the interpolation method and have to be determined only once.

Since the desired wind inflow characteristics are valid for the original Cartesian grid only, the transformation should aim at distorting the grid and the information to a minimum. Therefore, interpolation methods such as linear or cubic should be avoided, while the nearest-neighbour-method shows good results if at least the grid points on $y = 0$ and $z = 0$ are identical. Therefore, the numbers of horizontal and vertical points of the Cartesian grid need to be uneven and equal.

Exemplarily, in Figure B.2-1 and Figure B.2-2 in the Appendix resulting matrices for the nearest neighbour and linear interpolation methods are illustrated. They are of sparse type and allow the efficient calculation of a large set of wind fields, especially by using software optimized for matrix operations like Matlab or Octave. Wind field transformations using the proposed matrix method were found to be faster by orders of 13 to 17, when compared to the methods *griddata* and *TriScatteredInterp* integrated in Matlab.
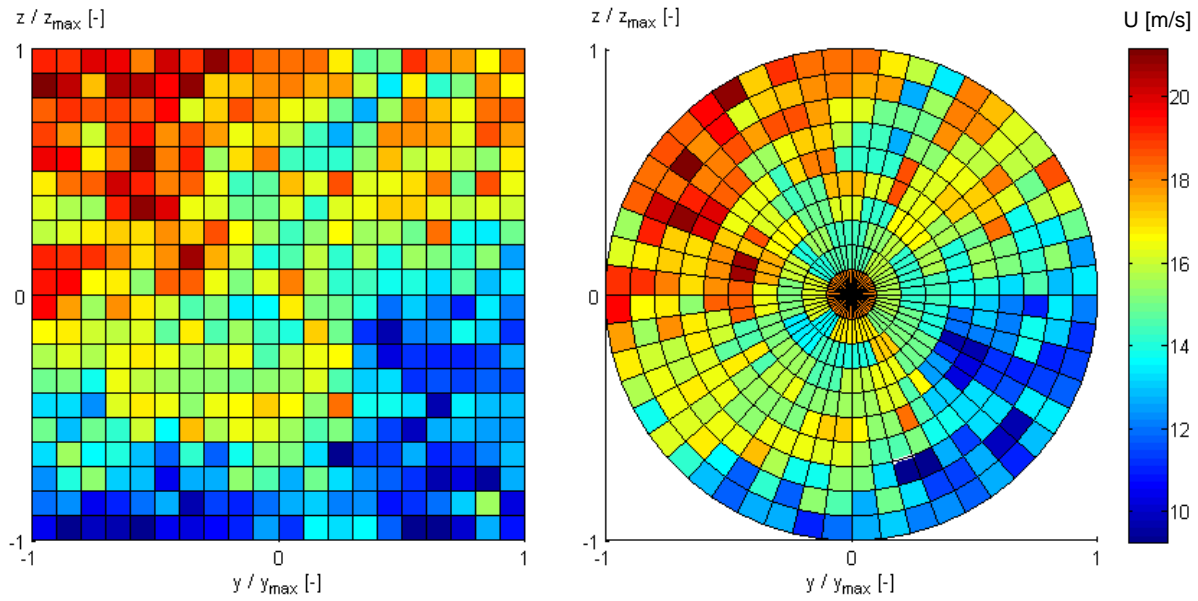
Figure 6-4: Simulated wind speed u-component in Cartesian and polar grid obtained by Equation (6.1) and nearest neighbour interpolation.

6.1.2 Wind Field Evolution

The issue of wind conditions changing between one or more measurement distances and the rotor plane has been discussed in Chapter 3.1.

Two effects have to be distinguished:

- Deterministic, reproducible inflow behaviour, which is dominated by the wind speed induction effect, can be compensated by static, rotor speed and wind speed dependent correction methods. In simulations these effects are inherently considered by the blade-element momentum theory rather than by modifying the inflow field. In real lidar applications, in contrast, the induction effect has a relevant influence and needs to be considered.

- Turbulence effects cannot be compensated as they are represented by stochastic processes. Since turbulent wind evolution occurs dominantly at smaller structures, i.e. small wave lengths or equivalently larger wave numbers and signal frequencies.

One possibility to take into account the turbulence effects is to apply a low pass filter on subsequent wind components in main wind direction for all grid points, so that the simulated lidar cannot measure these unpredictable high frequent wind speed fluctuations.[2] Using a forward-backward filter avoids time shift and signal distortion. The cut-off frequencies can be derived e.g. from experimental data of approaching wind simultaneously measured at different distances with a non-scanning lidar as described in Subsection 3.1.2. The phase of the cross spectrum of the two separated measurements in same direction was used as a measure of the linear dependency of the signals. The wavenumber limits at which the measured phase clearly deviates from the linear phase determined the limiting wavenumbers, and together with the mean wind speed, the cut-off frequencies can be determined.

In a more advanced approach by Bossanyi [93] decorrelated wind speed signals are explicitly modelled for lidar simulations based on theoretical coherence functions of Kristensen [94].

In Subsection 6.1.6 the developed filter of the feedforward signal takes into account, beside other requirements, the unpredictable frequencies discussed here.

6.1.3 Lidar Measurement Simulation

Measurements by turbine mounted lidars are influenced by the volume averaging effect briefly introduced in Subsection 3.2.3. Here, a practical implementation with truncated volume is described and the proportion of the remaining usable lidar measurements due to this simplification is calculated.

The simulated wind speed measurements in beam direction coordinate ξ, where $\xi = 0$ indicates the focus point, are therefore weighted by the function

$$w(\xi) = \frac{1}{\pi} \frac{z_R}{z_R^2 + \xi^2} \tag{6.2}$$

where z_R is the Rayleigh length parameter given by (3.2).

A normalized weighting function is defined by

$$w_{\text{norm}}(\xi) = \frac{w(\xi)}{w(0)}. \tag{6.3}$$

This weighting function (6.3) has to be set to zero at a certain minimum weighting level $w_{\text{norm,min}}$ due to the finiteness of the available computational data.

Using the integral of Equation (6.2)

---

[2] In the regarded simulations, as a computationally more friendly approximation, the filter is applied to the measurements in beam direction directly, instead of to the wind speeds in main wind direction.

$$W(\xi) = \int_0^{\xi} w(\zeta)\, d\zeta$$
$$= \frac{1}{\pi} \operatorname{atan}\left(\frac{\xi}{z_R}\right), \tag{6.4}$$

the integral of the used truncated symmetric part of w becomes

$$W_{\text{used}}(\xi) = W(\xi) - W(-\xi)$$
$$= \frac{2}{\pi} \operatorname{atan}\left(\frac{\xi}{z_R}\right). \tag{6.5}$$

Then, W_{used} can also be expressed as a function of $w_{\text{norm,min}}$ applying algebraic conversions, resulting in

$$W_{\text{used}}(w_{\text{norm,min}}) = \frac{2}{\pi} \operatorname{atan}\left(\sqrt{\frac{1}{w_{\text{norm,min}}} - 1}\right). \tag{6.6}$$

Equation (6.6) is plotted in the right part of Figure 6-5. The left plot represents the proportion of usable lidar measurements in the simulation. Choosing a lower limit of e.g. $w_{\text{norm,min}} = 0.1$ implies that around 80% of the backscatter measurements are covered. Note that the used part is independent of the Rayleigh length z_R and hence independent of the focus length of a continuous-wave lidar.
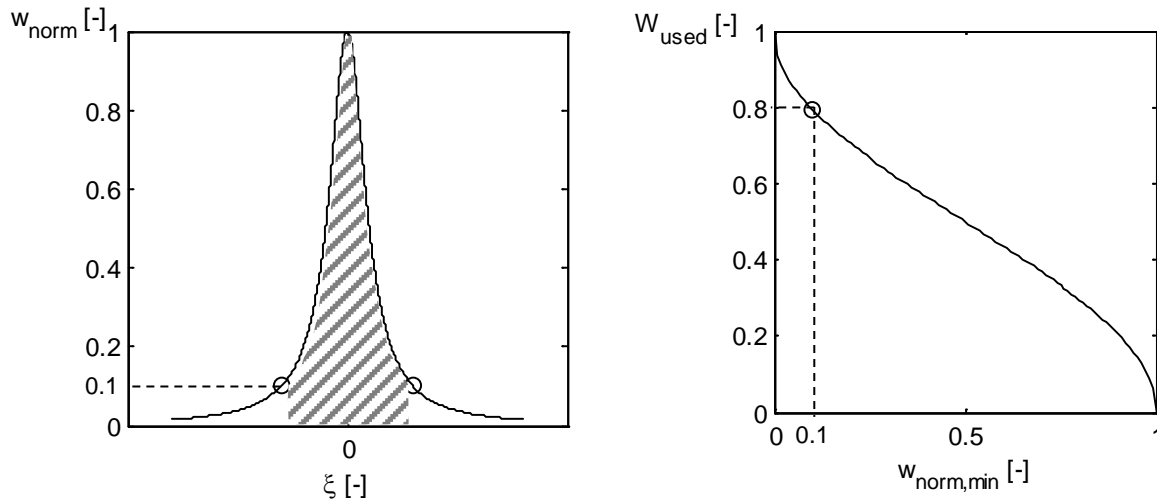
Figure 6-5: Part of the lidar weighting function used in the measurement simulation.
Left: Illustrated as the area below the weighting function for $w_{norm,min} = 0.1$.
Right: As a function of $w_{norm,min}$, 0.1 is marked.

For applying the described method, the radial extension of the wind field needs to be larger than the rotor swept area. This additional space depends on the chosen value of w_{norm}, the maximum scan angle and the focus distance.

The algorithms can be simplified considerably without introducing significant inaccuracies, if fast sequential lidar measurements within a short time interval of e.g. one second can be regarded to arise simultaneously.

6.1.4 Reconstruction

In a next step the simulated lidar measurements are aggregated to characteristic parameters of each consecutive wind field. The wind field parameters are calculated as presented in Chapter 4 and are used to calculate feedforward pitch angles later.

Important variables are the number of reconstructed parameters, depending on the scan strategy, the weighting of measurements according to their position on the rotor plane and their impact on the blades, and the number of aggregated measurements per time interval. Later on in this study, circular scanning in 32 equiangular directions with equal weighting and the aggregation of one scan figure per second is chosen.

6.1.5 Feedforward Pitch Control Strategy

In Section 1.2 feedforward control concepts using preview wind information have been reviewed briefly. Here the focus is not on the comparison of different feedforward control strategies, but on the variation of several parameters within the lidar measurement chain.

Therefore, a control strategy is favoured which

- can easily be added to conventional collective (CPC) and combined collective and individual (CPC + IPC) feedback controllers without changing them,

- thus allows the transparent comparison to the conventional controllers,

- enables extensive numerical simulations for parameter variations and load case studies.

A static compensation method for both collective feedforward (CFF) and individual feedforward (IFF) pitch angles is implemented here

For CFF pitch control, the steady state behaviour of the optimal pitch and wind speed is used. The relation associated with the generic wind turbine model is given in Figure B.1-1, bottom. For each rotor averaged wind speed

$$u = u_0 \cos(\delta_h) \cos(\delta_v + \tau).$$

(6.7)

with the wind field parameters rotor averaged wind speed u_0 in rotor averaged horizontal and vertical wind directions δ_h, δ_v and rotor tilt angle τ, the optimal pitch angle is interpolated from the steady state characteristics. In the simulations, first the linear 3pe method with $\delta_h = \delta_v = 0$ is used. Later in the sensitivity analysis, the 5pe method is considered with all parameters including δ_h and δ_v.

For IFF pitch control, the steady state behaviour of load alleviating 1P individual feedback pitch control is studied. Synthetic homogeneous wind fields with independently varying horizontal and vertical linear shear and horizontal and vertical constant inflow direction are generated and the generic wind turbine model with flexible blades, but with a stiff tower and no gravitational effects, and 1P IPC is simulated. After a short transient startup time, stationary pitch amplitudes and phases result
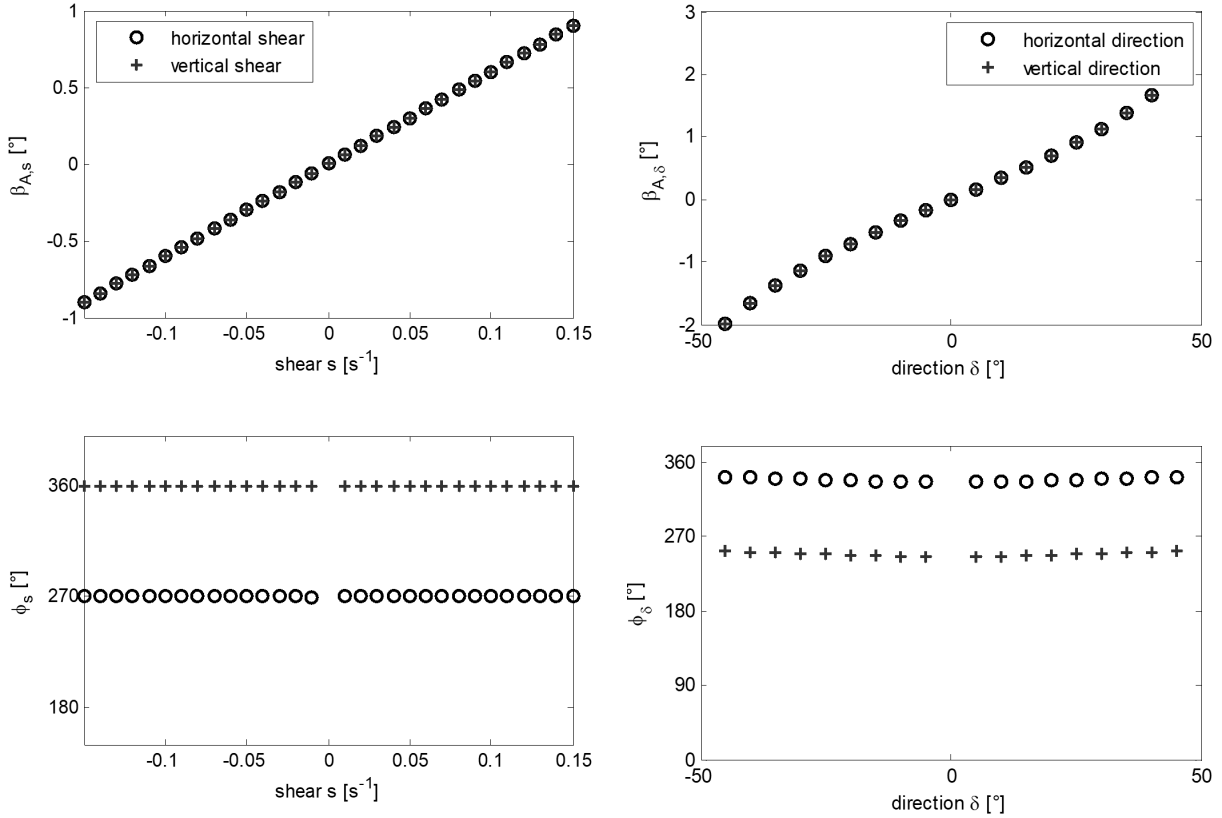
Figure 6-6: Stationary pitch amplitudes (upper row) and phases (lower row) for homogeneous wind fields of mean wind speed 16 meters per second and varying linear shear and homogeneous direction.

The obtained stationary pitch amplitudes β_A shown in Figure 6-6 (top) increase approximately linearly with the wind shear s and the flow direction angle δ. The slopes of these relations are approximated by a linear fit to result in mean differential pitch amplitude changes, e.g. $\frac{\overline{d\beta_{A,sh}}}{ds_h}$ for the horizontal shear. Phases ϕ can be considered constant and differ by 90 degrees from horizontal to vertical shear or inflow direction.

The overall individual feedforward pitch angle $\beta_{FF,i}$ of the i-th blade is then given by

$$
\begin{aligned}
\beta_{FF,i} = \ \beta_{CFF} &+ s_h \frac{\overline{\mathrm{d}\beta_{A,sh}}}{\mathrm{d}s_h} \cos(\vartheta_i - \phi_{sh}) \\
&+ s_v \frac{\overline{\mathrm{d}\beta_{A,sv}}}{\mathrm{d}s_v} \cos(\vartheta_i - \phi_{sv}) \\
&+ \delta_h \frac{\overline{\mathrm{d}\beta_{A,\delta h}}}{\mathrm{d}\delta_h} \cos(\vartheta_i - \phi_{\delta h}) \\
&+ \underbrace{\delta_v \frac{\overline{\mathrm{d}\beta_{A,\delta v}}}{\mathrm{d}\delta_v} \cos(\vartheta_i - \phi_{\delta v})}_{\beta_{IFF,i}}.
\end{aligned}
\tag{6.8}
$$

with angular rotor position ϑ_i and the overlined factors indicating the above determined mean differential pitch amplitudes. It represents a control schema based on the variable wind field parameters and the current rotor position.

The signal flow chart in Figure 6-7 shows that the compensation is based on the reconstructed wind field parameters, which can be calculated a priori, but also needs the current rotor blade azimuth positions of the tree blades, which are states of the turbine model during the simulation. Since $\beta_{IFF,i}$ does not influence the rotor speed and position, the use of ϑ_i cannot be regarded as a feedback loop. The collective part β_{CFF} influences the rotor speed. However, it does not depend on any of the turbine state variables, and as a feedforward control thereby does not change the stability of the control loop.

However, online calculations during runtime of the simulation turn out to slow down the simulation significantly. To accelerate the computational simulations by preparing the feedforward strategy, the individual compensating feedforward pitch angles are calculated for a set of possible rotor azimuth angles in the range $[0 \ldots 2\pi]$ and stored, in a lookup table for all time steps (rows) and the rotor angles (columns). Per each wind field and lidar simulation configuration, one lookup table can a priori be calculated. The table is loaded before a simulation by a developed DLL file and the three feedforward pitch angles are interpolated during runtime of the wind turbine simulation per each time step.
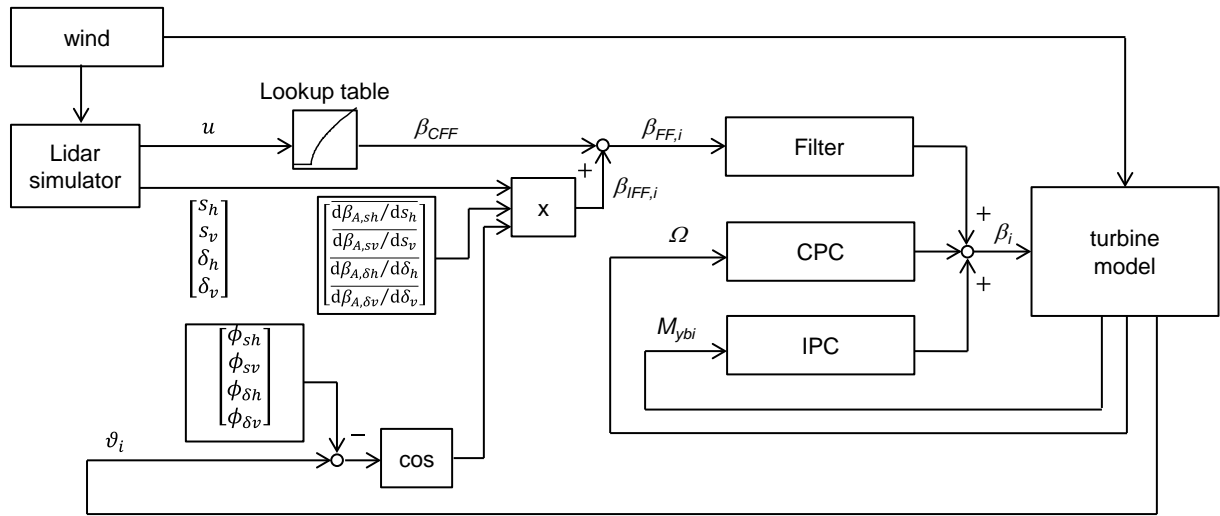
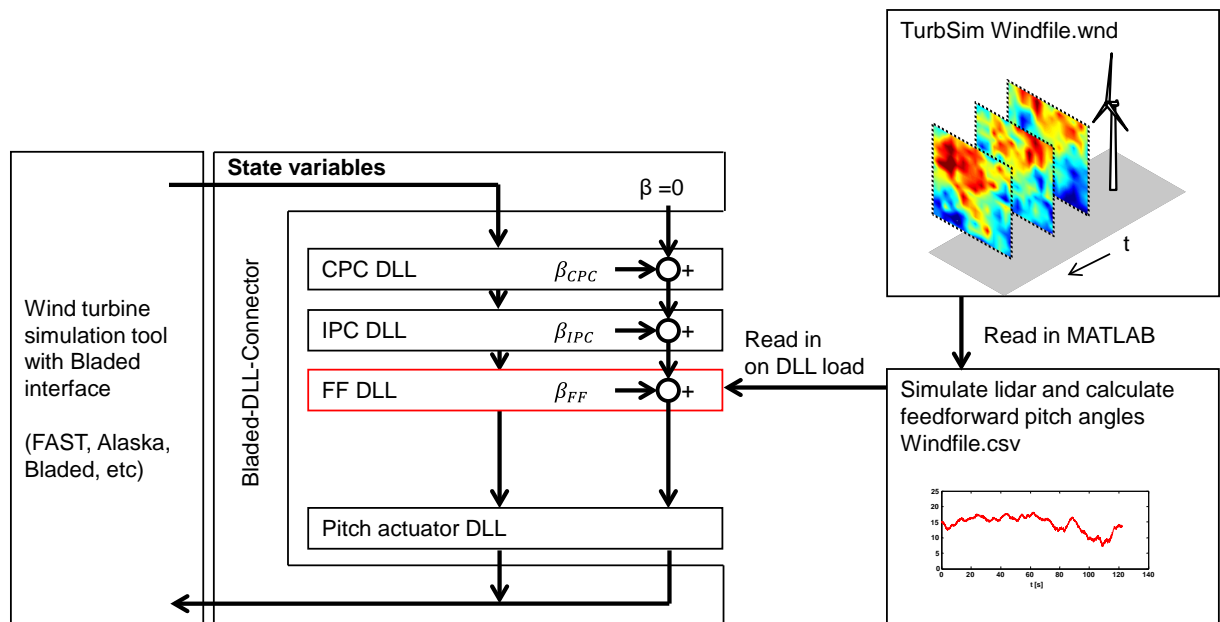*Figure 6-7: Signal flow chart of the static feedforward compensation*

Figure 6-8: Simulation setup of IFF pitch control with universal BLADED style DLLs

6.1.6 Filtering of Feedforward Pitch Signals

When using the static approach described in the previous section, turbulent fluctuations over a wide frequency range can be found in the pitch signals. However, fluctuations at higher frequencies should be avoided for two reasons: First, possible unpredictable turbulence effects discussed in Subsection 6.1.2 need to be filtered out to avoid wrong pitch action. Secondly, higher frequent parts of the calculated pitch signal can have a negative effect on the aimed load reductions, because in a realistic turbulent operation the turbine generally behaves slightly differently than in the stationary simulation used for pitch angle calculation.

Accordingly, it is one task during the design of a feedforward control strategy to construct an appropriate low pass filter. Its basic parameters are the filter type, filter order and cut-off frequency. Besides other approaches, e.g. based on the determination of the response characteristics, here, the input-output characteristics of the integrated system consisting of pitch actuation as input and fatigue load reduction as output is considered.

In a preparing simulation study of the integrated system a forward-backward filter strategy is used to study the influence of the cut-off frequency f_c whilst neglecting the influence of phase delays. By applying the load analysis method described later in this chapter it can be found that decreasing cut-off frequencies lead to decreasing loads for all numbers of scanned points per wind field per second. At least this is valid down to a cut-off frequency of 0.025 Hz for the simulated turbine, see the description and Figures in Appendix B.3. At these very slowly changing signals, even few scanned points are sufficient for significant load reductions. When applying feedforward pitch signal filters with higher cut-off frequencies, the averaging effect of a higher number of scan points is essential for gaining a benefit from feedforward pitch control.

However, in the practical online implementation of a forward filter, its delay has to be considered. Filters with low cut-off frequencies have large delays and can only be used if sufficient preview time τ_{pre} of the lidar system is available.

It is advantageous to introduce the group delay $\tau_g(\omega)$ of a filter defined as

$$\tau_g(\omega) = -\frac{d\phi(\omega)}{d\omega} \tag{6.9}$$

where $\phi(\omega)$ denotes the phase response depending on frequency ω.

The group delay can be interpreted as the shift of a "group" of frequencies in the time domain. The group delay tends to increase with decreasing cut-off frequency.

A constraint can now be introduced, stating that the allowable group delay $\tau_g(\omega)$ must not exceed the preview time $\tau_{\mathrm{pre}}(d_x, \overline{U})$ plus additional computational time τ_{comp}

$$\tau_g(\omega) < \tau_{\mathrm{pre}}(d_x, \overline{U}) + \tau_{\mathrm{comp}} \quad \forall \, \omega. \tag{6.10}$$

In the following simulations the additional computational time is neglected because usually $\tau_{\mathrm{pre}} \gg \tau_{\mathrm{comp}}$.

In Figure 6-9 the group delay together with the spectral filter magnitude is compared for an infinite impulse response (IIR) filter of first order, a finite impulse response (FIR) filter of fourth order with Kaiser windows and an FIR filter of eighth order with Gaussian windows. All three filters are designed to fulfil the specification of 3 dB damping at cut-off frequency, which is often used in filter design processes. According to the comparison the lowest group delays, which are aimed for the discussed control purposes, are achieved by low order IIR filters. In the given example the Butterworth IIR filter of first order is preferable. Other IIR filters like Chebyshev Type I/II or Elliptic filters of low order are possible and give equal or similar results.

Practical differences in the design, implementation and application can for example be found in [95] or [96]. The main disadvantage of IIR filters being the complex practical implementation can be considered of lower relevance in wind energy applications due to low computational restrictions.
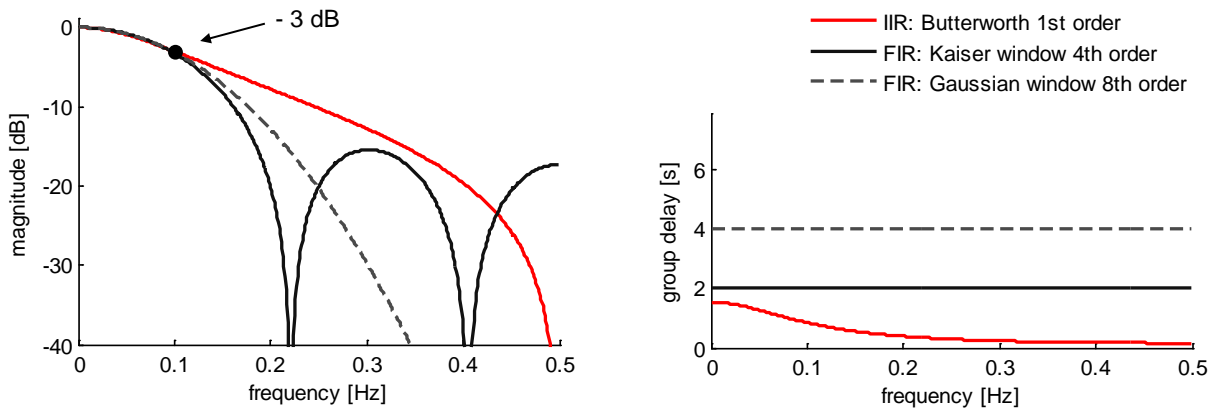
Figure 6-9: Magnitude and group delay of IIR and FIR filters designed for an attenuation of 3 dB at cut-off frequency 0.1 Hz. FIR filters need higher orders to meet the given specification, resulting in higher group delays. IIR filters of low order, for example the chosen Butterworth filter, have low group delays, which is favourable for feedforward pitch control applications.

Exemplarily, the group delay of a Butterworth filter is calculated and used in the developed simulation environment.

The transfer function of an order $n = 1$ Butterworth filter is given by

$$
\begin{aligned}
H(s) &= \frac{G_0}{\prod_{k=1}^{n} \dfrac{s - s_k}{\omega_c}} \\
&= \frac{G_0}{s/\omega_c + 1}.
\end{aligned}
$$

(6.11)

The phase $\phi(\omega)$ is defined as

$$
\begin{aligned}
\phi(\omega) &= \arg\{H(j\omega)\} \\
&= \arctan\left(\frac{\mathrm{Im}\{H(j\omega)\}}{\mathrm{Re}\{H(j\omega)\}}\right)
\end{aligned}
$$

(6.12)

and hence for transfer function (6.11)

$$
= \arctan\left(\frac{-\omega}{\omega_c}\right)
$$

(6.13)

According to (6.9) the group delay at $\omega = 0$ becomes

$$
\begin{aligned}
\tau_g(0)|_{n=1} &= -\left[\frac{d\phi(\omega)}{d\omega}\right]_{\omega=0} \\
&= \left[\frac{\omega_c}{\omega_c^2 + \omega^2}\right]_{\omega=0} \\
&= \frac{1}{\omega_c}
\end{aligned}
$$

(6.14)

Analogously, the group delay for the filters of second and third orders are

$$
\begin{aligned}
\tau_g(0)|_{n=2} &= \sqrt{2}^{1} \cdot \frac{1}{\omega_c}, \\
\tau_g(0)|_{n=3} &= \sqrt{2}^{2} \cdot \frac{1}{\omega_c}.
\end{aligned}
$$

(6.15)

Thus, the necessary preview time decreases inversely with cut-off frequency, or in other words, the minimum possible cut-off frequency decreases inversely with increasing preview time. This relation is illustrated in Figure 6-10. The preview time τ_{pre} is replaced by the measurement distance d using the linear approximation of Taylor's hypothesis

$$
d = \overline{U} \cdot \tau_{\mathrm{pre}}.
$$

(6.16)

The minimum cut-off frequency increases for filters of higher order by the factors given in Equations (6.15).

As described in Subsection 3.1.2, with increasing separation distance, the linear correlation of wind speed fluctuations disappears due to turbulence effects. The

upper frequency limits found in Subsection 3.1.2 can now be used here to design a low pass filter for the uncorrelated fluctuations.

Finally, a region can be identified where a low order IIR filter is realizable and at the same time the necessary low pass filter specifications due to wind evolution are fulfilled. Such an area is exemplarily given for mean wind speeds of 16 and 24 meters per second and filter (6.11) in Figure 6-10 c) and d).
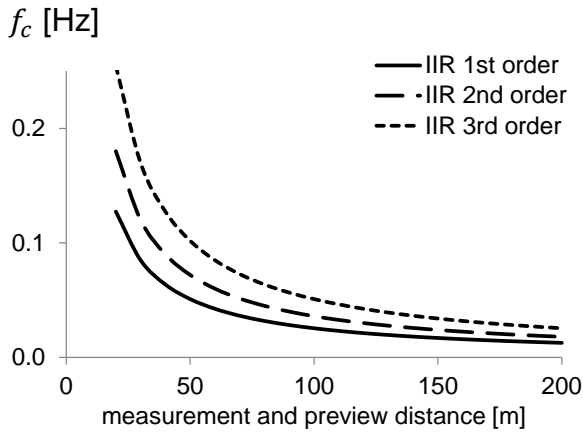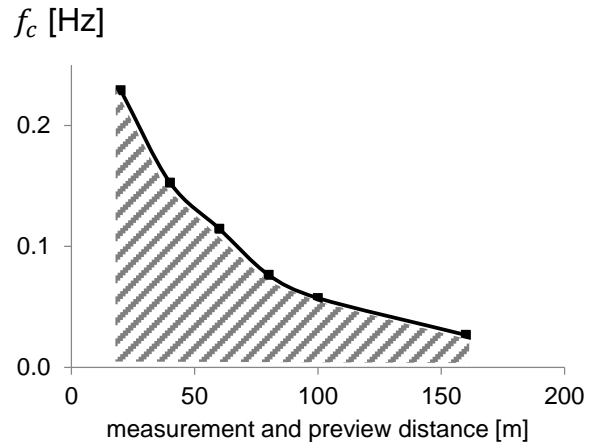

Figure 6-10: Possible filter cut-off frequencies

a): Minimum realizable filter cut-off frequencies of a Butterworth filter of first, second and third order. The limit represents equality of filter group delay and preview time based on mean wind speed $\overline{U}$ =16 m/s.

b): Maximal necessary filter cut-off frequencies for suppression of uncorrelated fluctuations at mean wind speed $\overline{U}$ =16 m/s.
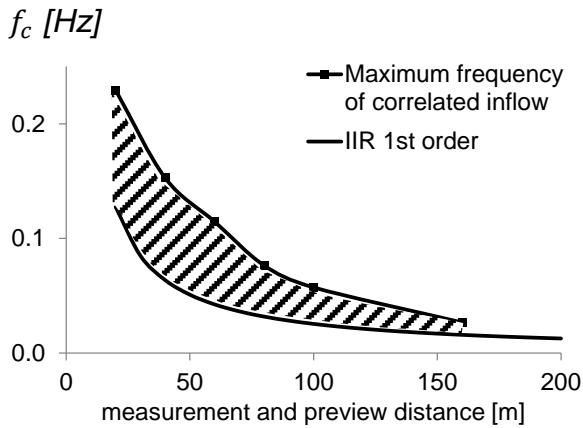
c): Region of realizable and necessary filter cut-off frequencies, lower limit represented by IIR filter of first order at mean wind speed $\overline{U}$ = 16 m/s.
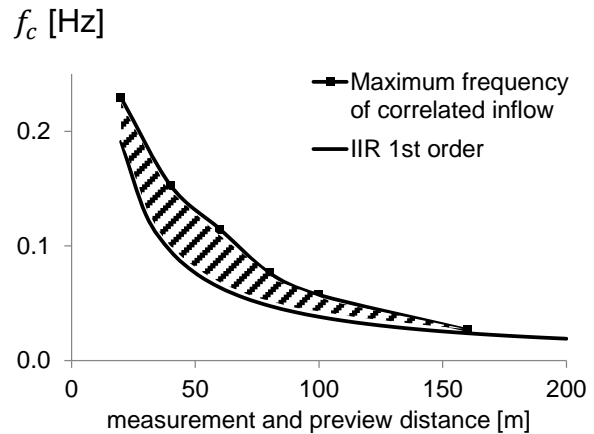
d): Analog Figure 6-10 c), but at mean wind speed $\overline{U}$ = 24 m/s.

Note that a lower deviation than the lower bound is inherently not possible, whereas the exceedance of the upper bound is possible but results in undesired noisy signals.

As a result, a mean wind speed dependent adaptive filter is created based on the presented limitations with the specifications listed in Table 6-3.

In case of CFF pitch control, the filter is applied to the calculated rotor averaged wind speed, or in case of the static compensation, to the calculated pitch angles.

For IFF pitch control the filter is applied to the calculated pitch angles per fixed rotor position, which means that the pitch angle variation at a given position on the fixed rotor disc is limited in the dynamics, typically to below 1P. However, the individual pitch angles follow their sinusoidal behaviour during one revolution.

Table 6-3: Cut-off frequencies of an adaptive filter

mean wind speed $\bar{U}$	allowable delay at $x_{\text{focus}} = 60$ m	filter group delay $\tau_g(0)$	chosen cut-off frequency f_c
[m/s]	[s]	[s]	[Hz]
2	30.00	5.88	0.027
4	15.00	5.88	0.027
6	10.00	5.88	0.027
8	7.50	5.88	0.027
10	6.00	5.88	0.027
12	5.00	4.96	0.032
14	4.29	4.28	0.037
16	3.75	3.77	0.042
18	3.33	3.29	0.048
20	3.00	3.03	0.052
22	2.73	2.71	0.058
24	2.50	2.49	0.063

The cut-off frequencies are constructed so that the group delay equals the allowable delay, or the lowest reasonable cut-off frequency is reached.

In contrast to the offline forward-backward filter of Subsection 6.1.2 (wind evolution simulation) a causal filter was designed, i.e. a filter with the output only depending on past and present inputs, so that the filter can be transferred to real applications.

6.1.7 Feedback Controllers

The power limiting collective pitch controller (CPC) and the 2P load alleviating individual pitch controller (IPC) developed by Hess and Seyboth [97] have been used for the presented simulations.

Both feedback control loops are designed according to the model based H-infinity approach to achieve high adaptability to different turbine models and guaranteed stability and performance. The tested and optimized collective pitch controller limits the generator output using the rotor speed as input. In addition to that, the 2P individual pitch controller uses blade root bending moment signals as well as tower acceleration measurements to mitigate loads in the 1P and 2P frequency domain. Controller descriptions and performance analyses can be found in [97].

An additional third experimental feedback controller is included in parts of the analysis to demonstrate the effect of reactive tower damping (TwD) by pitch control based on feeding back tower acceleration signals. Whereas IPC focusses on decreasing asymmetric loads on the rotor and tower side-to-side motions, a tower damping controller offers the possibility to mitigate symmetric loads in wind direction (tower fore-aft damping) and on the rotor shaft torque.

Feedforward control in principle is capable of assisting the aforementioned variants of feedback controllers. Particularly in the proposed independent add-on configuration it is easy to add and also to smoothly fade in and out.

6.2 Feedforward Pitch Control Simulation Results

The performance of a pitch controller is usually evaluated by comparing resulting loads on components of the wind turbine, the pitch activity and the power output for different control schemes. Here, a set of combinations of feedback and feedforward control methods is compared, with varying lidar measurement chain configurations. The base configuration is presented in Table 6-4. These parameters represent a realistic lidar measurement chain scenario taking into consideration current lidar technology.

Table 6-4: Lidar measurement chain parameterization

Wind evolution	forward/backward Butterworth low pass filter, 2nd order, wind speed adaptive
Scan	circular, 32 equiangular focus points
Focus length	71.0 m
Half cone opening angle	32.3°
Lidar wind field sampling	1 Hz
Volume averaging	$w_{\mathrm{norm,min}} = 0.1$ (see Section 6.1.3)
Reconstruction	three parameter estimation (u_0, s_h, s_v)
Feedforward pitch control	static collective and static 1P individual compensation and online lookup table interpolation
Feedforward pitch filter	causal Butterworth low pass filter, 1st order, wind speed adaptive azimuth-fixed filter of FF pitch angle time series

As a first indication of load reduction potentials, the fast Fourier transform (FFT) of the blade root bending moment is analysed for the turbulent wind conditions of 16 meters per second mean wind speed and 0° average horizontal and vertical wind direction Three configurations are compared: Baseline collective pitch control (CPC), additional 2P individual feedback pitch control (IPC) and additional collective (CFF) and individual (IFF) feedforward control based on the simulated measurements.

The amplitude spectra of the FFT are given in Figure 6-11. As it was designed for, IPC substantially reduces 1P and 2P load amplitudes. Around those frequencies, only marginal potential remains for additional reductions by feedforward controllers.

The benefits of feedforward control emerge at low frequencies, when the blades are predictively and precisely adjusted to the desired pitch angles. Conventional control based on the measured rotor speed signal provides correct angles only in stationary conditions. However the drive train inertia leads to a delayed response at the measured rotor speed. Up to a certain low frequency, in this example up to 0.2 Hz, collective feedforward control can therefore significantly reduce the blade load amplitudes.
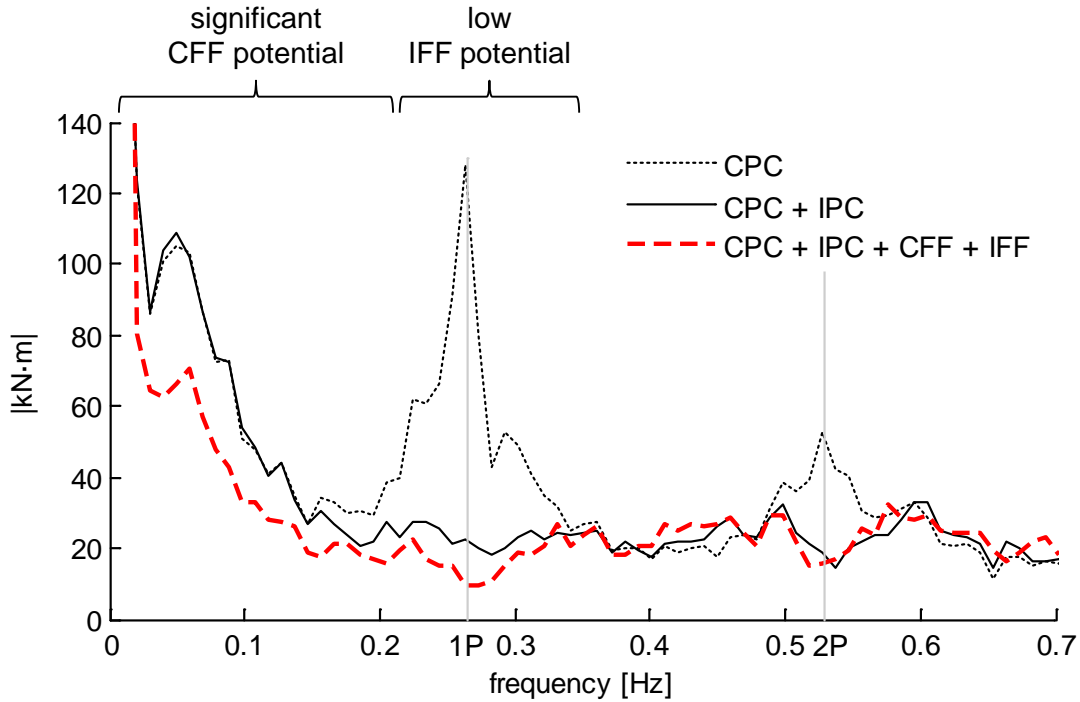
Figure 6-11: Amplitude spectrum of the FFT of the blade root bending moment M_{yb}.
Dotted: State of the art collective pitch control based on rotor speed.
Solid: Feedback individual pitch control to mitigate 1P- and 2P-loads based on measurements of the blade root bending moment.
Dashed: Feedforward + feedback individual pitch control based on perfect inflow measurements.
Vertical dotted: 1P and 2P frequencies

In the next section these potentials are quantified by the calculation of damage equivalent loads (DEL).

6.2.1 Fatigue Loads

Fatigue load calculation aims at predicting the lifetime of structural components and is often used in the performance evaluation of load reducing wind turbine control algorithms. E.g. Haibach published a comprehensive and systematic discussion [98]. Hereby fatigue is seen as a process of cyclic loading and damaging of the material and is statistically valid for a large number of components.

To determine damage equivalent loads from the simulated load time series, first stress cycles are counted according to the Rainflow-counting algorithm and sorted in stress amplitude classes and wind speed classes. The counted number of amplitudes are weighted by a Rayleigh distribution of the wind speeds at a given location. Here, the Rayleigh distribution with scale parameter $\sigma = 8.5 \cdot \sqrt{2/\pi}$ for the mean wind speed of 8.5 meters per second is used.

The measured or simulated load cycles usually are an excerpt of the life time damage seen by the component. Therefore the weighted numbers of amplitudes per stress class have to be extrapolated to the life time of for example 20 years.

The so obtained number of amplitudes n_i per stress class $S_{a,i}$ are then related to the number N_i of maximum endurable load cycles of amplitude $S_{a,i}$ of a specific material.

The relation of N and S_a can experimentally be determined for different materials by applying sinusoidal stress. Regarding fatigue loads, usually with increasing N smaller amplitudes S_a are possible. This relation often is linear in the double-logarithmic S-N or Wöhler curve and described by the Wöhler exponent k, which is e.g. for steal $k = 4$ and for glass-reinforced plastic (GRP) commonly used in the blades $k = 10$.

While the damage as the relation of n_i and N_i does not contain information about the loads, the (theoretical) amplitude of an equivalent sinusoidal load $S_{a,\text{eq}}$ – the damage equivalent load (DEL) – causing this same damage can be calculated for a given number of load cycles. It can be shown that the actual S-N-curve is not needed and the Wöhler exponent is sufficient to describe the material.

As load cases, the 60 wind conditions defined by the parameters according to Table 6-2 and compliant with the normal turbulence model (NTM) of the current IEC standard [92] are chosen.

Fatigue load reduction potentials are presented as relative changes in DEL, compared to the absolute DEL of CPC simulations, and using the feedforward parameters given in Table 6-4.

Three important load signals are regarded:

1. Flapwise blade root bending moments M_{yb}: The blades experience wind loads at the very front and the root bending moments often determine the blade design.

2. The variations of the rotor shaft torque M_{xs} do not only determine the design of the shaft, but also influence the whole drive train design like gear box and generator sizing.

3. The fore-aft tower base bending moment M_{yt} determines the tower and foundation dimensions. Both represent a large fraction of the total invest of a wind turbine, for example around 28% for a typical onshore utility scale 2.0-2.5 MW wind turbine installed over flat terrain, according to [99].

In Figure 6-12 the results of the simulations and load calculation for the three signals are summarized and grouped by three feedback control setups: CPC (left), CPC and IPC (middle) and CPC, IPC and TwD (right). Collective (CFF) and individual (IFF) lidar based feedforward control are compared in each group respectively.
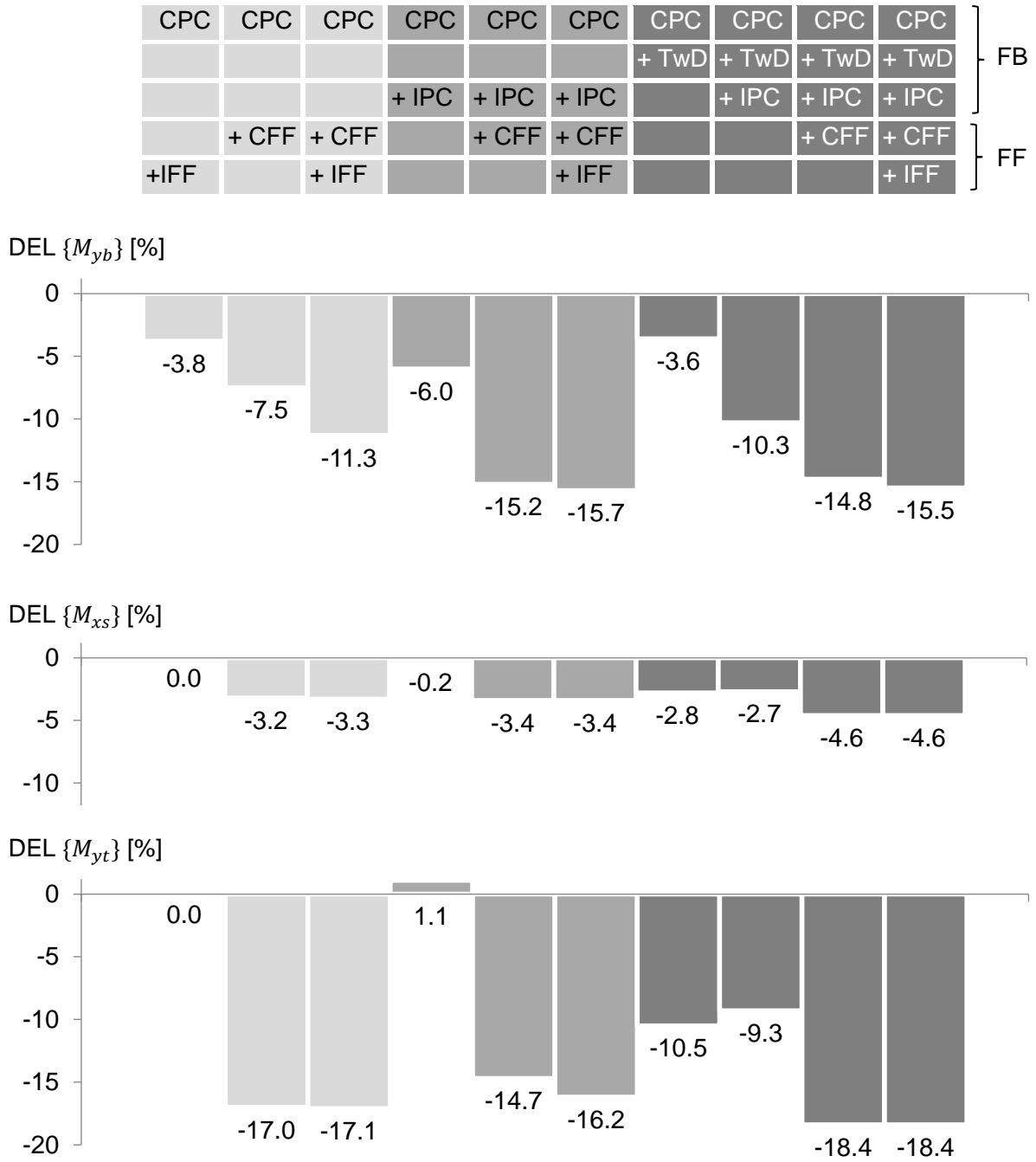
CPC	CPC	CPC	CPC	CPC	CPC	CPC	CPC	CPC	CPC	
						+ TwD	+ TwD	+ TwD	+ TwD	FB
			+ IPC	+ IPC	+ IPC		+ IPC	+ IPC	+ IPC	
	+ CFF	+ CFF		+ CFF	+ CFF			+ CFF	+ CFF	FF
+IFF		+ IFF			+ IFF				+ IFF	

DEL $\{M_{yb}\}$ [%]

DEL $\{M_{xs}\}$ [%]

DEL $\{M_{yt}\}$ [%]

Figure 6-12: Change in DEL of the flapwise blade root bending moment M_{yb}, shaft torque M_{xs} and tower base moment M_{yt} w.r.t. CPC for different pitch control setups comprising feedback (CPC, IPC, TwD) and feedforward (CFF, IFF) control strategies.

Collective feedforward pitch control offers, according to the simulation results, a significant load reduction potential when compared to any of the considered feedback controllers and for each load signal respectively. The blade root bending moment benefits by 4.5 to 9.2 percentage points (pp), the shaft moment by 2.9 pp in average, the tower base bending moment by 9.1 to 17 pp. Particularly, CFF can be regarded as a well suited supplement to IPC, by improving blade root load reduction and complementing rotor shaft and tower load reduction. The conclusion of the spectral

analysis of Figure 6-11 valid only for a mean wind speed of 16 meters per second and the assumption of perfect measurements qualitatively holds also for the lifetime fatigue. Tower feedback pitch control has to be seen as a competitive technology to CFF, because low frequent collective pitch is applied in both cases while reducing similar load channel sets. Here, CFF (+IPC) (column 5) exceeds the TwD (+IPC) (column 8) reduction potentials by 4.9, 0.7 and 5.4 pp. These values will vary for different lidar configurations or TwD implementations, but the basic CFF advantage of preview time τ_{pre} for filter applications will remain. Because the low frequent "collective" load fluctuations are unpredictable – in contrast to 1P loads – no feedback control strategy, like TwD, should reach the effectivity of well-engineered CFF designs.

Individual feedforward pitch control can reduce the damage equivalent loads of the flapwise blade root bending moment. As an alternative to an inoperative or unavailable IPC, IFF (column 1) reduces the considered blade loads by 3.8%, compared to 6.0% of IPC (column 4). As an enhancement to CFF, IFF reduces the blade loads even further by 11.3% (column 3).

In contrast, IFF can be regarded redundant if IPC is already implemented and in operation. Then, the additional load reductions of IFF only amount to 0.2, 0.0 and 1.5 pp (column 6) for the three load signals compared to IPC + CFF (column 5), and to 0.7, 0.0 and 0.0 pp compared to TwD + IPC + CFF (columns 10 and 9, respectively). This minor potential can be explained by two reasons: First, IPC already mitigates 1P loads fast and filter time demand is not an issue, because frequencies are higher and periodically, implying predictability. Second, IPC reduces periodic loads more precisely than the implemented feedforward strategy does. This is due to the fact that upwind lidar measurements are able to produce wind shear compensating pitch action only, while blade load feedback incorporates any other loads, including the dominating tower effect.

However, IFF can reduce Solely, as an alternative to IPC allowing 6.0 pp, IFF can reduce blade loads by 3.8 pp.

6.2.2 Extreme Operating Loads

Extreme operating loads have to be considered in the design process of wind turbines. In the IEC [92] design load cases are listed consisting of operation modes (e. g. start up, power production, parked), wind conditions (e. g. NTM or deterministic gust) and other conditions (e. g. system faults). The resulting overall extreme operating loads are obtained by the analysis of all the load cases and the application of safety factors.

Here, the extreme values of the fore-aft blade root bending moment during load cases based on the simulations with NTM wind conditions of Subsection 6.2.1 are analysed exemplarily. The absolute values of the (positive) maximum bending moments (in wind direction) are higher by a factor of approximately 2 than the absolute values of the (negative) minimum bending moments.

Naturally, the results cannot be transferred to other load cases.

Figure 6-13 presents the blade root bending moment reductions of the maximum values, again compared to baseline CPC, and for the three feedback control setup groups CPC only, CPC + IPC and additional TwD.
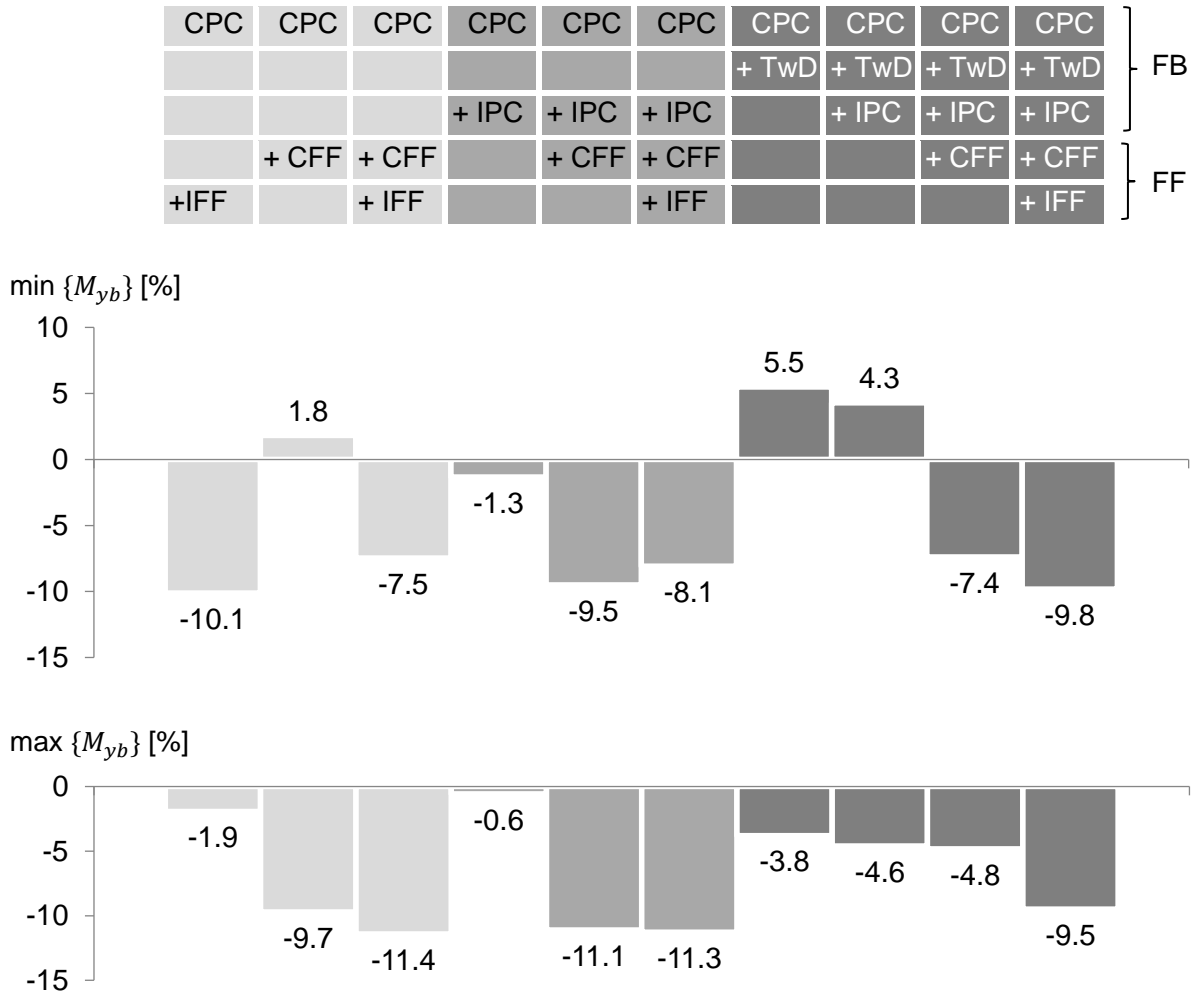
CPC	CPC	CPC	CPC	CPC	CPC	CPC	CPC	CPC	CPC	
						+ TwD	+ TwD	+ TwD	+ TwD	FB
			+ IPC	+ IPC	+ IPC		+ IPC	+ IPC	+ IPC	
	+ CFF	+ CFF		+ CFF	+ CFF			+ CFF	+ CFF	FF
+IFF		+ IFF			+ IFF				+ IFF	

min $\{M_{yb}\}$ [%]

max $\{M_{yb}\}$ [%]

Figure 6-13: Change in extreme loads of the blade root bending moment M_{yb} during regular operation w.r.t. CPC for the different pitch control setups.

CFF is able to decrease the considered extreme loads in different controller configurations up to 11.1%, but not all extreme loads are necessarily reduced. For instance, the extreme minimum blade 1 root bending moment in the CPC + CFF configuration is reached at one instance during passing of the tower shadow. Collective feedforward control even slightly deteriorates this particular load situation by 1.8%. In contrast, whenever feedback based IPC is applied, which is monitoring and directly controlling individual blade loads, additional CFF control reduces extreme loads by up to 10.5 pp. CFF can therefore again be regarded as a suitable supplement to IPC.

IFF is of minor effectivity in most of the simulated cases, except for the exclusive add-on to CPC due to the same reasons as for the fatigue loads in Section 6.2.1. As above, extreme load reduction cannot be guaranteed if no individual feedback pitch control is applied.

6.2.3 Pitch Activity

The presented control methods also influence the activity of the pitch drives, since the three blade pitch angles are the manipulated variables in the control loop. High pitch activity is undesirable due to the potential higher wear, energy consumption or need for larger or more robust pitch drives.

Pitch activity rates are analysed in the considered simulation results and measured in averaged and Rayleight-weighted standard deviation of the actual value of the pitch angle, within the wind speed bins 10 to 24 m/s of active feedforward control.

Often, also the so-called pitch actuator duty cycle (ADC) is used. It considers the proportion of the maximum pitch rate averaged over the duration of the load simulation and possibly weighted with a wind speed distribution [100].
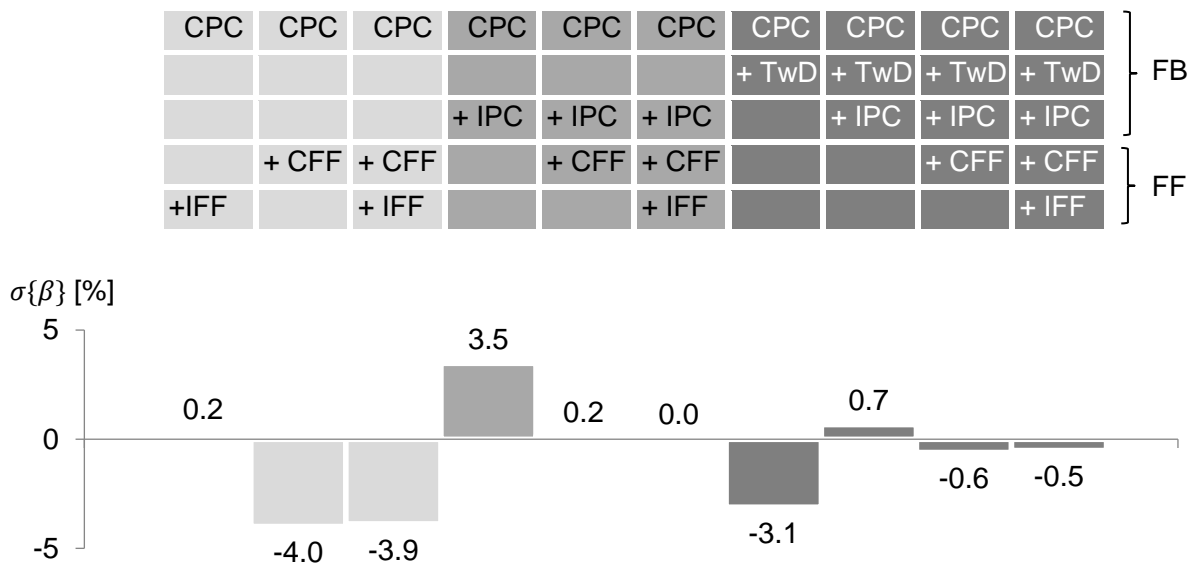

Figure 6-14: Change in the mean standard deviation of the blade pitch angle w.r.t. CPC for the different pitch control setups.

Adding collective feedforward pitch control, consistently the pitch variation is reduced. Compared to CPC, the pitch variation reduces by around 4% (column 2). Compared to CPC + IPC (column 4), the IPC induced increase in pitch activity is compensated with CFF (column 5). The pitch variation of TwD + IPC based control is only slightly influenced.

Individual feedforward pitch control do not demand the pitch drives more than CPC (column 1), but of course require the individual controllability of all three blades.

6.2.4 Generator Power

Besides load reductions, which are aimed applying feedforward control, and reduced pitch activity, which can be regarded as a welcome side effect, changes in the generator output have to be regarded. The generator output both is relevant in terms of the quality of the electrical power fed into the grid, and the amount of generated energy.

The electrical power output of the generator is analysed in terms of Rayleigh-weighted mean and standard deviation values in the feedforward operation region for wind speeds 10 to 24 m/s, where around half of the total yearly energy can be produced. The relative differences are shown in Figure 6-15.
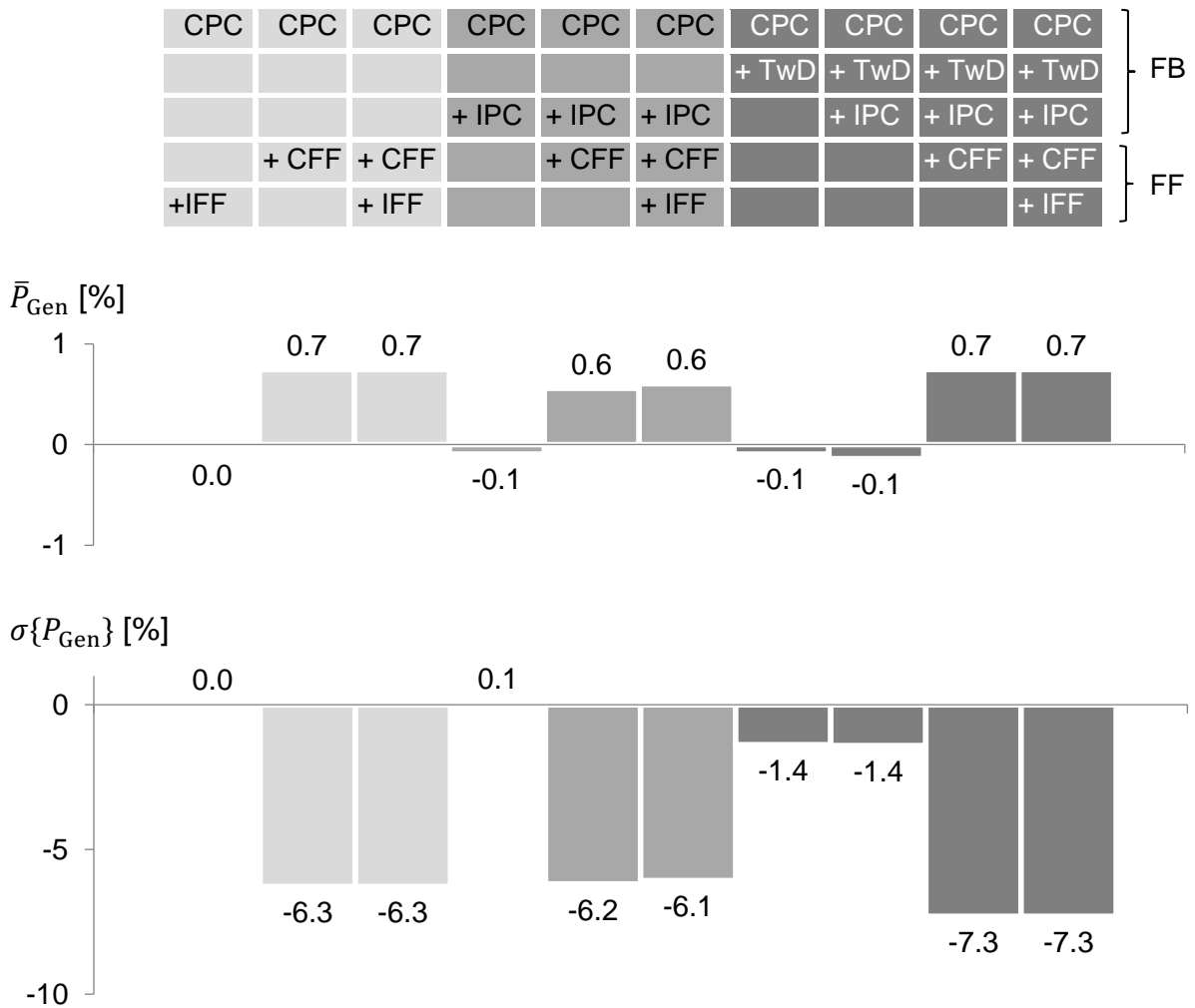

Figure 6-15: Change in the generator power output: mean (top) and standard deviation (bottom), w.r.t. CPC for the different pitch control setups.

Obviously, CFF slightly increases the electrical power output by 0.7% (around 0.3% annually) compared to all feedback strategies. From Figure 6-16 a) it can be argued that low frequent turbulent fluctuations in the transition region between 10 and 15 meters per second mean wind speed are more precisely tracked, or in other words, less energy is lost due to unnecessary pitch action.

In the full load operation region, moreover, power fluctuations are considerably reduced by 6.1 to 7.3%.

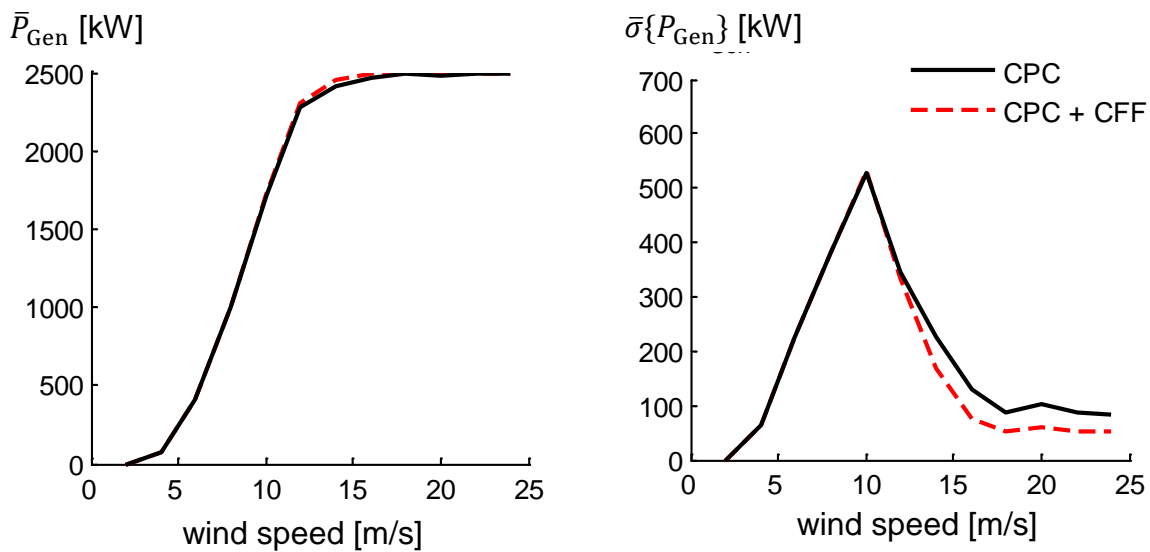IFF has no noticeable additional effect on the power output.

Figure 6-16: Generator power: mean (left) and standard deviation (right), per wind speed bin for conventional and feedforward enhanced collective pitch control

6.2.5 Sensitivity Analysis

Finally, a sensitivity analysis is carried out applying different configurations of the developed lidar simulation.

Table 6-5: Parameter variations for the sensitivity analysis

	Simulation parameter	Reference	Variations
1	Wind simulation	60 IEC wind files according to Table 6-2	-
2	Wind evolution	not modelled	filter according to Subsection 6.1.2 $x_{\text{focus}} = \{30, 60, 90\}$ m
3	Measurement		
3.1	Scan pattern	no scan[3]	n points in 1 s on a circle at 0.84 R $n = \{1, 2, ..., 10, 12, 16, 20, 24, 32\}$
3.2	Volume averaging	no averaging	$x_{\text{focus}} = \{30, 60, 90\}$ m
3.3	Measurement precision	no error	Normally distributed wind speed error in beam direction $v_{\text{LOS,i}} = v_{\text{LOS}} + \mathcal{N}\left(v_{\text{LOS,i}}, \sigma^2\right)$ $\sigma = \{0.1, 0.5\}$ m/s
4	Parameter reconstruction	direct calculation from wind files, rotor swept area[4]	3pe lin. according to Eq. (4.5)/ 3pe nonlin. according to Eq. (4.6)/ 5pe according to Eq. (4.28)+(4.29)
5	FF control		
5.1	Prediction time error	no error	$\tau_{\text{error}} = \{0, 0.5, 1, 2\}$ s
5.2	Azimuth angle error	no error	$\vartheta_{\text{error}} = \{0°, 10°, 45°, 90°\}$
6	Filter	noncausal Buttwerworth 2$^{\text{nd}}$ order $f_{\text{c}} = 0.2$ Hz	causal Butterworth 1$^{\text{st}}$ order wind speed adaptive according to Table 6-3

In Figure 6-17 the change in DEL reduction of the flapwise blade root bending moment in percentage points in the successive variation of the parameters listed in Table 6-6 is shown.

---

[3] When lidar parameters are varied, a reference scan of 32 points each on 5 circles between $r = 0.17\,R$ and $r = 0.84\,R$ each 1 second at the distance $x_{\text{focus}} = 60$ m is assumed.
[4] When lidar parameters are varied, the 3pe lin. is applied.
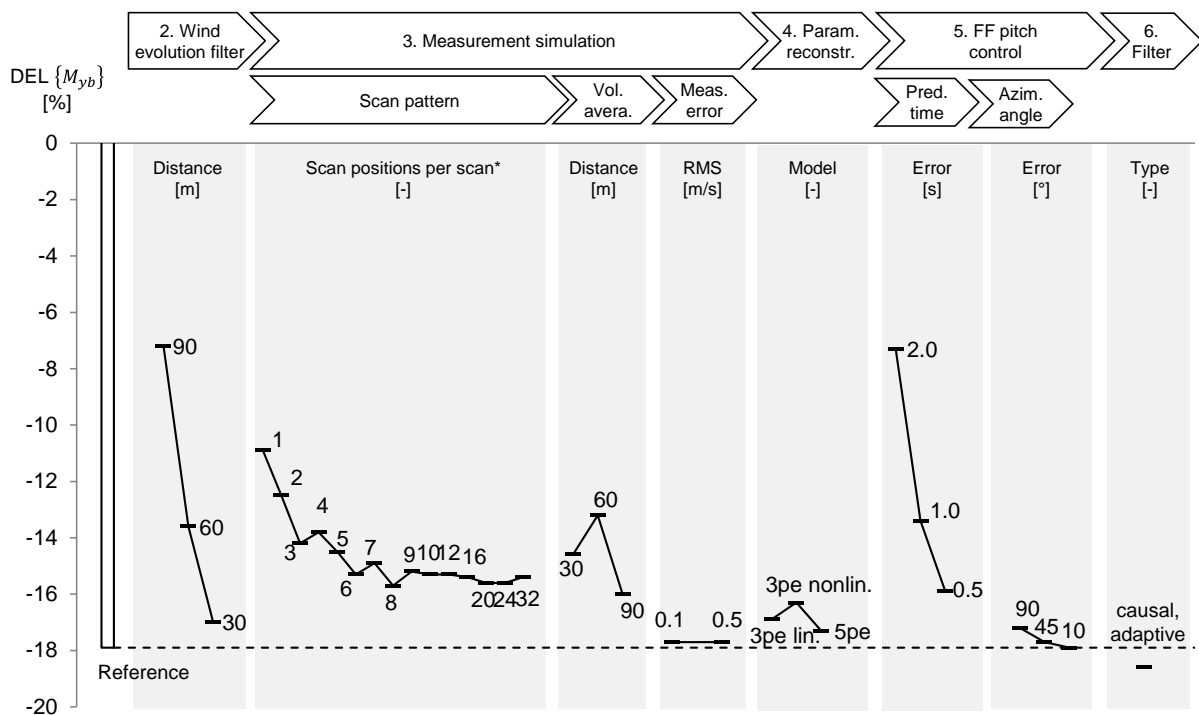
Figure 6-17: Sensitivity of feedforward fatigue load reduction w.r.t. conventional CPC of the blade root bending moment M_{yb} regarding different lidar setup parameters.
* In 60 m, but also with evolution filter and volume averaging.

Three parameters of major influence are:

1. Prediction time offset: A temporal misalignment of wind and measurement is introduced, resulting e.g. from inaccurate wind evolution prediction. The analysis reveals a distinct sensitivity on this parameter of around five percentage points per second.

2. Measurement distance: With increasing measurement distance the unusable information due to the turbulent wind evolution reduce the load reduction potential. The resulting sensitivity in the particular simulated setup is six percentage points per 30 meters.

3. Number of focus points: The more wind speed measurements are taken, here equiazimuthally on a circle and simultaneously per second, the more accurate wind field characteristics are calculated and the lower fatigue loads tend to result. For more than around eight points, no significant additional benefit can be gained from a higher sampling rate in terms of fatigue loads. The load reduction of these 15 cases do not reach the reference load reduction because the evolution filter and volume averaging were switched on here.

Naturally, load results of combined parameter variations cannot simply be derived by the addition of the effect of the given isolated changes. Usually, the decrease in load

reduction of a combination of variations tends to be less than the sum of the decreases of individual variations.

Minor influence is represented by the remaining three parameters:

1. Pitch phase offset: The application of individual feedforward pitch angles at an imagined erroneous azimuth angle (phase offset) occurs e.g. if the signal arrives too late or the azimuth sensor outputs wrong signals. Anyhow, the influence is negligible, because the effect of IFF itself is negligible, assuming IPC in standard configuration.

2. Wind field reconstruction: The three parameter nonlinear model (wind speed, vertical shear and horizontal direction), three parameter linear model (wind speed, horizontal and vertical shear) and five parameter nonlinear model are compared. The differences range below one percentage point. While the advantage of more accurate wind direction measurements of the 5pe method seems obvious regarding yaw control, pitch control is less influenced by inaccurate direction or shear signals and hence load reduction potential differences are small.

3. Lidar measurement error: Lidar measurement errors of 0.1 and 0.5 meters per second, defined by the root mean square of the error of the wind speed signal in beam direction, are introduced. The load reduction results are insignificantly deteriorated, so that the technical demand on lidar system is low for this specific parameter. This high tolerance is based on the lidar inherent volume averaging effect as well as on the averaging of a multiple point scan. For less scanned positions, the analysis should be repeated.

4. The developed causal wind speed adaptive filter does not reduce the load reduction compared to forward-backward filtering with fixed corner frequency.

6.3   Other Lidar Based Control Applications

Besides pitch control researchers have proposed further applications of turbine mounted lidars in the field on monitoring and control applications.

Recently, several approaches to dynamically monitor the performance of wind turbines have been made. The advantages of turbine mounted scanning lidars – fixed orientation towards the inflow and spatial averaging in beam direction and via scan patterns, make them attractive for dynamic power monitoring tasks.

In [101] and [102] it was demonstrated that dynamic power curves can be derived from this kind of data for short averaging times of e.g. 60 seconds. Consequently, the performance relative to the wind conditions can instantaneously be monitored, which has recently been evaluated in field tests [103], [104], [105].

In [106] a monitoring method based on the difference of the current power output and the current dynamic power curve (Langevin Power Curve, LPC) was proposed. Service periods were identified successfully.

An increased knowledge and tracking of the current wind conditions, e.g. by using the proposed five parameter model of Section 4.2, could potentially enable more advanced monitoring tasks.

In this section, two control applications, lidar based yaw control (Subsection 6.3.1) and lidar based generator torque control (Subsection 6.3.2) are discussed in brief. Conclusions regarding lidar based monitoring, pitch, yaw and generator control are summarized in Table 6-6 of Section 6.4.

6.3.1   Yaw Control

The yaw control system of a wind turbine is responsible for the accurate horizontal alignment of the rotor relative to the mean wind direction and contributes substantially to the overall performance. It influences the power production in partial load operation as well as the loads on main components of the wind turbine during operation and stand still.

In contrast to a conventional point measurement behind the rotor plane, in the configuration considered here, the yaw control system consists of a nacelle or spinner based lidar system, measuring upstream wind speeds and outputting averaged horizontal wind direction information, linked to a conventional yaw actuation mechanism. The accuracy of the horizontal direction information is studied here and compared for different lidar configurations and reconstruction methods.

The following steps are performed for all 60 full turbulent IEC wind model manifestations according to Table 6-2:

1. Simulation of n lidar measurements per wind field as described in Section 6.1.3, including the lidar's inherent volume averaging effect, resulting in n wind speeds in beam direction $v_L(x, y)$ at a given sampling rate f_s,

2. Reconstruction of the averaged horizontal wind direction $\delta_h(t_i)$ per time step t_i or equivalently per wind field using the three parameter (u_0, s_v, δ_h) and five parameter estimation methods (3pe, 5pe) of Sections 4.1.2 and 4.2.2, respectively.

3. Calculation of the actual ("real") wind direction $\delta_{h,act}(t_i)$ based on averages of the full wind information within the rotor swept area.

4. Segmentation and averaging of the resulting signals $\delta_{h,3pe}(t_i)$ and $\delta_{h,5pe}(t_i)$ and the actual direction $\delta_{h,act}(t_i)$ in blocks of length Δt_B,

5. Calculation of the mean of the absolute difference between block averaged reconstructed directions and the block averaged actual direction $\mathrm{abs}(\Delta\delta_h)$.

These mean values are a measure of the potential errors of a yaw control strategy using time averages of Δt_B based on the proposed lidar signals.
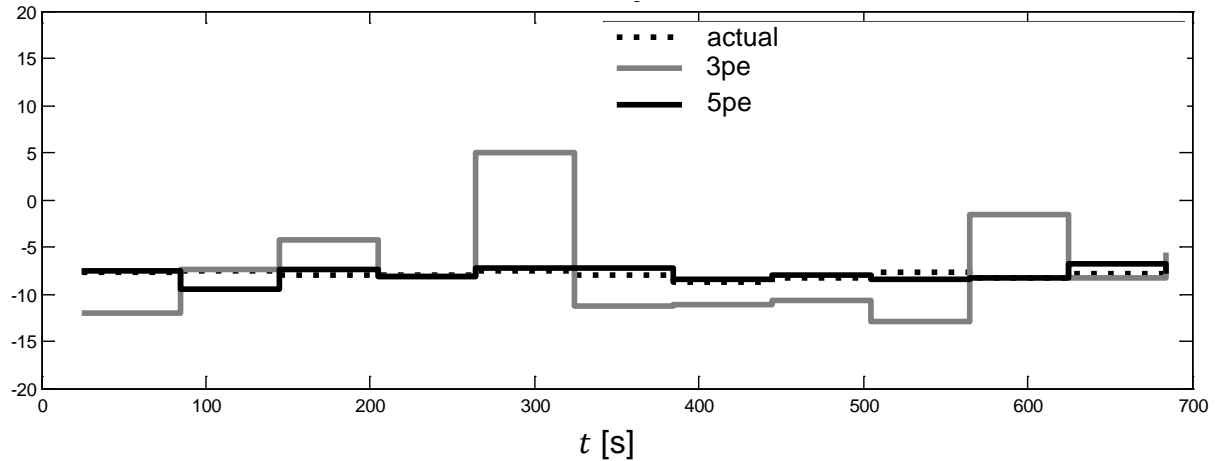
δ_h [°]

Figure 6-18: Reconstructed wind directions δ_h using the three and five parameter estimation method, plotted block averaged using Δt_B = 60 s, along with the actual wind direction derived from full wind information. The mean absolute errors are 3.6 degrees for the 3pe and 0.6 degrees for the 5pe method.

An example of the block averaged time series is given in Figure 6-18 for IEC wind conditions of 14 meters per second mean wind speed, -8 degrees horizontal and 0 degrees vertical mean wind direction. Obviously the direction estimation of the five parameter reconstruction method is much closer to the actual calculated wind direction of the numerical wind field. Unfortunately, as can be seen from the example, the IEC wind fields do not allow for the study of transient wind direction behaviour because the wind direction variation is too small.

In Figure 6-19 the estimation error ranges per wind bin are given for the two investigated methods, based on the mean absolute errors calculated for the different IEC simulations. Both the maximum and mean errors are lower for the five parameter method, and also the fluctuations are reduced, which was anticipated. In the operation region below rated wind speed, where the energy output can beneficially be influenced, the mean block-wise absolute errors range from around one to six degrees using the three parameter method, whereas the respective errors of the five parameter method do not exceed 1.3 degrees.

Because of the design of the IEC wind fields used here, turbulence intensity increases disproportionately to decreasing wind speeds [92]. Thus, at lower mean wind speeds, the turbulence within the wind field is relatively high. In Subsection 4.3.2 it was shown that higher ratios of random fluctuations and mean wind speed,

which was called conical turbulence intensity, leads to larger estimation errors of the 3pe method compared to the 5pe method.

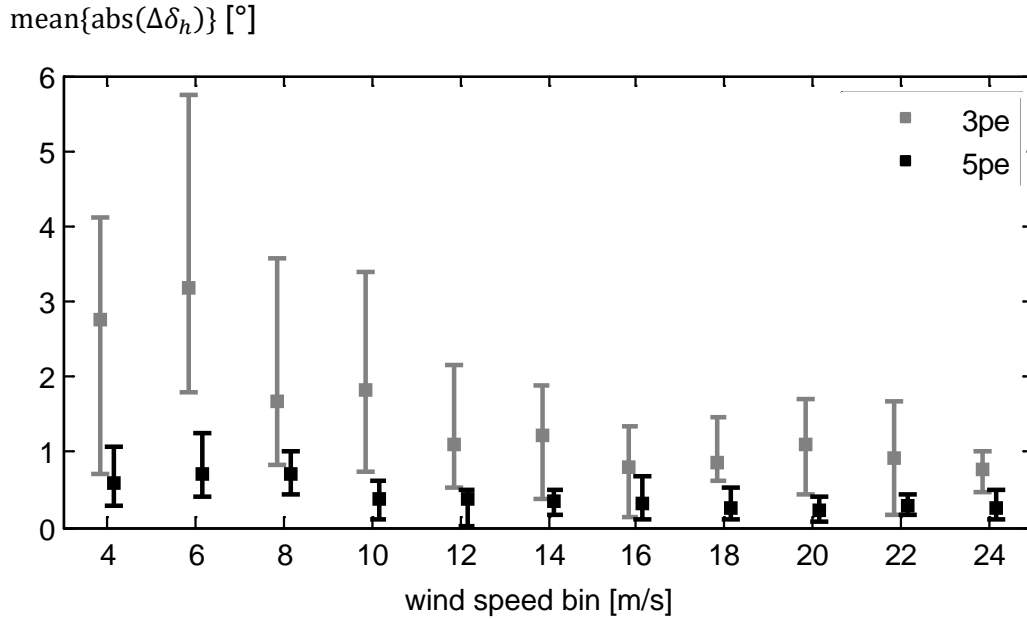$$\text{mean}\{\text{abs}(\Delta \delta_h)\} \ [°]$$

Figure 6-19: Errors in the direction estimation as a function of wind speed bins calculated for 60 IEC wind fields.
The error bars represent the minima and maxima of five simulations per bin.
The block-wise estimation error can be decreased by around 1 to 5 degrees in the partial load region applying
the 5pe method. Lidar measurements are simulated at 32 scan points and the reconstructed time series $\delta_h(t)$
are split in blocks of size 300s.
(The two bar groups are slightly separated in x-direction to improve readability.)

Further wind direction error estimations are given in Figure B.4-1 to Figure B.4-3 in the Appendix B.4, with varying numbers of scan points n and average block sizes Δt_B. The largest errors for both estimation methods in this calculation can be found for a small number of scan points and short averaging time segments, because limited spatial information evaluated over short time periods is affected most by spatial and temporal turbulence. In contrast, high resolution spatial scans combined with long averaging periods give lowest error rates.

In the region $8 \leq n \leq 32$ and $30 \leq t_B \leq 300$ the resulting errors can be seen in a more differentiated form. If the above effects do not dominate, the five parameter method estimates the direction more accurately for almost all simulated conditions, for instance of the order of five degrees for a wide range of wind speeds, see Figure B.4-3.

It can be concluded that for long averaging time intervals like 600 seconds, which can be considered close to current industry standard, and the use of a scanning lidar sensor with a number of scanned focus positions of the order of ten per second the mean errors do not exceed two degrees for both reconstruction methods. The easier to implement 3pe method using one focus distance only is preferable in these cases.

If a second measurement distance is employed at a high spatial resolution scan at for instance $n = 32$ positions, a lower error level of up to five degrees difference can be reached using the 5pe method. The effect on the power output can be estimated according to e.g. [107] by a factor of $cos(\delta_h)^3$. The annual energy production (AEP) of a wind turbine is commonly considered applying a power curve model and wind distribution assumptions [69]. An exemplary calculation for a five Megawatt offshore wind turbine model results in a difference in net energy extraction of the order of 0.2% between 5pe and 3pe (yaw hysteresis neglected).

Since the used IEC wind fields do not describe real wind changes sufficiently, the calculated benefits of the 5pe method are conservative. Especially in wind farms, as shown in Section 5.3.2, the 3pe method can be highly affected by misinterpretations of wakes. Then, the difference between 5pe and 3pe will be considerably larger due to larger 3pe errors.

Note that the total energy extraction potential using turbine lidars basically depends on the errors of existing wind vane based yaw control. Several studies present different potentials ranging from 0 to 10% AEP [107]. The power losses are strongly dependent on the specific turbine, the yaw measurement system and its calibration as well as the site location.

6.3.2 Generator Torque Control

Rotor speed is usually controlled at partial load operation, i.e. at below rated wind speed, by setting the generator torque based on rotor speed measurements. For each wind speed, there exists a dedicated tip speed ratio (tip speed of the blade divided by the free wind speed) for maximal energy extraction, and hence dedicated rotor speed and generator torque values. The control loop is relatively slow due to the inertia of the rotor and drive train.

The basic idea to improve generator torque control by making use of turbine lidar measurements is to predictively adjust the rotor speed and thereby to overcome the delay caused by the rotor and drive train inertia. In [70] it could be demonstrated in simulations that the optimal rotor speed can be tracked more precisely applying this approach. However, the fatigue loads on the shaft increased by around 9%, whereas the yearly energy output increased negligibly by less than 0.1%. The limited additional energy yield can be explained by the low dependency of the power coefficient of modern rotors on tip speed variations in the vicinity of the design tip speed ratio and the low level of tip speed variations due to slow rotor and wind speed variations.

6.4   Conclusions on Control Simulations

In Table 6-6 all control applications extensible with turbine lidar inflow measurements considered in this chapter are listed. The application's potential, the technical demand on a lidar sensing system and the method's maturity are assessed for each application.

The applications are ordered from large to small potential, while the technical demand tends to increase and the maturity tends to decrease.

First, it can be observed that performance monitoring is to be one of the first market-ready applications for turbine lidars, at least if lidar based power curve measurements become part of the certification procedure.

The high load reduction potential of lidar based collective pitch control could be confirmed in the simulations presented in this Chapter, so that after further field tests market introduction for large wind turbines can be expected if the sensitivities presented in Section 6.2.5 are realised in real lidar systems.

As a main result of this work, yaw control sets higher demands on the lidar system than often expected in the past. Many current systems lack the ability to measure from two independent horizontal directions, or in two consecutive distances as proposed in Section 4.2.2. Therefore, significant inaccuracies of the direction signal can occur as presented in the analysis in 5.3.2, especially in wind farm layouts, where usually the majority of wind turbines are located. Also, most comprehensive studies show minor need for persistent wind direction measurement improvements and low energy potentials. Consequently, the use for yaw control can be questioned.

Less potentially, lidar assisted individual feedforward pitch control will be of significance in future wind turbine designs, due to the presented superiority of reactive feedback individual pitch control. Lidar-IPC could possibly be applied as a – less powerful – alternative to feedback-IPC in cases a lidar system is to be installed anyway, e.g. as a monitoring solution. However, the demands on the lidar system are more stringent in terms of sampling, data acquisition, signal processing and system availability.

Table 6-6: Wind turbine applications of turbine mounted lidars

Application	Advantage	Potential	Technical Demand	Maturity
1 Performance Monitoring	dynamic power curve measurement	● esp. offshore	● low sampling and availability	● many field tests
2 Collective Pitch Control	decreased fatigue loads	● 5-10% DEL [3]	● low sampling and availability	◐ some field tests + publications
	decreased extreme loads	● 0-10% [3]	◐ low sampling, high availability	○ few publications
	increased energy output	◐ < 1 % AEP	● low sampling and availability	○ few publications
3 Yaw Control	increased energy output	◐ 0-10 % AEP	◐ two independent beam directions	◐ many field tests, but few reliable data
4 Individual Pitch Control	decreased fatigue loads	◐ 1-2% DEL [3,4]	◐ high spatial and temporal resolution	○ no field tests
	decreased extreme loads	○ < 1% [3,4]	○ high resolution and availability	○ few publications
5 Generator Torque Control	increased energy output	○ <0.1% AEP	◐ rotor average, temporal resolution	○ few field test

[3]: flapwise root bending moment   [4]: additional percentage points compared to traditional IPC

Assessment: ● positive, ◐ neutral, ○ negative

7 Conclusions and Outlook

In this thesis, new contributions to the increasingly popular topic of applications of turbine mounted lidars have been researched.

In general, it was observed in literature that lidar anemometry has been studied and tested mostly for site assessment applications, while lidar technology for turbine control applications is in a less mature state in terms of theory, testing and industrial applications. Therefore, existing challenges for systems based on lidar enhanced turbine control applications have been formulated in the introduction in three research objectives.

The first objective, the development of advanced methods to reconstruct wind field parameters for horizontal lidars, was approached in three steps: First, a five parameter wind field model was introduced to overcome existing limitations in the description of wind fields. Secondly, a reconstruction method was developed based on measurements in only one distance. It was found that only in very laminar inflow conditions the two similar effects of shear and direction on the measurements can be reconstructed uniquely. However, typically in wind energy applications more turbulent conditions dominate.

A possible solution was developed in a third step introducing a second measurement distance in upwind direction besides a fast and robust reconstruction algorithm. The new method combines measurements from two or more independent directions and offers a mathematically unique and stable solution for determining horizontal shear and direction. Analogously, also both vertical parameters can be determined, so that together with the averaged wind speed five relevant wind field parameters can be derived. In evaluation simulations without wake effects, the five parameter model is more accurate than existing three parameter models, e.g. of the order of five degrees lower root mean square direction errors in the considered IEC wind field sets.

However, test wind fields with more realistic wind direction changes are needed in further studies and could also extend the IEC wind fields. It can also be assumed that in wake situations the advantage of this method will be even more apparent.

As a possible realization of the measurements from independent directions, the refocussing to other focus points was assumed. However, this requires additional functionality which no fast scanning turbine mountable lidar was capable of until the end of 2013.

The second objective aims at improving the understanding of signals of turbine mounted lidar systems within a wind farm. A hub mounted spherical scanning lidar was successfully operated in a research consortium. Some analysis results have been presented in this thesis. A current data processing method was extended for horizontal lidars and applied to the experimental data. It was found that reflections from hard targets occur more frequently than in vertical applications and have to be filtered out to avoid measurement distortions.

A data availability analysis was performed, proving acceptable behaviour for most possible applications, with over 99.9% valid 1-Hz-data in a 170 hours period.

The high temporal and spatial resolution of the lidar enables new insights into turbulent wind conditions. Exemplarily, the inflow in upwind direction towards a neighbouring turbine was recorded and a clear area of wake induced low wind speeds could be found in parts of the visualized wind field. In another example, wind speed distributions very different from linear or exponential shear could be observed. This measurement method could be used for further analysis of typical wind conditions for which wind turbines should be designed to.

Moreover, the reconstructed wind direction in front of the experimental modern wind turbine within the wind farm was studied and it was confirmed that the direction signal is substantially affected by systematical errors. The errors are of sinusoidal shape with their maxima occurring around nacelle orientations towards the partial wake of upwind operating turbines. Averaged direction errors repeatedly reach 20 to 30 degrees in half wake orientations. They are almost independent of both the mean wind speed and the number of used measurement points between two and 200 per second distributed over an area of a disk. In these wake affected orientations, which can cover a large part of the turbine's operational time, conventional nacelle based non-remote wind direction sensors are more precise than the regarded lidar systems, even though the experimental lidar was the fastest scanning and sampling lidar available at that time.

The main reason for the inaccuracy was identified to originate from the misinterpretation of horizontal shear as horizontal direction due to the wake effects. The misinterpretation, in turn, finally results from the inherently similar effect of shear and direction on the limited information of the wind speed component measured in one laser beam direction only.

The third objective resulted in the development of a lidar measurement simulation chain with feedforward pitch control for a simulation environment for wind turbine models. All relevant characteristics such as scan geometry, volume averaging effect, wind evolution, parameter reconstruction, pitch angle calculation and signal filtering can be set up and varied. By that, the feedforward pitch angles can be calculated efficiently before the simulation. For simulations, a BLADED style DLL was developed which can easily be integrated or excluded in simulations with other controllers, e.g. conventional feedback controllers.

The advantage of the approach is that load reductions as an indication of the control performance can directly be regarded as a function of the lidar parameters. By that, extensive sets of simulations with varied parameters can be performed for comparison. The approach also includes a method to design causal wind speed adaptive low pass filters, based on experimental data and the available preview time.

The modularly extended simulation environment was used for the calculation of load reduction potentials applying different feedforward control strategies on a generic 2.5 MW wind turbine model with 90.37 m rotor diameter. In accordance with results from the literature, collective feedforward pitch control offers promising fatigue load reduction potentials for blade, shaft and tower bending moments, e.g. in the order of 9 to 17% DEL for the tower base. Besides, extreme operating loads decrease (5-11%), pitch activity is reduced (0-4%) and generator output can slightly be increased (<1%) with less variance (6%). The effects result from earlier reacting to turbulent inflow in the sub-1P-frequency range.

The addition of individual feedback blade pitch control seems especially promising since the advantages of both techniques complete each other: Collective feedforward pitch control can reduce loads below, and individual feedback around and above the 1P frequency.

In the simulations, individual feedforward pitch control could replace individual feedback control to a certain degree, depending on the lidar measurement chain setup. The requirements on the lidar system in terms of availability and reliability should be compared to the requirements on a strain sensor system for individual feedback pitch control carefully. However, as a supplement to individual feedback pitch control, individual feedforward control does not offer any additional advantage.

In a sensitivity analysis it is found that a possible prediction time offset of more than 0.5 seconds, measurement distances of more than around 90 meters and, thirdly, a number of measurement points less than 8 limit the load reduction potential.

In all three fields – measurement expertise, reconstruction theory and application design – further research and development activity can be anticipated. Currently, there is a lot of experimental testing activity ongoing and planned in the research and industrial sector. Next steps will regard the preparation of lidar designs and nacelle integration for series production, explicitly for monitoring and feedforward control enhancements.

One research issue will be the sufficiently correct and robust calculation of deterministic inflow effects, particularly the deceleration in the rotor induction zone, so that the correct timing of gust measurements and pitch action is ensured.

Reconstruction methods, especially for shear and direction estimations, will be given more relevance, since the current direction signals can be insufficient, as was demonstrated. The experimental testing of multi distance lidars for enhanced direction measurements is recommended.

Major research is also required in the field of data availability analyses for horizontal lidars. Longer studies on small timescales of around one Hertz sampling frequency are needed, and special focus should be given to strong precipitation, clouds and other environmental conditions.

Finally, more effort should be spent on the standardization of simulation scenarios for lidar based control. Varying wind fields in front of turbines and more realistic variant direction and shear behaviour, especially in wind farm configurations, should be implemented into standard test scenarios for wind turbine controllers, so that comparability between test setups as well as closeness to reality are improved.

Bibliography

[1] S. W. Thomson, "Presidential Address to Section A of the British Association for the Advancement of Science," 1881.

[2] The European Wind Energy Association, "Wind in power: 2013 European Statistics," 2013.

[3] Fraunhofer-Institut für Solare Energiesysteme (ISE), "Stromgestehungskosten Erneuerbarer Energien," 2013.

[4] DEWI GmbH, "Windenergienutzung in Deutschland," [Online]. Available: http://www.dewi.de/dewi/index.php?id=47&L=1. [Accessed 01 05 2013].

[5] Fraunhofer IWES, "Price Tendencies in the Wind Energy Market per kW installed Power," [Online]. Available: http://windmonitor.iwes.fraunhofer.de. [Accessed 01 05 2013].

[6] S. Krohn, P.-E. Morthorst and S. Awerbuch, "The Economics of Wind Energy," *Proc. European Wind Energy Conference & Exhibition, Marseille, France,* 2009.

[7] Google Inc., "Google Scholar," [Online]. Available: http://scholar.google.de/. [Accessed 07 05 2013].

[8] J. M. Vaughan and P. A. Forrester, "Laser Doppler Velocimetry Applied to the Measurement of Local and Global Wind," *Wind Engineering Vol. 13 No. 1,* 1989.

[9] F. Bingöl, J. Mann and D. Fousseki, "Conically scanning lidar error in complex terrain," *Meteorologische Zeitschrift Vol. 18, No. 2, 189-195,* 2009.

[10] J. M. Vaughan, K. O. Steinvall, C. Werner and P. H. Flamant, "Coherent Laser Radar in Europe," *Proc. IEEE, Vol. 84, No. 2,* 1996.

[11] S. Kapp, "Internal market survey," *Robert Bosch GmbH,* 2013.

[12] M. Harris, M. Hand and A. Wright, "Lidar for Turbine Control," *Technical Report NREL/TP-500-39154,* 2006.

[13] A. Rettenmeier, M. Hofsäß, D. Schlipf, J. J. Trujillo, B. Siegmeier and M. Kühn, "Wind field analyses using a nacelle-based LIDAR system," *Proc. European*

Wind Energy Conference, Warsaw, Poland, 2010.

[14] N. Angelou, T. Mikkelsen, K. H. Hansen, M. Sjöholm and M. Harris, "LIDAR Wind Speed Measurements from a Rotating Spinner: "SpinnerEx 2009"," *Risø-R-1741(EN),* 2010.

[15] A. K. Scholbrok, P. A. Fleming, L. J. Fingersh, A. D. Wright, D. Schlipf, F. Haizmann and F. Belen, "Field Testing LIDAR Based Feed-Forward Controls on the NREL Controls Advanced Research Turbine," *NREL/CP-5000-57339,* 2013.

[16] R. Gasch and J. Twele, "Windkraftanlagen," Teubner, Wiesbaden, 2005.

[17] E. A. Bossanyi, "The Design of closed loop controllers for wind turbines," *Wind Energy 3: 149–163,* 2000.

[18] E. L. van der Hooft, P. Schaak and T. G. van Engelen, "Wind turbine control algorithms," *ECN-C--03-111,* 2003.

[19] E. A. Bossanyi, "Individual blade pitch control for load reduction," *Wind Energy 6: 119–128,* 2003.

[20] T. G. van Engelen and E. L. van der Hooft, "Individual Pitch Control Inventory," *Technical Report ECN-E-03,* 2005.

[21] E. A. Bossanyi, "Further load reduction with Individual pitch control," *Wind Energy 8: 481–485,* 2005.

[22] F. Heß, "Ganzheitliche Regelung einer Windkraftanlage basierend auf einem parameteraffinen Entwurfsmodell," *Dissertation Technische Universität Berlin,* 2014.

[23] D. Schlipf and M. Kühn, "Prospects of a Collective Pitch Control by Means of Predictive Disturbance Compensation Assisted by Wind Speed Measurements," *German Wind Energy Conference (DEWEK), Bremen, Germany,* 2008.

[24] J. H. Laks, L. Y. Pao, E. Simley, A. D. Wright, N. Kelley and B. Jonkman, "Model Predictive Control Using Preview Measurements From LIDAR," *49th AIAA Aerospace Sciences Meeting including the New Horizons Forum and Aerospace Exposition, Orlando, Florida, USA,* 2011.

[25] L. Jespersen and M. W. Krogen, "Model Predictive LIDAR Control of Wind Turbines for Load Mitigation," *Master Thesis Aalborg University,* 2011.

[26] A. Körber and R. King, "Nonlinear Model Predictive Control for Wind Turbines," *Proc. EWEA Annual Event, Brussels, Belgium,* 2011.

[27] F. Dunne, D. Schlipf, L. Pao, A. Wright, B. Jonkman, N. Kelley and E. Simley, "Comparison of Two Independent Lidar-Based Pitch Control Designs," *Proc. AIAA Aerospace Sciences Meeting,* 2012.

[28] D. Schlipf, "Lidar-assisted control concepts for wind turbines," *Ph.D. dissertation, University of Stuttgart,* 2016.

[29] K. Williams and M. G. Bevilacqua, "Leon Battista Alberti's Bombard Problem in Ludi matematici: Geometry and Warfare," *The Mathematical Intelligencer,* 2013.

[30] International Electrotechnical Commission, IEC 61400-12-2 ed1.0: Wind turbines - Part 12-2: Power performance of electricity-producing wind turbines based on nacelle anemometry, 2013.

[31] W. Tong, "Wind Power Generation and Wind Turbine Design," *WIT Transactions on State-of-the-art in Science and Engineering,* 2010.

[32] T. F. Pedersen, N. Sørensen, H. A. Madsen, R. Møller, M. Courtney, P. Enevoldsen and P. Egedal, "Spinner Anemometry - an Innovative Wind Measurement Concept," *Proc. European Wind Energy Conference, Milan, Italy,* 2007.

[33] W. L. W. Henson, "Improving Sodar Data Processing and Reporting," *Renewable Energy Research Laboratory Report,* 2005.

[34] K. A. Browning, D. Beran, M. J. S. Quigley and C. G. Little, "Capabilities of radar, sodar and lidar for measuring the structure and motion of the stably stratified atmosphere," *Boundary-Layer Meteorology,* no. 5, 1973.

[35] T. Mikkelsen, "Remote Sensing of Wind," *Proc. Summer School in Remote Sensing for Wind Energy, Boulder, Colorado, USA,* 2012.

[36] P. Lindelöw and M. Courtney, "Five Years of Lidar Anemometry in the Wind Energy Industry," *Proc. 15th Coherent Laser Radar Conference, Toulouse, France,* 2009.

[37] M. B. Christiansen, "Wind Energy Applications of Synthetic Aperture Radar," *Risø-PhD-27(EN),* 2006.

[38] B. D. Hirth and J. L. Schroeder, "Measurements of the complex flows through a wind farm using mobile Doppler radars," *Proc. EWEA Annual Event, Vienna,*

Austria, 2013.

[39]   C. Weitkamp, "Lidar - Range-Resolved Optical remote Sensing of the Atmosphere," *Springer Series in Optical Sciences,* 2005.

[40]   N. Sela, "The SpiDAR Wind Measurement Technique," 2012. [Online]. Available: http://www.windtech-international.com/editorial-features/features/articles/the-spidar-wind-measurement-technique. [Accessed 26 05 2013].

[41]   X. Chu, "Lecture 2 Laser Remote Sensing Overview," 2006. [Online]. Available: http://sisko.colorado.edu/NOTES/Lecture2.pdf. [Accessed 26 05 2013].

[42]   C. F. Abari, A. T. Pedersen and J. Mann, "An all-fiber image-reject homodyne coherent Doppler wind lidar," *Optical Society of America,* 2014.

[43]   C. Slinger and M. Harris, "Introduction to continuous-wave Doppler lidar," *Proc. Summer School in Remote Sensing for Wind Energy, Boulder, Colorado, USA,* 2012.

[44]   G. Vaughan, "Lidar Profiling of the Atmosphere," *Proc. Cargese International School Cost Action 723, Cargese, France,* 2005.

[45]   C. Hill and M. Harris, "QinetiQ Lidar Measurement Report," *Remote Sensing (UpWind WP6),* 2010.

[46]   J.-P. Cariou, "Pulsed lidars," *Risø–I–3184(EN),* 2012.

[47]   A. Peña, "Sensing the wind profile," *Risø-PhD-45(EN),* 2009.

[48]   A. Betz, "Das Maximum der theoretisch möglichen Ausnutzung des Windes durch Windmotoren," *Zeitschrift für das gesamte Turbinenwesen,* 1920.

[49]   R. Hunter, T. F. Pedersen, P. Dunbabin, I. Antoniou, S. Frandsen, H. Klug, A. Albers and W. K. Lee, "Measurement Method to Verify Wind Turbine Performance Characteristics," *Risø-R-1209(EN),* 2001.

[50]   G. C. Larsen, H. A. Madsen, F. Bingöl, J. Mann, S. Ott, J. N. Sørensen, V. Okulov, N. Troldborg, M. Nielsen, K. Thomsen, T. J. Larsen and R. Mikkelsen, "Dynamic wake meandering modeling," *Risø Report R-1607(EN),* 2007.

[51]   P. M. O. Gebraad, F. W. Teeuwisse, J. W. van Wingerden, P. A. Fleming, S. D. Ruben, J. R. Marden and L. Y. Pao, "A Data-Driven Model for Wind Plant Power Optimization by Yaw Control," *Proc. American Control Conference (ACC),* 2014.

[52] B. F. Lund, P. N. Oma and T. Jakobsen, "Wind farm production maximization through joint optimization of turbine efficiency and yaw," *Proc. EWEA Annual Event, Barcelona, Spain,* 2014.

[53] G. I. Taylor, "The spectrum of turbulence," *Proc. The Royal Society of London, Series A: Mathematical, Physical and Engineering Sciences,* 1938.

[54] M. Sjöholm, S. Kapp, L. Kristensen and T. Mikkelsen, "Experimental evaluation of a model for the influence of coherent wind lidars on their remote measurements of atmospheric boundary-layer turbulence," *Proc. SPIE 8182, Lidar Technologies, Techniques, and Measurements for Atmospheric Remote Sensing VII, Prague, Czech Republic,* 2011.

[55] S. Kapp, "Speed Control of Wind Turbines by Use of Remote Sensing Technologies," *Diploma Thesis, University of Stuttgart,* 2010.

[56] S. Kapp, "Speed Control of Wind Turbines by Use of Remote Sensing Technologies," *PhD Summer School, Risø, Roskilde, Denmark,* 2010.

[57] M. Sjöholm, T. Mikkelsen, L. Kristensen, J. Mann, P. Kirkegaard, S. Kapp, D. Schlipf and J. J. Trujillo, "Spectral analysis of wind turbulence measured by a Doppler Lidar for velocity fine structure and coherence studies," *Proc. 15th International Symposium for the Advancement of Boundary Layer Remote Sensing (ISARS), Paris, France,* 2010.

[58] N. Angelou, J. Mann, M. Sjöholm and M. Courtney, "Direct measurement of the spectral transfer function of a laser based anemometer," *Review of scientific instruments,* vol. 83, 2012.

[59] E. Simley, L. Y. Pao, N. Kelley, B. Jonkman and R. Frehlich, "LIDAR Wind Speed Measurements of Evolving Wind Fields," *Proc. ASME Wind Energy Symposium, National Harbor, Maryland, USA,* 2012.

[60] D. Schlipf, "LiDAR and wind turbine control," *Proc. PhD Summer School: Remote sensing for wind energy, Roskilde, Denmark,* 2009.

[61] F. M. J. F. D. Bingöl, "Modeling conically scanning lidar error in complex terrain with WAsP Engineering," *Meteorol. Z. 18,* pp. 189-195, 2009.

[62] A. T. Pedersen and T. Mikkelsen, "Blade lidar experiments," *Meeting: Integration of Wind LIDARs in Wind Turbines for Improved Productivity and Control (HTF 049-2009-3), Roskilde, Denmark,* 2012.

[63] M. Harris, "Introduction to continuous-wave Doppler lidar," *Remote Sensing for*

Wind Energy, pp. 69-92, 2010.

[64] C. Hasager, A. Peña, T. Mikkelsen, M. Courtney, I. Antoniou, S.-E. Gryning, P. Hansen and P. B. Sørensen, "12MW Horns Rev Experiment," *Risø-R-1506(EN),* 2007.

[65] M. Sjöholm, A. T. Pedersen, N. Angelou, F. F. Abari, T. Mikkelsen, M. Harris, C. Slinger and S. Kapp, "Full two-dimensional rotor plane inflow measurements by a spinner-integrated wind lidar," *Proc. EWEA Annual Event, Vienna, Austria,* 2013.

[66] C. Hill, "Remote Sensing (UpWind WP6) QinetiQ Lidar Availability Report," *Upwind Technical Report,* 2010.

[67] C. Mohr, I. Alberts, M. Masbou and A. Bott, "Nebelbildung am Flughafen München: Klimatologie und Modellierung," *Report Universität Bonn,* 2009.

[68] E. A. Bossanyi, A. Kumar and O. Hugues-Salas, "Wind turbine control applications of turbine-mounted LIDAR," *Journal of Physics: Conference Series 555,* 2012.

[69] E. Hau, Windkraftanlagen: Grundlagen, Technik, Einsatz, Wirtschaftlichkeit, 4th ed., Berlin, Heidelberg: Springer, 2008.

[70] D. Schlipf, S. Kapp, J. Anger, O. Bischoff, M. Hofsäß, A. Rettenmeier and M. Kühn, "Prospects of Optimization of Energy Production by LIDAR Assisted Control of Wind Turbines," *Proc. EWEA Annual Event, Brussels, Belgium,* 2011.

[71] C. Voigt and J. Adamy, "Formelsammlung der Matrizenrechnung," *Oldenbourg Wissenschaftsverlag,* 2007.

[72] C. Slinger, M. Leak, M. Pitter and M. Harris, "Relative Power Curve Measurements Using Turbine Mounted, Continuous-Wave Lidar," *Proc. EWEA Annual Event, Vienna, Austria,* 2013.

[73] S. Kapp and M. Kühn, "A Five-Parameter Wind Field Estimation Method Based on Spherical Upwind Lidar Measurements," *Proc. The Science of Making Torque from Wind, Oldenburg, Germany,* 2012.

[74] W. Gander, M. J. Gander and F. Kwok, Scientific Computing - An Introduction using Maple and MATLAB, Cham, Switzerland: Springer, 2014.

[75] E. Anderson, "LAPACK Users' Guide," *Society for Industrial & Applied*

Mathematics, 1995.

[76] Encyclopedia of Mathematics, "Kolmogorov–Smirnov test," [Online]. Available: http://www.encyclopediaofmath.org/index.php/Kolmogorov%E2%80%93Smirnov_test. [Accessed 26 05 2013].

[77] D. Schlipf, P. Fleming, A. Scholbrock, S. Raach, F. Haizmann, P. W. Cheng, R. Krishnamurthy and M. Boquet, "An Adaptive Data Processing Technique for Lidar-Assisted Control to Bridge the Gap Between Lidar Systems for Wind Turbines," *NREL/CP-5000-65273,* 2015.

[78] A. Scholbrock, P. Fleming, A. Wright, C. Slinger, J. Medley and M. Harris, "Field Test Results from Lidar Measured Yaw Control for Improved Yaw Alignment with the NREL Controls Advanced Research Turbine," *NREL/CP-5000-63202,* 2014.

[79] The Danish National Advanced Technology Foundation, "Intelligent wind turbines make better use of the wind," [Online]. Available: http://hoejteknologifonden.dk/en/project_gallery/project_gallery/intelligent_wind_turbines_make_better_use_of_the_wind/. [Accessed 21 09 2013].

[80] M. Sjöholm, N. Angelou, T. Mikkelsen, A. Pedersen, S. Kapp, M. Harris and C. Slinger, "Two-dimensional structures in wind turbine inflow studied by a spinner-mounted windscanner," *17th International Symposium for the Advancement of Boundary-Layer Remote Sensing (ISARS), Auckland, New Zealand,* 2014.

[81] T. Mikkelsen, J. Mann and M. Nielsen, "Rotating Prism Scanning Device and Method for Scanning". Patent WO 2009/155923 A1, 2009.

[82] T. Mikkelsen, N. Angelou, K. Hansen, M. Sjöholm, M. Harris, C. Slinger, P. Hadley, R. Scullion, G. Ellis and G. Vives, "A spinner-integrated wind lidar for enhanced wind turbine control," *Wind Energy,* pp. 625-643, 16 10 2013.

[83] E. Branlard, A. T. Pedersen, J. Mann, N. Angelou, A. Fischer, T. Mikkelsen, M. Harris, C. Slinger and B. F. Montes, "Retrieving wind statistics from average spectrum of continuous-wave lidar," *Atmospheric Measurement Techniques,* 2013.

[84] NREL National Renewable Energy Laboratory, "NWTC - Computer-Aided Engineering Tools (FAST)," 2013-11-26. [Online]. Available: http://wind.nrel.gov/designcodes/simulators/fast/.

[85] S. Kapp, F. Heß and M. Kühn, "Sensitivity of Lidar Measurement Chain Uncertainties on Wind Turbine Load Reductions Applying Feedforward Pitch

Control," *Proc. EWEA Annual Event, Vienna, Austria,* 2013.

[86] D. Schlipf, E. Bossanyi, C. E. Carcangiu, T. Fischer, T. Maul and M. Rossetti, "LIDAR assisted collective pitch control," *UpWind Deliverable D5.1.3,* 2010.

[87] GL Garrad Hassan, "Bladed," [Online]. Available: http://www.gl-garradhassan.com/en/GHBladed.php. [Accessed 26 11 2013].

[88] F. Dunne, E. Simley and L. Pao, "LIDAR Wind Speed Measurement Analysis and Feed-Forward Blade Pitch Control for Load Mitigation in Wind Turbines," *NREL Subcontract Report,* 2011.

[89] NREL National Renewable Energy Laboratory, "NWTC - Computer-Aided Engineering Tools (TurbSim)," [Online]. Available: http://wind.nrel.gov/designcodes/preprocessors/turbsim/. [Accessed 26 11 2013].

[90] The MathWorks, Inc., "Interpolate scattered data - MATLAB griddata," [Online]. Available: http://www.mathworks.de/de/help/matlab/ref/griddata.html. [Accessed 26 11 2013].

[91] The MathWorks, Inc., "Interpolate scattered data - MATLAB TriScatteredInterp," [Online]. Available: https://www.mathworks.de/help/matlab/ref/triscatteredinterp.html. [Accessed 26 11 2013].

[92] IEC/TC 88, *IEC 61400-1: Wind turbines - Part 1: Design requirements,* 2007.

[93] E. A. Bossanyi, "Un-freezing the turbulence: improved wind field modelling for investigating Lidar-assisted wind turbine control," *EWEA Proceedings, Vienna, Austria,* 2012.

[94] L. Kristensen, "On longitudinal spectral coherence," *Boundary Layer Meteorology, 16,* pp. 145-153, 1979.

[95] A. V. Oppenheim and R. W. Schafer, "Discrete-Time Signal Processing," *Pearson,* 2009.

[96] Massachusetts Institute of Technology, Department of Electrical Engineering and Computer Science, "DT Filter Design: IIR Filters," OpenCourseWare, Cambridge, MA, USA, 2006.

[97] F. Heß and G. Seyboth, "Individual Pitch Control with Tower Side-to-Side Damping," *10th German Wind Energy Conference (DEWEK), Bremen,*

Germany, 2010.

[98]   E. Haibach, "Betriebsfestigkeit - Verfahren und Daten zur Bauteilberechnung," *Springer,* 2006.

[99]   MAKE Consulting, "Wind Turbine Trends," 2011.

[100] Bottasso, C. L., Campagnolo, F., Croce, A., Tibaldi, C., "Optimization-Based Study of Bend-Twist Coupled Rotor Blades for Passive and Integrated Passive/Active Load Alleviation," *Wind Energy Vol 16,* pp. 1149-1166, 2013.

[101] J. Gottschall, "Modelling the variability of complex systems by means of Langevin processes," *Dissertation, Carl von Ossietzky Universität Oldenburg,* 2009.

[102] J. Gottschall and J. Peinke, "Stochastic modelling of a wind turbine's power output with special respect to turbulent dynamics," *Journal of Physics: Conference Series 75,* 2007.

[103] B. Cañadillas and T. Neumann, "First Test of a Nacelle-based "2-beam" Wind LiDAR System under Offshore Conditions," *DEWI Magazin,* 2011.

[104] A. Rettenmeier, P. Klausmann, O. Bischoff, M. Hofsäß, D. Schlipf and B. Siegmeier, "Determination of power curves based on wind field measurements using a nacelle-based LiDAR scanner," *Proc. EWEA Annual Event, Brussels, Belgium,* 2011.

[105] R. Wagner, T. F. Pedersen, M. Courtney, I. Antoniou, S. Davoust and R. L. Rivera, "Power curve measurement with a nacelle mounted lidar," *Wind Energy Volume 17, Issue 9,* 2013.

[106] Kühn, M., Reuter, R., Cheng, P. W., Hofmeister, P. G., Kunze, M., Raach, S., Schlipf, D., Wächter, M., Würth, I., "Abschlussbericht des Forschungsprojekts »Entwicklung gondelbasierter Lidar-Technologien für die Messung des Leistungsverhaltens und die Regelung von Windenergieanlagen« LIDAR II," *Universiät Oldenburg,* 2015.

[107] K. Kragh, "Performance Enhancement and Load Reduction on Wind Turbines Using Inflow Measurements," *DTU Wind Energy PhD-0014 (EN),* 2013.

[108] C. Schwarze, "A New Look at Risley Prisms," *Photonics Spectra,* 06 2006.

Appendix A: Lidar Field Experiment Details

A.1 Scan Patterns of the Experimental Two-Dimensional Lidar

$t = 1$ s
$t = 2$ s
$t = 3$ s
$t = 4$ s
$t = 5$ s
$t = 6$ s
$t = 7$ s
$t = 8$ s
$t = 9$ s
$t = 10$ s
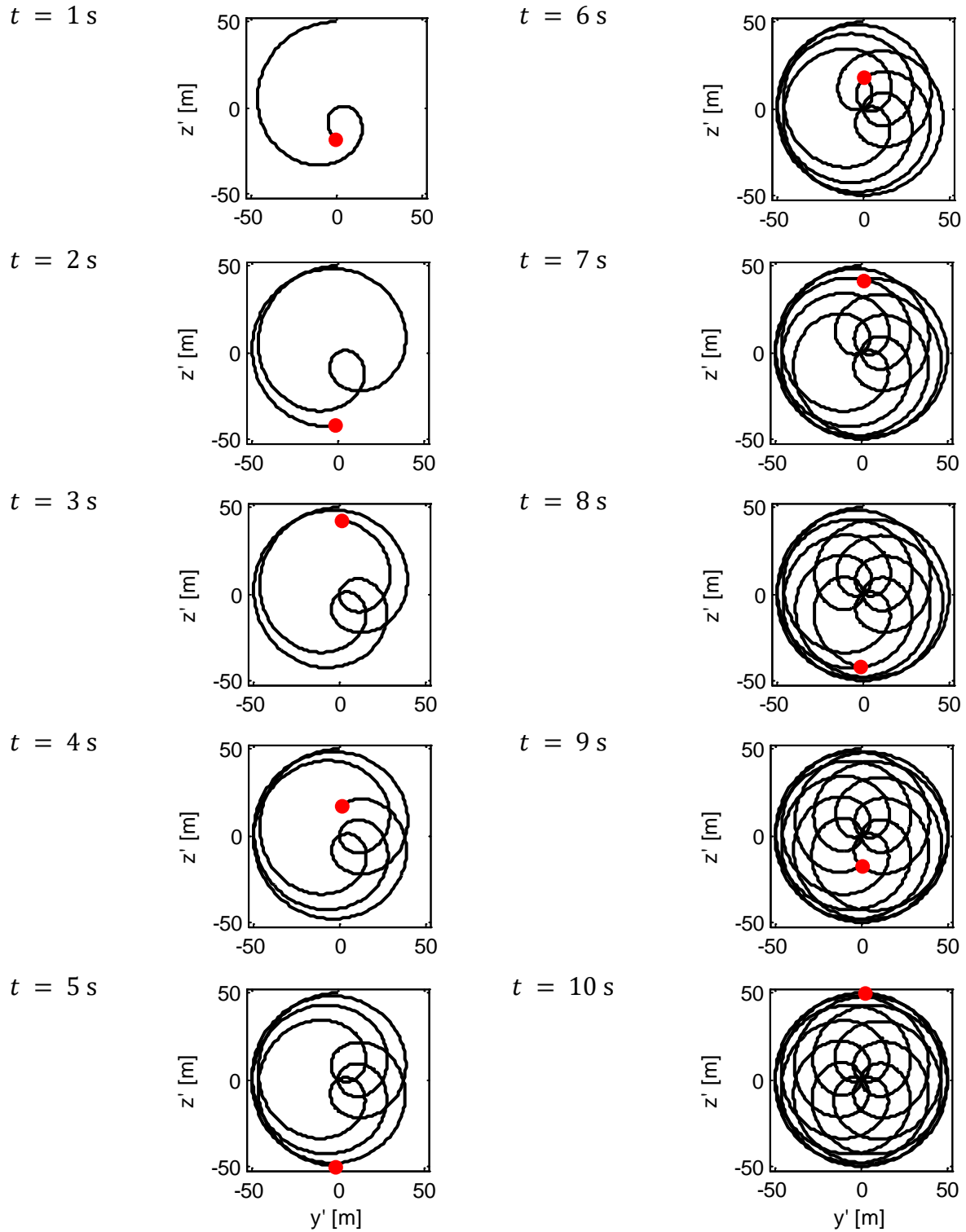
Figure A.1-1: Double prism scan pattern in a rotating y'-z'-frame of reference, $t = 1 \dots 10$ s.

$t = 1$ s

$t = 6$ s

$t = 2$ s

$t = 7$ s

$t = 3$ s

$t = 8$ s

$t = 4$ s

$t = 9$ s

$t = 5$ s

$t = 10$ s
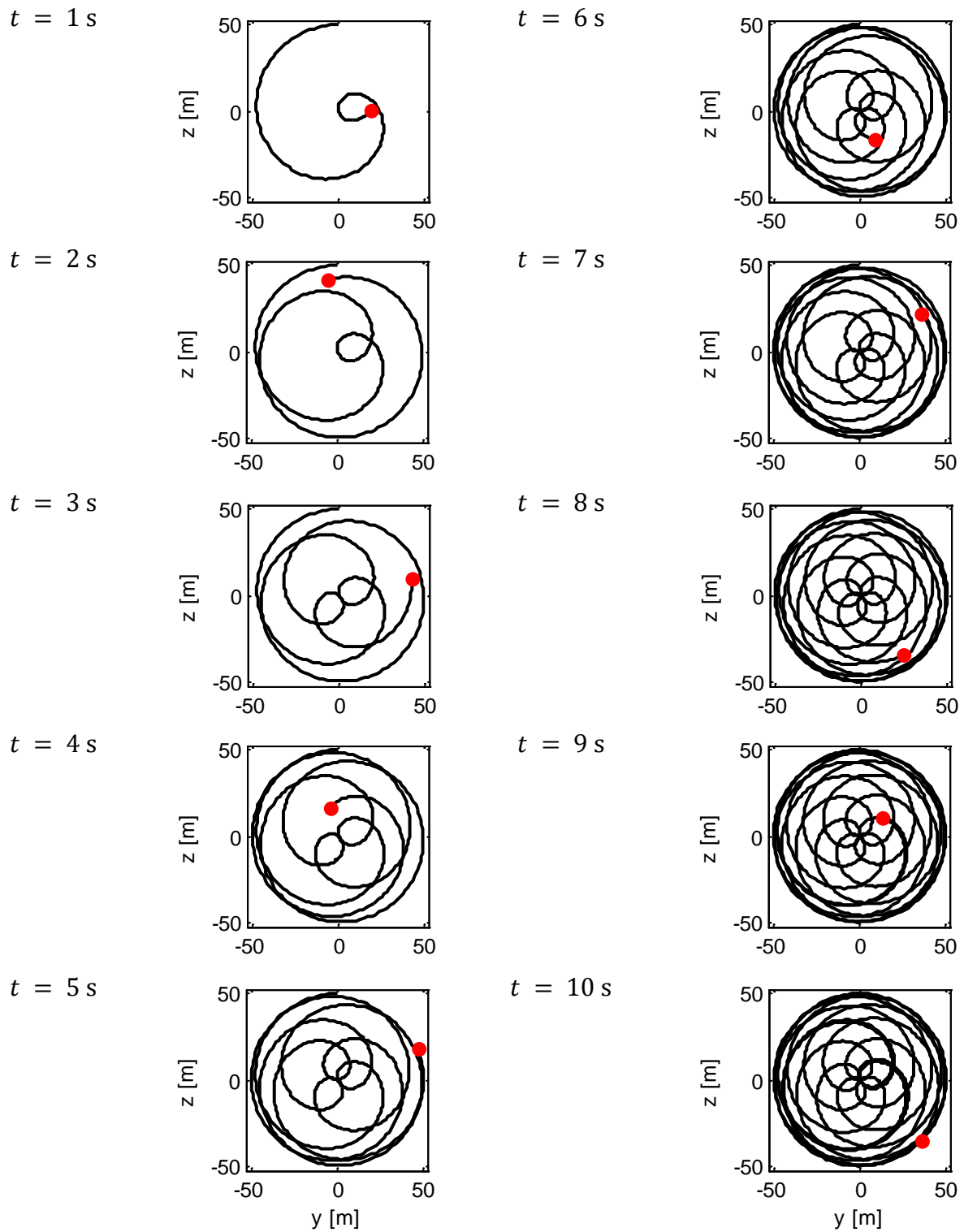
Figure A.1-2: Double prism scan pattern in a rotor fixed y-z-frame of reference, at rotor speed one revolution per 3.8 s, $t = 1 \ldots 10$ s.

A.2 Identification of Relative Intensity Noise of the ZephIR Spinner Lidar Using Experimental Data

1. Two ten minute periods of lidar spectral data were chosen during low and high wind speeds
   a. 2012-09-09, 23:40-23:50
   b. 2012-09-06, 20:00-20:10
2. For each period the median of all spectra is calculated. In frequency ranges of unlikely wind speeds the median should indicate the noise level better than the mean.
3. Figure A.2-1 top and middle also show the standard deviation of spectral data above and below the median. It can be seen that in the high frequency range most spectra are below the median whereas in ranges of (likely) wind speed occurrences, most data is above.
4. To determine the relative intensity noise (RIN), the minimum of both median spectra is calculated (red dashed line).
5. Bins up to 7 are proposed to be excluded from the analysis; RIN identification is not possible in this range.
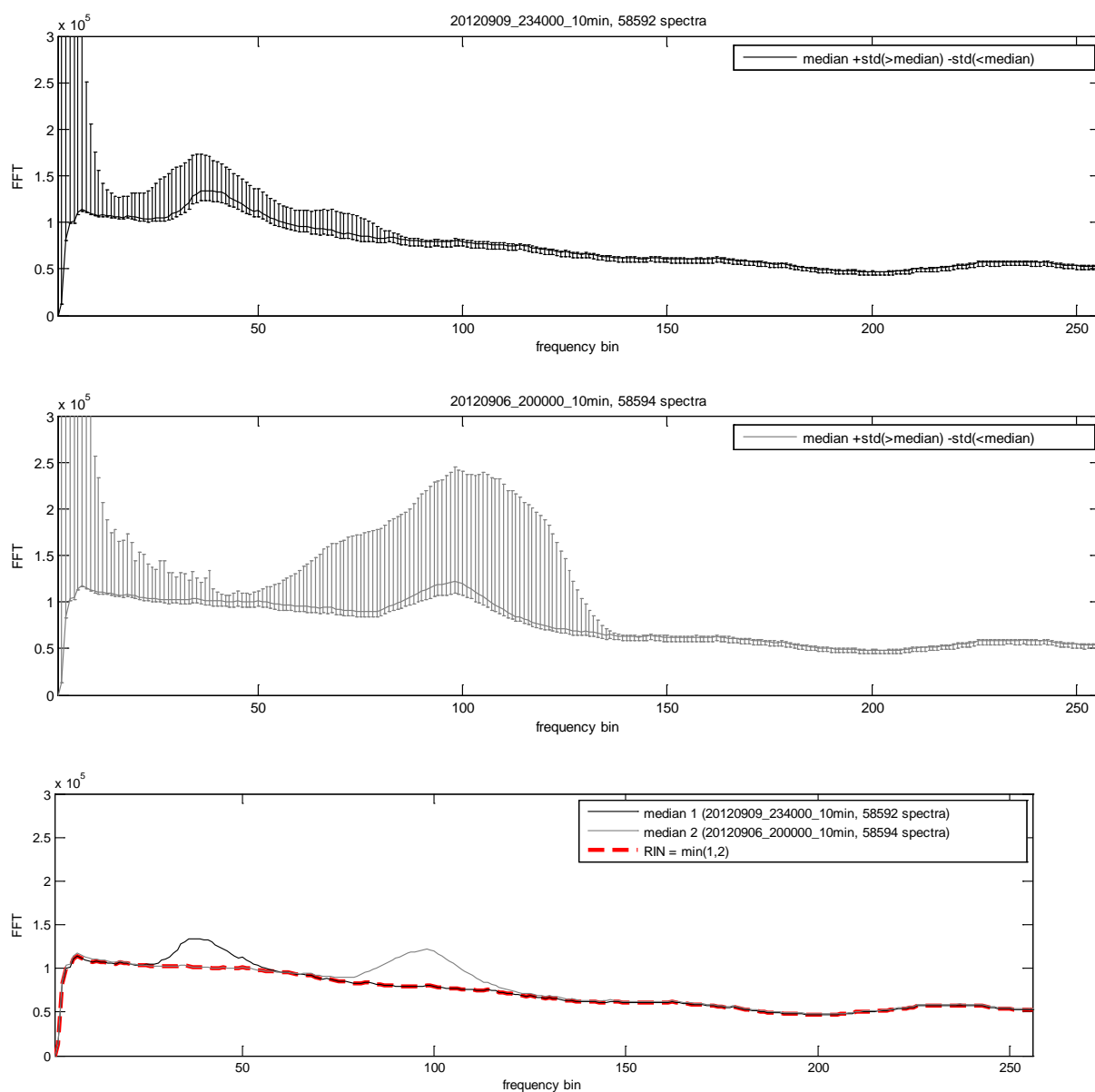
Figure A.2-1: RIN spectrum calculation
Top and middle: median of sample spectra and standard deviations per frequency,
separately for above and below the median.
Bottom: for mast, turbine and lidar measurements respectively.

A.3 Time Series of the Considered Experimental Period
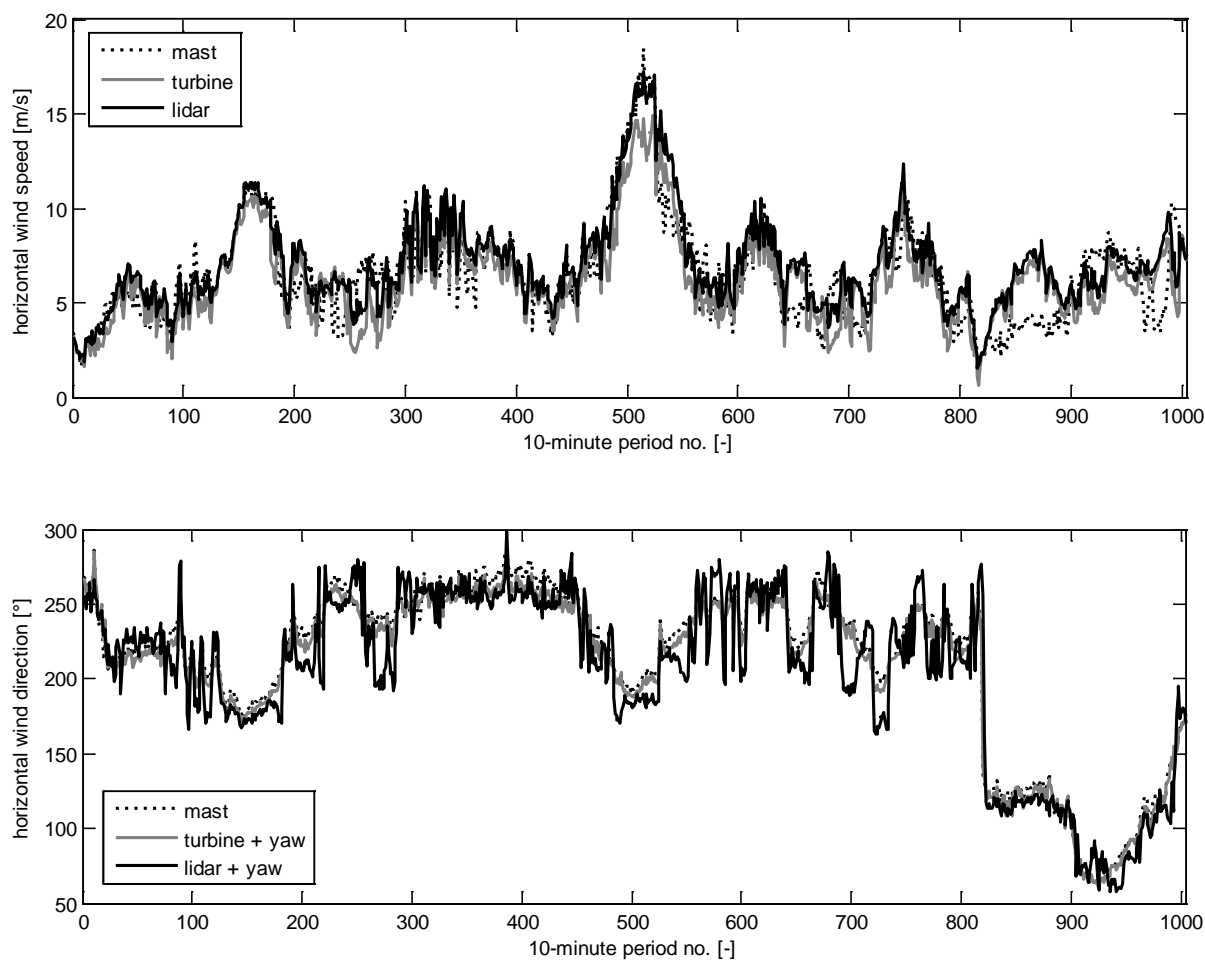
Figure A.3-1: Time series of horizontal wind speed and direction for mast, turbine and lidar measurements respectively (10-minute averages).

A.4 Scan Example of the Experimental Two-Dimensional Lidar
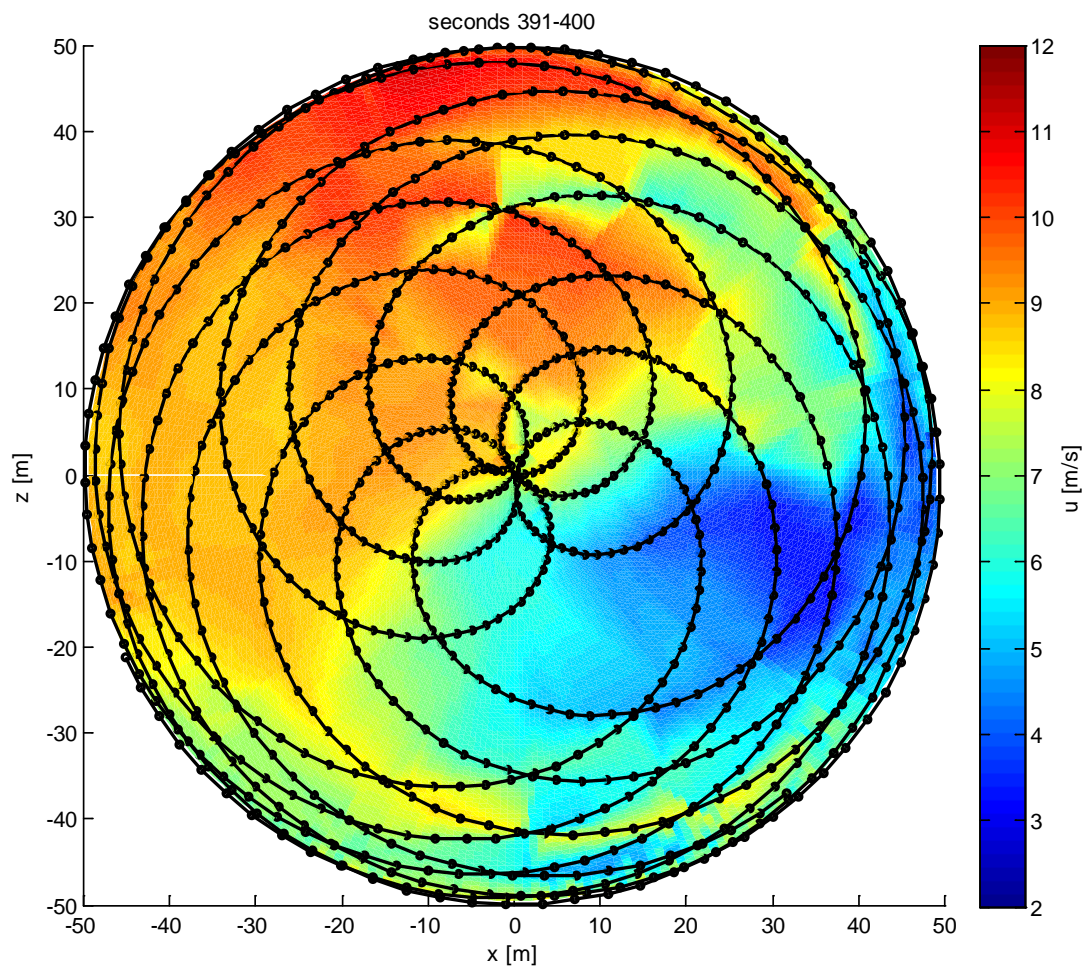
Figure A.4-1: Scan of 977 measurement samples during 10 seconds projected on the wind speed u-components, in non-rotating tilted turbine coordinates x-y-z, x is rotor axis in tilted downwind direction, and colour coded numerical interpolation between the scans.

Appendix B: Simulation Details and further Results

B.1 Wind Turbine Model

The generic 2.5 MW wind turbine model used for the simulations described in Chapter 6 represents a typical Type Class IIa pitch regulated multi megawatt onshore wind turbine. It was chosen due to its industrial relevance and its similarity to the experimental turbine described in Chapter 5. The steady state characteristics are given in Figure B.1-1.
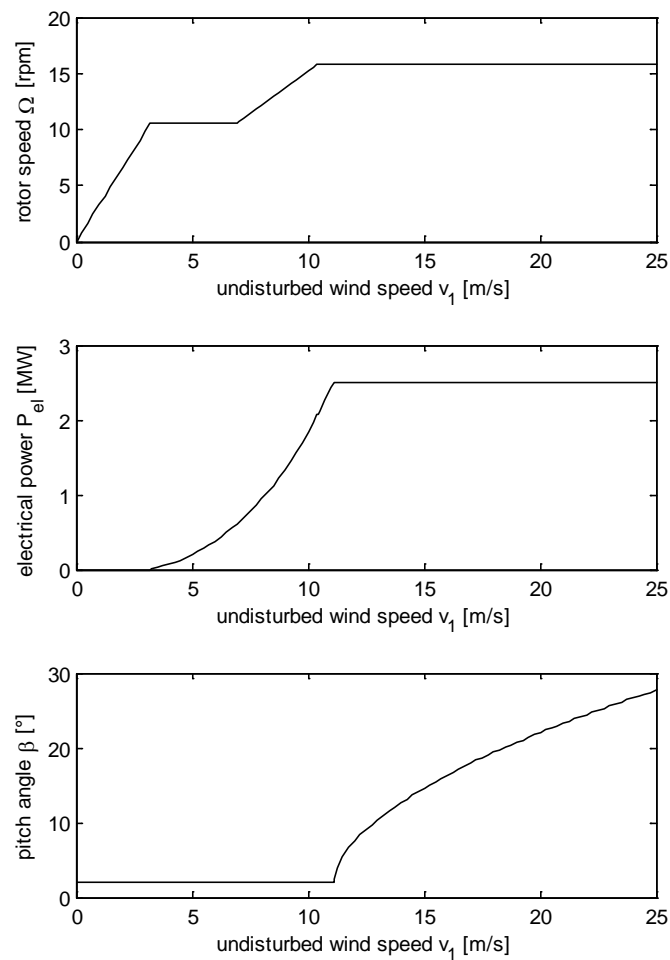
Figure B.1-1: Steady state characteristics of the simulated generic 2.5 MW wind turbine model.

B.2 Transformation Matrix Cartesian to Polar

Figure B.2-1: Identity elements (black) in matrix M found by implementing the nearest neighbour interpolation method. A 13×13 Cartesian grid is mapped onto polar circle of 32 points.

Figure B.2-2: Matrix elements from 0 (white) to 1 (black) found by implementing a linear interpolation method for the same grids as in Figure B.2-1.

B.3 Scan and Filter Cut-Off Variation

If a scanning turbine mounted lidar is used for the calculation of feedforward blade pitch angles, the quality of the feedforward signal should increase with the number of (quasi-simultaneously) scanned focus positions in the inflow, because turbulence within the scanned area is filtered out. A similar effect can be assumed by low-pass filtering the feedforward command, since turbulent fluctuations over time are filtered out.

In this parameter variation simulation, the influence of the number of scanned lidar focus points and the cut-off frequency of the feedforward signal on the damage equivalent loads (DELs) of the blade, shaft and tower are studied.

The simulations and DEL-calculations are carried out analogue to the reference fatigue load simulations of Subsection 6.2.1, but with a reduced measurement distance of $x_{focus} = 38\,\text{m}$, a varied number of equiazimuthal focus positions n_{84} on a circle at $0.84\,R$, calculating collective feedforward (CFF) pitch angles and varied corner frequencies of a noncausal forward-backward Butterworth filter of 2nd order.

The relative DELs with respect to collective feedback pitch control are presented in Figures B.3-1 to B.3-3 analogue to Subsection 6.2.1., plotted against the cut-off frequency of the low pass filter, and with varied number of scanned positions.

A higher number of scanned points up to around 8 to 12 leads to significantly reduced fatigue loads, especially at higher cut-off frequencies. Forward-backward-filtering with lower cut-off frequencies tend to result in lower loads for all scan strategies.

In the sensitivity analysis in Subsection 6.2.5 the noncausal filter is replaced by a realizable wind speed adaptive filter with lowest possible cut-off frequency.
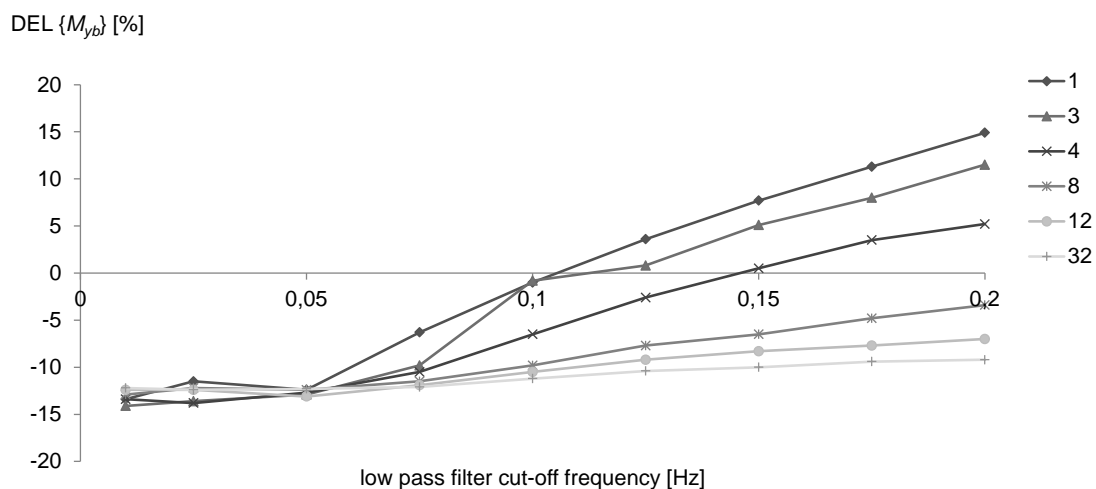
Figure B.3-1: Change in fatigue load of the fore-aft blade root bending moment M_{yb} of CFF + IPC w.r.t. CPC

DEL {M_{xa}} [%]
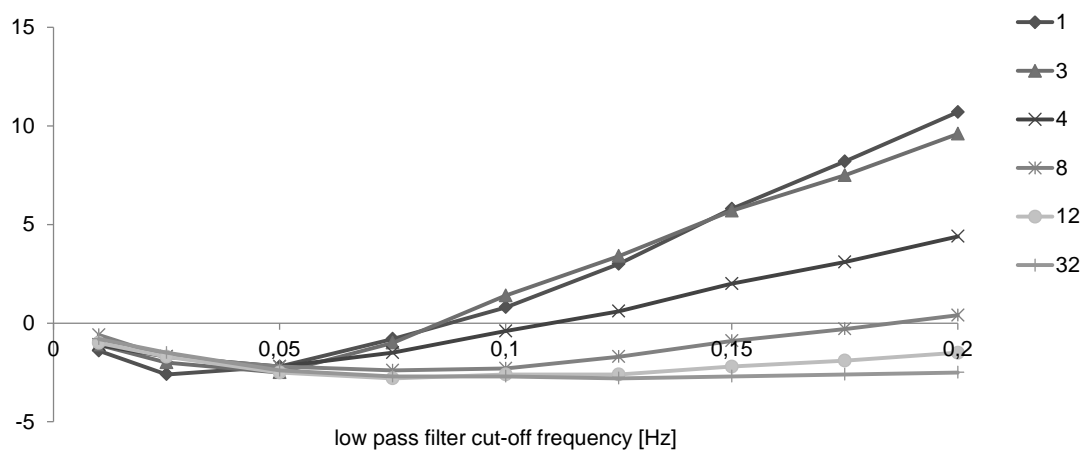
Figure B.3-2: Change in fatigue load of the rotor shaft torque M_{xs} of CFF + IPC w.r.t. CPC

DEL {M_{yt}} [%]
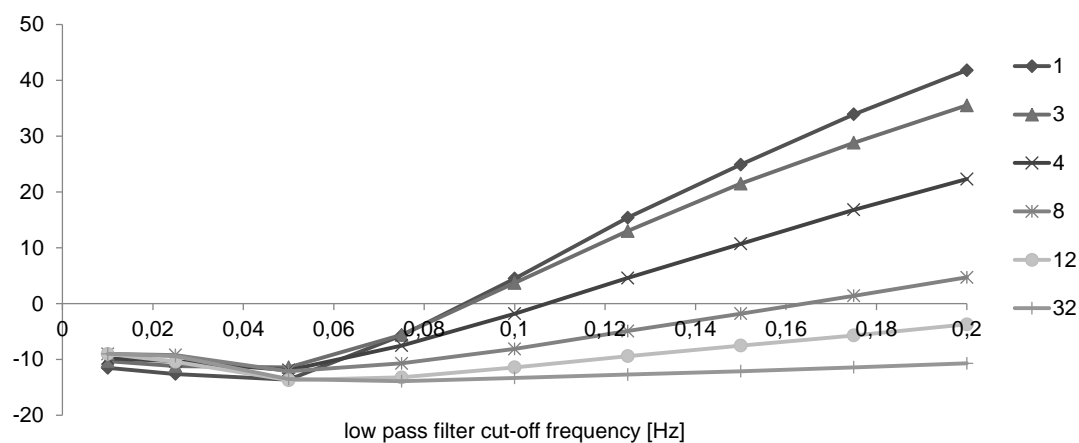
Figure B.3-3: Change in fatigue load of the fore-aft tower base moment M_{yt} of CFF + IPC w.r.t. CPC

B.4 Simulated Wind Direction Errors of 3pe and 5pe methods using IEC Wind Fields
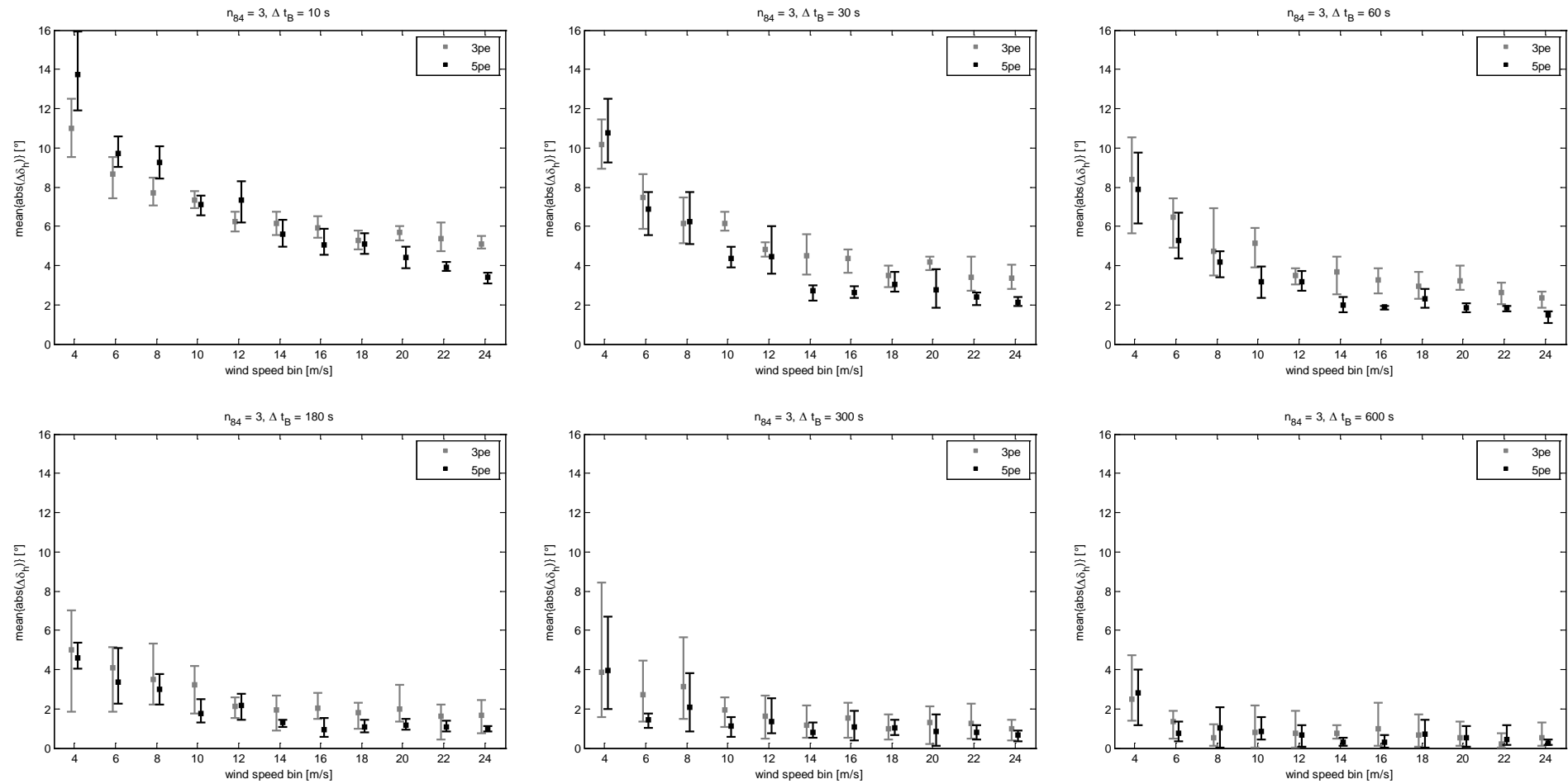
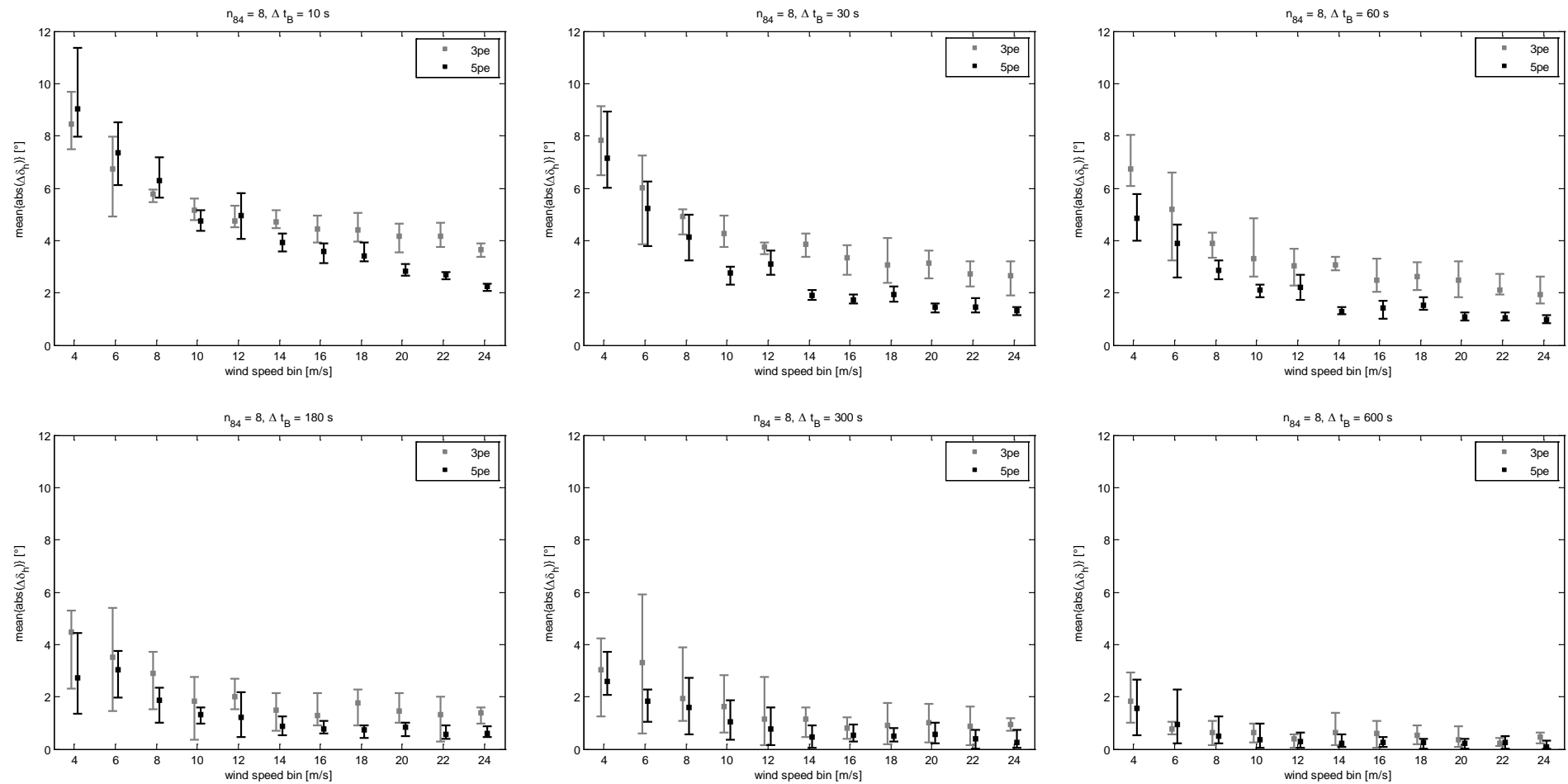*Figure B.4-1: Simulated wind direction errors for different averaging intervals, 3 measurement points*

Figure B.4-2: Simulated wind direction errors for different averaging intervals, 8 measurement points
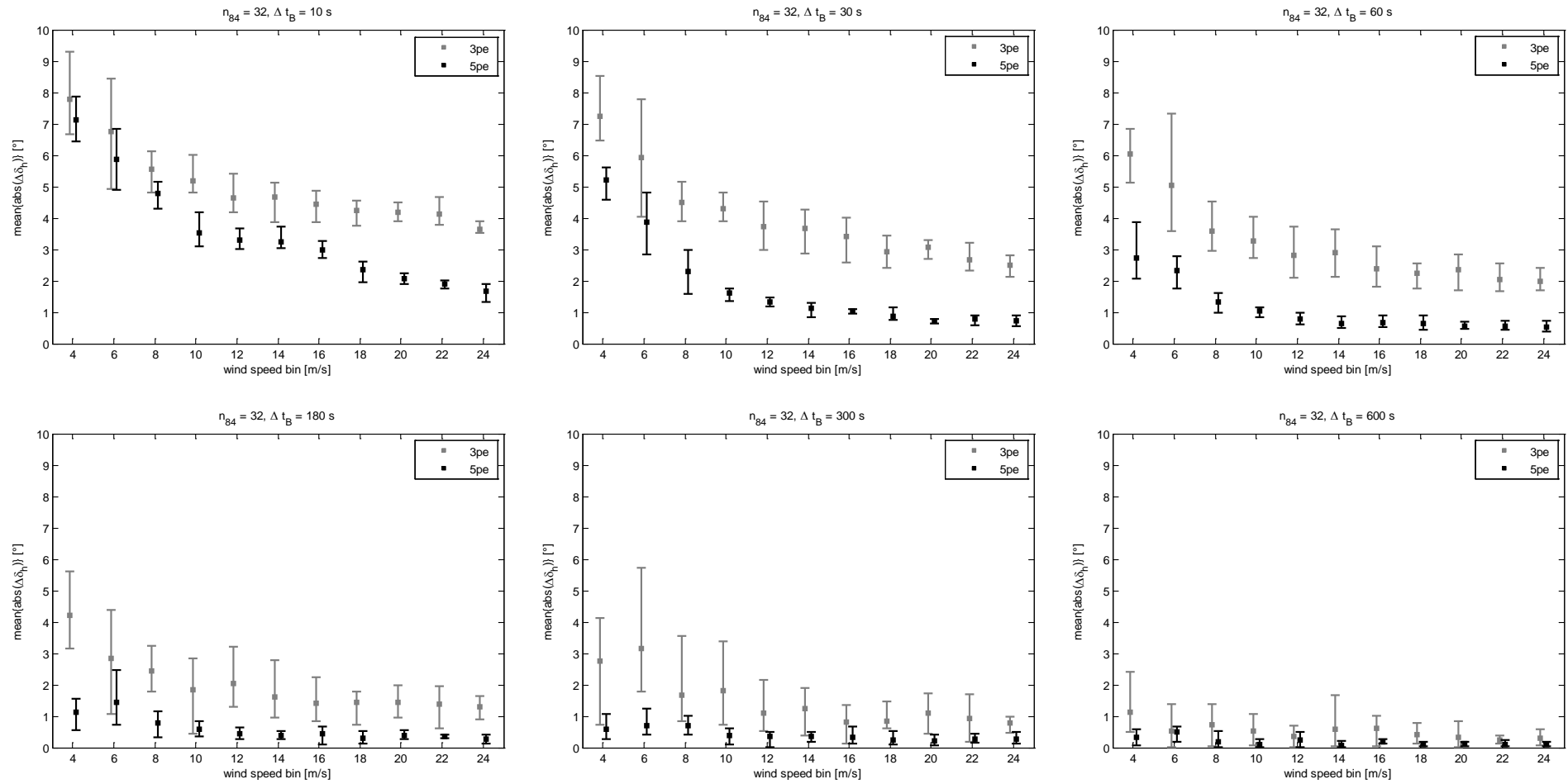
Figure B.4-3: Simulated wind direction errors for different averaging intervals, 32 measurement points

List of Publications

M. Sjöholm, N. Angelou, T. Mikkelsen, A. T. Pedersen, S. Kapp, M. Harris, C. Slinger, "Two-dimensional structures in wind turbine inflow studied by a spinner-mounted lidar", 19th International Symposium for the Advancement of Boundary-Layer Remote Sensing Auckland, New Zealand, 2014

D. Schlipf, P. Fleming, S. Kapp, A. K. Scholbrok, F. Haizmann, F. Belen, A. Wright, P. W. Cheng, "Field Testing of Direct Speed Control Using Lidar", Proc. American Control Conference, Washington, D.C., USA, 2013

M. Sjöholm, A. T. Pedersen, N. Angelou, F. F. Abari, T. Mikkelsen, M. Harris, C. Slinger, S. Kapp, "Full Two-Dimensional Rotor Plane Inflow Measurements by Spinner-Integrated Wind Lidar", Proc. EWEA Annual Event, Vienna, Austria, 2013

S. Kapp, F. Heß, M. Kühn, "Sensitivity of Lidar Measurement Chain Uncertainties on Wind Turbine Load Reductions Applying Feedforward Pitch Control", Proc. EWEA Annual Event, Vienna, Austria, 2013

S. Kapp, M. Kühn, "A Five-Parameter Wind Field Estimation Method Based on Spherical Upwind Lidar Measurements", Proc. EAWE Making Torque, Oldenburg, Germany, 2012

M. Sjöholm, S. Kapp, L. Kristensen, T. Mikkelsen, "Experimental evaluation of a model for the influence of coherent wind lidars on their remote measurements of atmospheric boundary-layer turbulence", Proc. of SPIE. Vol. 8182, Prague, Czech Republic, 2011

D. Schlipf, S. Kapp, J. Anger, O. Bischoff, M. Hofsäß, A. Rettenmeier, M. Kühn, "Prospects of Optimization of Energy Production by LIDAR Assisted Control of Wind Turbines", Proc. EWEA Annual Event, Brussels, Belgium, 2011

M. Sjöholm, T. Mikkelsen, L. Kristensen, J. Mann, P. Kirkegaard, S. Kapp, D. Schlipf, J. J. Trujillo, "Spectral analysis of wind turbulence measured by a Doppler Lidar for velocity fine structure and coherence studies", Proc. ISARS, Paris, France, 2010

S. Kapp, "Speed Control of Wind Turbines by Use of Remote Sensing Technologies", PhD Summer School, 7-11 June 2010, Risø DTU, Roskilde, Denmark, 2010

List of Published Patents

J. Fehse, F. Hess, S. Kapp, M. Voss, "Verfahren und Steuergerät zum Ansteuern einer Winkelverstellung für Blätter eines Rotors einer Windenergieanlage", DE Patent DE102014212475A1, 27.06.2014, published 31.12.2015

J. Damerau, A. Paweletz, S. Kapp, B. Buchtala, J. Fehse, T. Herrmann and L. Schindele, "Method for operating wind energy plant of wind farm, involves determining target operation target to limit mechanical load at one of wind energy plants using first degree of wear and second degree of wear of wind energy plants". DE Patent DE102013002662A1, 18.02.2013, published 21.08.2014.

F. Hess and S. Kapp, "Method and device for reducing a pitch moment which loads a rotor of a wind power plant". DE/ US/ CN Patent DE102012024272A1/ US020140161610A1/ CN000103867384A, 12.12.2012/ 10.12.2013/ 11.12.2013, published 12.06.2014/ 12.06.2014/ 18.06.2014.

S. Kapp, M. Voss and B. Buchtala, "Device for determining wind field parameters for wind energy plant, has deflecting unit to variably deflect laser beam in relation to axial direction, so that two measuring points are scanned at different distances". DE Patent DE102012019663A1, 08.10.2012, published 10.04.2014.

S. Kapp and R. Gauch, "Method for monitoring and operating wind energy plant within wind farm, involves determining mechanical load of energy plant by evaluating device, and providing control variables of energy plant to control device based on measured variables". DE Patent DE102011112627A1, 06.09.2011, published 07.03.2013.

Acknowledgements/ Danksagungen

Curriculum Vitae

Personal Data

Name	Stefan Kapp
Date of birth	27th of August 1984
Place of birth	Ludwigsburg
Nationality	German
Family status	Married, one child

Education

09/1995 - 07/2004	Friedrich-Schiller-Gymnasium Ludwigsburg, Germany Degree: General higher education entrance qualification
10/2004 - 04/2010	Universität Stuttgart, Germany Degree: Diplom-Ingenieur Engineering Cybernetics
10/2009 - 04/2010	Risø DTU, Denmark Stay abroad to write the diploma thesis "Speed Control of Wind Turbines by Use of Remote Sensing Technologies"
05/2010 - 02/2017	Carl von Ossietzky Universität Oldenburg, Germany PhD research "Lidar-based Reconstruction of Wind Fields and Application for Wind Turbine Control"

Professional Career

05/2010 - 06/2013	Robert Bosch GmbH, Schwieberdingen, Germany PhD in Corporate Research and Advance Engineering, Future Systems Industrial Technology
Since 07/2013	Festo Didactic SE, Denkendorf, Germany Project Engineer Learning Factories Focus on energy efficiency, renewable energies, cloud computing

Eidesstattliche Erklärung

Hiermit erkläre ich an Eides statt, dass ich die vorgelegte Dissertation selbstständig verfasst und alle in Anspruch genommenen Hilfsmittel in der Dissertation angegeben habe.

Die Dissertation hat weder in ihrer Gesamtheit noch in Teilen einer anderen wissenschaftlichen Hochschule zur Begutachtung in einem Promotionsverfahren vorgelegen.

Ludwigsburg, den 20.12.2016